Université d'Ottawa · University of Ottawa

Université d'Ottawa · University of Ottawa

FACULTÉ DES ÉTUDES SUPÉRIEURES ET POSTDOCTORALES

FACULTY OF GRADUATE AND POSTDOCTORAL STUDIES

LEBLANC, Pierre

AUTEUR DE LA THÈSE - AUTHOR OF THESIS

M. Sc. (Physics)

GRADE - DEGREE

Department of Physics

FACULTÉ, ÉCOLE, DÉPARTEMENT - FACULTY, SCHOOL, DEPARTMENT

TITRE DE LA THÈSE - TITLE OF THE THESIS

Optical Probing of a Bose-Einstein Condensate

E. Fortin

DIRECTEUR DE LA THÈSE - THESIS SUPERVISOR

CO-DIRECTEUR DE LA THÈSE - THESIS CO-SUPERVISOR

EXAMINATEURS DE LA THÈSE - THESIS EXAMINERS

J. Armitage

I. L'Heureux

S. Raymond

J.-M. De Koninck, Ph.D.

LE DOYEN DE LA FACULTÉ DES ÉTUDES SUPÉRIEURES ET POSTDOCTORALES

SIGNATURE

DEAN OF THE FACULTY OF GRADUATE AND POSTDOCTORAL STUDIES

Optical Probing of a Bose-Einstein Condensate

Pierre J. Leblanc

Thesis submitted to the
Faculty of Graduate and Postdoctoral Studies
in partial fulfillment of the requirements
for the degree of Master of Science in Physics

Department of Physics
University of Ottawa

Your file Votre référence
ISBN: 0-612-90103-3
Our file Notre référence
ISBN: 0-612-90103-3

Abstract

Experimental results acquired with various methods used to optically probe an excitonic Bose-Einstein condensate are presented. The condensate is initially created by a high-intensity pulsed laser illumination ($\lambda = 532\,nm$) incident on a high-quality natural single crystal of Cu_2O (at $T = 1.8\,K$), having (100) symmetry. The travelling condensate is laterally probed by a laser pulse tuned at the 1S orthoexciton resonance ($\lambda = 609.51\,nm$), where significant condensate amplification is observed. Correspondingly, the resonant probing beam is additionally attenuated upon being transmitted through the excitonic packet. In an attempt to measure the condensate's lateral and longitudinal dimensions, the additional attenuation (NDA) is determined at various probing beam positions relative to the perpendicularly propagating packet. A three-dimensional representation of the exciton packet was constructed with spatially dependent NDA measurements.

Highly detailed continuous spectra of the 1S line were taken with the use of a tunable dye laser, permitting the observation of never before seen features in the 1S line. The wavelength dependance of both the condensate amplification and the lateral pulse's additional attenuation were studied using this technique.

The onset of a secondary exciton packet observed in various excitation geometries, further contributed to the amplification model proposed in previous work. Moreover, a strong correlation between electrical and all-optical measurements was found, providing reassurance on the validity of past interpretations based on electrical measurements.

Sommaire

Plusieurs méthodes d'analyse optique sont utilisées pour examiner le Condensat de Bose-Einstein (CBE) d'excitons dans le Cu_2O. Initialement, le condensat est créé par des impulsions laser ($\lambda = 532\,nm$) de haute intensité, incidentes sur un mono-cristal ($T = 1.8\,K$) naturel de haute qualité ayant une symétrie (100). Le condensat est ensuite stimulé et amplifié par une impulsion latérale accordée au voisinage de l'état 1S de l'orthoexciton ($\lambda = 609.51\,nm$). L'atténuation additionnelle (NDA) de la lumière résonante induite par le passage du paquet excitonique est vérifiée à plusieurs positions latérales et longitudinales du paquet. Une représentation tri-dimensionnelle d'un paquet d'excitons a été construite suite aux mesures spatiales du NDA.

À l'aide d'un laser à colorant accordable, des spectres très détaillés au voisinage de la résonance, ont été captés et ont mis en évidence un dédoublement de la ligne 1S. Avec cette technique expérimentale, le phénomène d'amplification du condensat et de l'atténuation additionnelle de la lumière résonante ont été étudiés à plusieurs longueurs d'onde au voisinage de la ligne 1S.

L'observation, sous diverses conditions expérimentales, d'un paquet excitonique secondaire a contribué à une amélioration du modèle d'amplification proposé dans certains travaux précédents. De plus, l'étude des résultats démontre une bonne corrélation entre les résultats obtenus par les mesures photovoltaïques et les mesures purement optiques. Enfin, les résultats confirment la validité des interprétations considérées auparavant suite aux mesures photovoltaïques.

Acknowledgements

I would like to gratefully acknowledge the enthusiastic supervision of Dr. Emery Fortin during this work. I thank André Merizzi, Luc Charron, and Dr. Yazid Braik for stimulating discussions and assistance during experiments. I would also like to acknowledge François Saumier of the Science machine shop for patiently building a sophisticated sample holder at the precision limit of his instrument. I also thank Dr. André Lalonde for his helpful tips on determining the crystallographic axes of our samples using X-ray diffraction. I thank Sylvain Robineau for taking nice pictures of the sample holders. Spelling corrections brought forth by Jennifer Guibord were very useful and greatly appreciated. Many thanks to Natalie and Pascal for their countless encouragements during my studies. Finally, I am forever indebted to my parents Hélène and Jacques for their help and endless support throughout the years.

Statement of Originality

Unless indicated otherwise, experimental results presented in this thesis were collected by the author during experiments at the University of Ottawa. Some of these results were presented in the following:

- **Conference Proceedings**
  - Optical Probing of an Exciton Condensate, E. Fortin, A. Merizzi, and P.J. Leblanc, 5th International Conference on Excitonic Processes in Condensed Matter (EXCON 2002), Darwin, Australia, July 2002.
  - Optical Probing of Excitonic Bose-Einstein Condensates in Cu_2O, P.J. Leblanc, A. Merizzi, and E. Fortin, Canadian Association of Physicists (CAP) Congress, Quebec City, June 2002.
  - Bose-Einstein Condensation of Excitons in Cu_2O, P.J. Leblanc, Canadian Undergraduate Physics Conference (CUPC 2000), Quebec City, November 2000.
- **Journal Papers**
  - Optical probing of an exciton condensate, E. Fortin, A. Merizzi, and P.J. Leblanc, *Journal of Nonlinear Optics*, **29(4-6)**, 211 (2002).
  - Some considerations concerning the detection of excitons in Cu_2O by the voltaic effect, A. Mysyrowicz, P.J. Leblanc, and E. Fortin, *Phys. Stat. Sol.*, Accepted.
  - Enlightenment on the behavior of Excitonic Bose-Einstein Condensates, P.J. Leblanc, and E. Fortin, Under preparation.

Contents

Abstract i

Sommaire ii

Acknowledgements iii

Statement of Originality iv

Table of contents v

List of figures viii

List of tables xii

Introduction 1

1 Theory 6

1.1 Bose-Einstein Condensation 6

1.1.1 Fermions and Bosons 8

1.1.2 Ideal Bose Gas 8

1.1.3 Condensate Properties 11

1.2 Excitons 12

1.2.1 Band Structure of Semiconductors 12

1.2.2 Types of Excitons in Cu_2O 13

1.3 Excitonic BEC 15

1.4 Condensate Amplification 17

2 Experiment 20

2.1 Lasers 20

2.1.1 Pulsed Lasers 20
2.1.2 Laser Beam Attenuation 21
2.2 Exciton-Mediated Photovoltaic Effect 23
2.3 Sample Preparation 25
2.3.1 Sample Polishing 27
2.3.2 Chemical Etching 28
2.3.3 Electrode Depositions 28
2.3.4 Wire Contacts 30
2.3.5 Sample Holder 30
2.4 Experimental Setup 33
2.4.1 Optical Cryostat 33
2.4.2 Data Acquisition 34
2.4.3 Detectors, Optical Fibres, and Connectors 35
2.4.4 Excitation Geometries 38
2.5 Basic Time-Resolved Signals 40
2.5.1 Transmission Signal (Photodetector) 41
2.5.2 PV Signal (Exciton Detector) 41
2.5.3 Time-Resolved Signals Observed in Actual Experimental Excitation Geometries 50
2.6 Linearity and Efficiency of the Exciton Detector 53

3 Results **57**
3.1 Time-Resolved Signals Related to Bose-Einstein Condensation 58
3.1.1 Condensate Amplification 58
3.1.2 Normalized Differential Attenuation (NDA) 60
3.1.3 Secondary Packet Formation 62
3.2 Continuous Spectra 73
3.2.1 PV Spectrum between 600-610nm 73
3.2.2 Transmission and PV Spectrum in the Vicinity of the 1S Line . . 75
3.2.3 Temperature Evolution of the 1S Line 76
3.2.4 Wavelength Dependence of Condensate Amplification 79
3.2.5 Wavelength Dependence of the Formation of the Secondary Packet 81
3.2.6 Spectral Splitting of the 1S Line 82
3.3 Longitudinal Measurements 88
3.3.1 Longitudinal Condensate Amplification & NDA 88

3.4 Lateral Measurements 90
3.4.1 Lateral NDA 90
3.4.2 The Impact of the Pump Beam's Vertical Position on NDA 96

Conclusion 98

Bibliography 100

List of Figures

1.1 Condition for Bose-Einstein Condensation. Figure taken from [23] 7
1.2 Average occupation of the ground state as a function of temperature. . . 11
1.3 A) direct transition, B) indirect transition. 12
1.4 Exciton energy levels for $\vec{k} = 0$. Excitonic levels were not drawn to scale with respect to the band structure. 14

2.1 Pulsed dye laser average power variation over a range of output wavelengths. 22
2.2 The quadruple-wedge optical attenuator. 23
2.3 Schematic of the exciton-mediated photovoltaic effect. 24
2.4 Electrode configuration for high intensity time-resolved photovoltaic detection. 25
2.5 Dimensions of the two Cu_2O samples used during experiments. (Not drawn to scale) 26
2.6 Cu_2O crystal mounted on a sample holder, depicting the Au (ring) and Cu (disk) electrodes. Gold wires are firmly fixed to the electrodes by a special conductive epoxy compound. 29
2.7 Sample holder schematic, as developed in [16]. 31
2.8 Copper sample holder with three illumination conduits. Sample#2 was placed in this holder for most of the experiments 32
2.9 Brass sample holder with five illumination conduits; this holder was used to support Sample#2 for several experiments. 33
2.10 Positions of the optical fibers used for two purposes: 1)Light-collecting; 2) Time-delaying. 35
2.11 Beam displacement with glass plate 37
2.12 Various excitation geometries 38
2.13 General experimental setup 39

2.14 Time-resolved transmission signal resulting from a resonant pulsed illumination ($\lambda = 609.51\,nm$), incident along the sample's secondary axis. Light transmitted through the sample was collected and transmitted towards an external photodetector via an optical fiber where light was detected. The signal's FWHM corresponds to the laser pulse duration of 10ns. 42
2.15 Time-resolved "front" signal corresponding to a slightly off-resonant ($\lambda = 609.56\,nm$) pulsed laser illumination, incident on the exposed face of the exciton detector (deposited electrodes). Two signal components (metallic and exciton) are clearly depicted. The "metallic" signal has a FWHM of ~10ns corresponding to the laser pulse duration of 10ns. The broad signal is the result of migrating excitons. 43
2.16 Time-resolved signals resulting from a Nd:YAG laser pulse incident on the back face of the electrodes. Signals (A and B) are shown for two laser intensities, while the third signal (C) is normalized to match signal B's amplitude. 45
2.17 Time-resolved dye laser "front" signal in the vicinity of the 1S line, compared to the Nd:YAG laser "front" signal. Both laser excitation were performed on the back side of the exciton detector. 46
2.18 Time-resolved "front" signal resulting from a dye laser pulsed illumination tuned at the 1S orthoexciton resonance ($\lambda = 609.51$nm). Excitation is on the back face of the electrodes. 47
2.19 Time-resolved front signals resulting from pulsed dye laser illumination at various wavelengths in the vicinity of the 1S line. The laser pulse is incident to the back side of the electrodes. 49
2.20 Dye laser front signal resulting from a resonant pulsed excitation ($\lambda = 609.51$nm). The signals result from three different laser excitation geometries, and are normalized to show the same amplitude. 51
2.21 Time-resolved signals generated by a pulsed Nd:YAG laser illumination ($\lambda = 532$nm) along the sample's main axis. An excitonic packet is detected at the opposing crystal face, where the exciton detector lies. 52
2.22 Time-resolved dye laser front signals for various intensities. The resonant ($\lambda = 609.51$nm) laser pulse is incident along the sample's main axis. . . . 54
2.23 Peak and integrated signals of traces shown in Figure 2.22, versus intensity. 55

3.1 Time-resolved signals resulting from excitation in the orthogonal geometry. a. A Nd:YAG laser pulse is incident on the sample's main axis. In a separate measurement, a time-delayed ($\delta t = 170ns$) dye laser pulse tuned at $\lambda = 609.51$nm is incident on the sample's secondary axis. b. The signal resulting from the orthogonal excitation of both laser pulses described above. 59

3.2 The time-resolved transmission signal resulting from a resonant ($\lambda =$ 609.51nm) dye laser pulse excitation along the sample's secondary axis. Light transmitted through sample was collected with an optical fiber and thereafter detected by an external photodetector. The transmission signals were measured in the presence and absence of the exciton condensate, where an NDA of ~45% was observed. The dye laser time-delay of $\delta t = 770ns$, corresponds to the resonant pulse intercepting the tail end of the exciton packet. 61

3.3 Onset of a secondary packet at time-delays "δt" larger than the condensate's half-transit time ($\delta t = 300ns$). Excitations were performed in the orthogonal geometry, with a dye laser tuned at resonance ($\lambda = 609.51$nm). The secondary packets are pointed out by arrows. The top-left figure is presented on a different scale to better show the condensate amplification. 63

3.4 Secondary packet created in the collinear excitation geometry with various dye laser wavelengths. The dye laser pulse is delayed by 770ns with respect to the Nd:YAG laser pulse. 65

3.5 Zoom-in view of the secondary packet signals presented in Figure 3.4. . . 66

3.6 Secondary packet created in the collinear excitation geometry with various dye laser wavelengths. The dye laser pulse is delayed by 1200ns with respect to the Nd:YAG laser pulse. 67

3.7 Zoom-in view of the secondary packet signals presented in Figure 3.6. . . 68

3.8 Secondary packet created in the collinear excitation geometry with various dye laser wavelengths. The dye laser pulse is delayed by 300ns with respect to the Nd:YAG laser pulse. 69

3.9 Secondary packet created in the collinear excitation geometry with various Nd:YAG laser intensities. The dye laser pulse is delayed by 1200ns with respect to the Nd:YAG laser pulse. 71

3.10 Time-resolved signals demonstrating the presence of a secondary packet with various pump-probe beam time-delays. 72

3.11 Absorption spectrum of Cu_2O depicting three regions of interest: absorption at the band edge, phonon-assisted absorption, and n=1 resonant absorption line. 74
3.12 Transmission and PV spectra in the vicinity of the n=1 orthoexciton line. 76
3.13 Temperature evolution of the 1S line. 77
3.14 Change in position and linewidth of the 1S orthoexciton absorption line for various temperatures. This figure was constructed with the use of Figure 3.13 78
3.15 Wavelength dependence of the condensate amplification. 80
3.16 Wavelength dependence of the secondary packet formation, for a probe beam time delay of $\delta t = 770ns$ with respect to the Nd:YAG laser pulse. . 81
3.17 PV and Transmission spectra demonstrating a prominent splitting. . . . 83
3.18 Transmission spectra taken in the absence and presence of the exciton condensate, where a prominent splitting is shown. 85
3.19 Wavelength dependance of both the condensate amplification and the NDA, where a prominent splitting is displayed. 86
3.20 The wavelength dependence of both the condensate amplification and the secondary packet formation. 87
3.21 Probe beam time-delay (longitudinal) dependance of condensate amplification and NDA, in the orthogonal excitation geometry. The dye laser was tuned at the 1S orthoexciton resonance. 89
3.22 NDA measured at three different fiber positions, for various probe beam time delays. 91
3.23 Side view: 3D representation of the travelling exciton packet with NDA. . 92
3.24 Rear view: 3D representation of the travelling exciton packet with NDA. 93
3.25 Top view (contrast) of the 3D representation of the travelling exciton packet constructed with spatial NDA measurements. 94
3.26 NDA measured at five different fiber positions, for various probe beam time delays. 95
3.27 NDA measured by different vertical positions of the Nd:YAG laser. . . . 96

List of Tables

2.1 Guidelines for sample polishing. 27
2.2 Guidelines for chemical etching. 28
2.3 Guidelines for wire contacts. 30

Introduction

One of nature's most fascinating properties is the fact that particles can behave like waves. According to the wave theory of matter, it is said that a state of a particle can be fully described by a wavefunction. Under certain conditions, the wavefunctions of neighboring particles can become overlapped, making it increasingly difficult to distinguish them apart. When the particles' wavefunctions completely overlap each other, the distinguishing process becomes impossible. This seemingly indistinguishable state of particles (multiple occupancy of a quantum state) is what is known as Bose-Einstein Condensation (BEC). The possible existence of such physical state was predicted in 1925 by A. Einstein [1] while collaborating with mathematician S. Bose [2], hence the name Bose-Einstein Condensation. The confirmation of its physical existence for atoms came in 1995, when BEC of Rubidium [3] and Sodium [4] atoms was observed. The BEC phenomenon has managed to spark interest in both the research community (Nobel Prize for physics (2001) was awarded to E. Cornell, C. Wieman, and W. Ketterle for their pioneering work in the field) and the general public [5].

Observing Bose-Einstein Condensation of atomic systems is an outstanding achievement, considering that it occurs at temperatures on the order of a millionth of a degree from absolute zero. Achieving such low temperatures involves many complex steps using sophisticated equipment. These laboratory instruments are expensive and limited to a few researchers worldwide. Meanwhile in order to pursue research in the field of BEC before the advent of such sophisticated equipment to reach temperatures on the order of nanokelvin, scientists were on the lookout for more accessible particle systems suitable for BEC study. In semiconductors, bound electron-hole pairs known as excitons, became attractive candidates [6, 7, 8, 9] for such research. Their integer spins classifies them in the boson-type category of particles, which can have the property of condensing into a coherent state. However, the relatively low effective mass of excitons remains a key point of interest, as it enables BEC to occur at reasonably high temperatures compared to the case of atomic systems. The critical temperature for the onset of excitonic BEC is

typically on the order of a few Kelvins (at a density of $10^{17}\,cm^{-3}$), and can be achieved with liquid ^{4}He, which is readily accessible.

Excitons in cuprous oxide (Cu_2O) are particularly suitable candidates for BEC, since the radiative decay of the 1S paraexciton (spin zero singlet state) is forbidden (optically inactive), resulting in a long exciton lifetime. This long lifetime enables the observation of anomalous ballistic transport of paraexcitons over large distances following an intense laser pulse excitation at the surface of a Cu_2O crystal. The ballistic transport was observed at low crystal temperatures, at high particle densities [10, 11, 12, 13, 14], and was attributed to the onset of excitonic superfluidity in [12]. Optical imaging was originally used to monitor the dense population of migrating excitons from the excitation surface [10, 11]. Although paraexciton detection by means of photoluminescence is deemed unsuitable for transport study because of the optically inactive nature of the n=1 paraexcitons, migrating excitons were successfully investigated with the use of a photovoltaic detector [12, 13, 14].

Our research group's pioneering work on BEC was carried out by E. Benson [15]. In his work fundamental properties of excitonic Bose-Einstein condensates were studied. Exciton transport was thoroughly investigated, particularly the transition from the diffusive to ballistic transport regimes. This regime transition of exciton transport was later attributed to the onset of excitonic BEC, in which the ballistic condensate was shown to travel through the crystal at near sonic velocities. The temperature dependance of ballistic transport was found to be equivalent to varying the excitation intensities, in agreement with BEC theory. The interference of two coherent condensates was also investigated during his work. A somewhat surprising result was found when considerable amplification of the condensate was observed when exposed to a secondary excitation having relatively low intensity. The source of secondary excitation used in this work was a continuous wave (CW) laser tuned at the 1S orthoexciton energy. In conclusion to his work, E. Benson proposed a model to help better visualize and explain particular properties of the condensate. The model was analogous to the structure of a comet composed of three main components: 1) The Core: Excitonic Condensate, 2) The Coma: Nearly condensed excitons closely surrounding the condensate, and 3) The Tail: Uncondensed excitons left behind by the ballistically travelling condensate.

Research work on excitonic BEC continued with M. Massé [16], who investigated the effects of various packet-forming initial conditions. For the most part of his work the exciton packet was formed using two different illumination wavelengths, individually creating them at two different penetration depths, due to the wavelength dependant

absorption coefficient. Although one of the illumination wavelengths corresponded to having three times as much excess energy available for phonon creation compared to the other illumination wavelength, both packets (formed with different wavelengths) were found to yield similar dependance on the initial exciton density, consequently casting doubt upon the "phonon wind" interpretation brought forth by S. Tikhodeev [18] as an alternate explanation of our results. Expanding on the previous work of E. Benson, M. Massé further studied the packet amplification resulting from a secondary excitation. Unlike in [15], where a CW illumination was used, a pulsed excitation was applied to probe the exciton packet during the course of his work. With a pulsed excitation, the additional absorption observed in the presence of the travelling exciton condensate can be quantified. This quantification was termed the Normalized Differential Attenuation (NDA). Pulsed excitations allowed many other measurements to take place, such as the longitudinal dependence of the amplification and the NDA. By deliberately time delaying the secondary excitation with respect to the packet creating (primary) excitation, the longitudinal probing of any chosen part of the packet (core, coma, or tail) was achieved. Amplification and NDA measurements were also performed at various intensities for both the primary and the secondary excitation. The interference properties of two coherent condensates were redone using different initial dynamics than the ones used in [15], which confirmed the presence of a quantum coherent state. And for the first time, the onset of a secondary exciton packet was observed. The formation of an additional exciton packet occurred at large time delays (high transit times of the packet).

Subsequent to the work of M. Massé, A. Merizzi's work [19], focused on studying the interactions between the resonant secondary excitation and the exciton packet. To do so, he carried out some of his research on a sample having a crystal orientation ($[111] \times [1\bar{1}0] \times [11\bar{2}]$) permitting polarization-dependent measurements. In his work, emphasis was shifted towards the time-resolved signals resulting from a secondary excitation that seemed to have been overlooked in previous work. The philosophy behind this approach was to directly observe the effects of the secondary excitation, and thereafter correlate the results with the effects seen in the presence of the packet. In doing so, various components of the time-resolved front signal were identified by investigating the signal's temporal shape at various wavelengths. Moreover, condensate amplification and the NDA were characterized at various secondary excitation wavelengths. The scattered portion of the secondary excitation incident on the electrodes was also found to be unusually attenuated (F-NDA) in the presence of the excitonic packet. With the use of his results, A. Merizzi further elaborated on the model originally proposed by E. Benson to include

a possible explanation for the amplification of the condensate.

However, despite years of research on BEC of excitons in Cu_2O, many of the condensate's properties still remain unknown. For instance, the lateral spatial distribution of exciton inside the propagating packet has never been measured. The exact mechanism leading to the condensate amplification from a relatively low illumination intensity tuned at the 1S resonance remains largely unexplained. In an attempt to answer some of these questions, additional research work was recently done. Such work is presented in this thesis.

To reduce any confusion raised in the past, a special effort was made in this thesis to clearly explain all of the time-resolved signals encountered during BEC experiments. In order to convincingly verify that the properties of the phenomena are due to BEC, this work emphasized on relating both the optical measurements of the condensate properties with similar measurements taken by non-optical means (exciton detector). In fact, highly detailed spectra taken with the use of the tunable dye laser, convincingly demonstrated that spectra of the 1S line observed by the exciton detector is complementary to the all-optically measured spectrum (see section 3.2.2). This spectra-acquiring technique which has a much better resolution than the spectrometer in the laboratory, resulted in the observation of never before seen features of the 1S line (section 3.2.6). Such features were helpful in linking the mechanisms responsible for the condensate amplification and the observation of additional beam attenuation (NDA). Temperature dependent spectra of the 1S were also measured using this technique (section 3.2.3). The 1S line's temperature evolution behaved according to theoretical predictions of excitonic lines; however a noticeable increase in the linewidth for modest rises in temperature led us to believe that the actual 1S linewidth should be much larger than the reported value determined through indirect observations by D. Fröhlich [20].

Along our quest for a plausible condensate amplification explanation, the onset of the secondary packet was further studied. Secondary packet formation under various experimental conditions helped to determine the mechanisms at work when probing the condensate's incoherent tail. The formation of the secondary packet was found to be extremely sensitive to the pump beam intensity, suggesting the exciton density in the tail of the condensate to be near the critical density.

But most importantly, by applying the "pump and probe" technique to longitudinally and laterally probe the travelling condensate, a three-dimensional mapping of the condensate was produced for the first time. This 3D representation confirmed the exciton packet's component, as first pointed out by E. Benson.

This document is partitioned in three major sections. The first part provides the theory related to excitonic BEC in Cu_2O. The following section deals with the experimental techniques as well as a description of the instruments used during this research project. Experimental results are presented in the third part, in which they are also discussed.

Chapter 1

Theory

This chapter serves as a theoretical reminder concerning the Bose-Einstein Condensation (BEC) phenomenon. Because of the weakly interacting particle system used during experiments, the ideal Bose gas treatment of BEC is presented in this chapter. Excitons and excitonic BEC will be described afterwards followed by the amplification process of the condensate.

1.1 Bose-Einstein Condensation

Bose-Einstein Condensation is a manifestation of the wave-like nature of particles. According to quantum mechanics, the quantum state of a particle is described by a wavefunction.

Beginning with the example shown at the top of Figure 1.1, particles in a box are described as having a velocity "v" with a separation distance of "d". However, from the wave theory's point of view, each particle can also be described as a wavefunction having a wavelength expressed by the deBroglie wavelength "λ_{dB}":

$$\lambda_{dB} = \frac{h}{mv} \tag{1.1}$$

where h is Planck's constant, m is the mass of the particle and v is the particle velocity. According to the kinetic theory of gases, the average translational kinetic energy of a particle is given by:

$$\frac{1}{2}m\overline{v^2} = \frac{3}{2}k_BT \tag{1.2}$$

where m is the mass of the particle, $\overline{v}$ is the average particle velocity, k_B is Boltzmann's

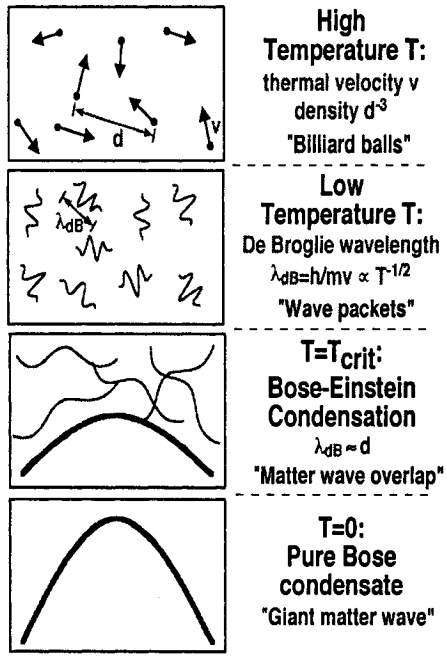

Figure 1.1: Condition for Bose-Einstein Condensation. Figure taken from [23]

constant, and T is the gas temperature. By combining eq.1.1 and eq.1.2 one can obtain an expression for the average thermal deBroglie wavelength.

$$\overline{\lambda_{dB}} = \frac{h}{\sqrt{3mk_BT}} \tag{1.3}$$

The average thermal deBroglie wavelength is shown in eq.1.3 to be temperature dependent ($\overline{\lambda_{dB}} \propto T^{-\frac{1}{2}}$). An increase in the deBroglie wavelength results from a drop in temperature. When the thermal deBroglie wavelength becomes comparable with the inter-particle separation, the wavefunctions of individual particles overlap making it increasingly difficult to distinguish particles from each other as shown in Figure 1.1. When the deBroglie wavelength is larger than the inter-particle separation ($T \leq T_{critical}$), the particle distinguishing process becomes impossible since particles appear to be all in the same state. If the particles have the ability to condense (see section 1.1.1), the wavefunction of all the particles in the condensate would collapse into a macroscopic quantum state consisting of a superposition of identical wavefunctions triggering the onset of a Bose-Einstein Condensate. For a weakly interacting particle system such as paraexcitons in Cu_2O, the ideal Bose gas treatment is a good approximation.

1.1.1 Fermions and Bosons

Quantum effects are an important factor in the interactions between particles, in a system having a high density at low temperature. The particles' wavefunctions determine the types of interactions in such a regime. There exists only two types of quantum particles: fermions (having a half-integer spin) and bosons (having an integer spin). The boson wavefunction is even under particle exchange,

$$\Psi(\vec{r_1}, \vec{r_2}) = \Psi(\vec{r_2}, \vec{r_1}). \tag{1.4}$$

whereas that for the fermion is odd.

$$\Psi(\vec{r_1}, \vec{r_2}) = -\Psi(\vec{r_2}, \vec{r_1}), \tag{1.5}$$

Fermions behave according to the Fermi-Dirac distribution, where only a single particle can occupy a particular quantum state (Pauli's exclusion principle). Bosons however, obey the Bose-Einstein distribution where an unlimited number of these type of particles can occupy a single quantum state. The latter property of boson-type particles is what enables these particles to condense into a state called Bose-Einstein Condensation. Such a state have different properties compared to solids, liquids, or gases due to the symmetry of the particle's wavefuntion. Some unique properties of this BEC state, includes superfluidity (drag-free motion) similarly to the case of Cooper pairs, the proposed mechanism for superconductivity according to the BCS (Bardeen Cooper Schrieffer) theory.

1.1.2 Ideal Bose Gas

An ideal Bose gas is a system of non-interacting bosons where quantum statistics is a dominant factor in the behavior of the particles. Paraexcitons in Cu_2O can be well approximated by this model, since interactions between these particles are negligible. Beginning with the boson partition function, predictions of the basic properties of an ideal quantum gas can be determined with the derivation of the ideal Bose gas equation of state. In the Grand Canonical Ensemble the boson partition function "L" is given by

$$L(z, V, T) = \sum_{N=0}^{\infty} z^N e^{-\beta \sum \varepsilon_{\vec{p}} f_{\vec{p}}} = \prod_{\vec{p}} \left[\sum_{f_{\vec{p}}} \left(z e^{-\beta \varepsilon_{\vec{p}}} \right)^{f_{\vec{p}}} \right], \tag{1.6}$$

where N is the number of particles, V the volume, T the temperature, $f_{\vec{p}}$ is the occupation number of a state with energy $\varepsilon_{\vec{p}}$, $\vec{p}$ is the momentum, β is equal to $\frac{1}{k_B T}$ and z is the

fugacity (the fugacity is related to the chemical potential μ by $z = e^{\beta\mu}$). The total number of particles is limited by the condition $\sum f_{\vec{p}} = N$, as the sum of occupation numbers must return the total number of particles. For bosons, $f_{\vec{p}}$ is any positive integer, because state degeneracies are unlimited. The sum over $f_{\vec{p}}$ is a geometric series $\left(\sum_{s=0}^{\infty} r^s = \frac{1}{1-r}\right)$ reducing the partition function for bosons to:

$$L(z,V,T) = \prod_{\vec{p}} \frac{1}{1 - ze^{-\beta\varepsilon_{\vec{p}}}}. \tag{1.7}$$

With the use of eq.1.7, the equations of state can be obtained.

$$\frac{PV}{k_B T} = \log L(z,V,T) = -\sum_{\vec{p}} \log(1 - ze^{-\beta\varepsilon_{\vec{p}}}), \tag{1.8}$$

$$N = z\frac{\partial}{\partial z} \log L(z,V,T) = \sum_{\vec{p}} \frac{ze^{-\beta\varepsilon_{\vec{p}}}}{1 - ze^{-\beta\varepsilon_{\vec{p}}}}. \tag{1.9}$$

In the limit as $V \to \infty$ the possible values of $\vec{p}$ form a continuum and the sum over $\vec{p}$ in eq.1.8 and eq.1.9 is replaced by an integration such that $\sum_{\vec{p}} \to V \cdot \frac{2s+1}{h^3} \int d^3\vec{p}$ where s is the particle spin and h is Planck's constant. Eq.1.8 and eq.1.9 can be rewritten as:

$$\frac{P}{k_B T} = -\frac{4\pi \cdot (2s+1)}{h^3} \int_0^{\infty} dp\, p^2 \log(1 - ze^{-\beta p^2/2m}) - \frac{1}{V}\log(1-z), \tag{1.10}$$

$$n = \frac{4\pi \cdot (2s+1)}{h^3} \int_0^{\infty} dp\, p^2 \frac{1}{z^{-1}e^{\beta p^2/2m} - 1} + \frac{1}{V}\frac{z}{1-z}. \tag{1.11}$$

where $n = N/V$ is the density.

Since the boson ground state term can be as important as the rest of the states, it has been taken out of the sum before being converted to an integral. The integration of eq.1.10 and eq.1.11 can now be performed, providing the relations between pressure(P), density(n), temperature(T) and fugacity(z) for an ideal Bose gas.

$$\frac{P}{k_B T} = \frac{(2s+1)}{\lambda^3} g_{5/2}(z) - \frac{1}{V}\log(1-z), \tag{1.12}$$

$$n = \frac{(2s+1)}{\lambda^3} g_{3/2}(z) + \frac{1}{V}\frac{z}{1-z}, \tag{1.13}$$

$\lambda = \sqrt{\frac{2\pi\hbar^2}{mk_B T}}$ is the thermal wavelength and $g_n(z) \equiv \sum_{l=1}^{\infty} \frac{z^l}{l^n}$. From the partition function (eq.1.6), the average occupation number $< f_{\vec{p}} >$ can be derived as:

$$< f_{\vec{p}} >= -\frac{1}{\beta}\frac{\partial}{\partial \varepsilon_{\vec{p}}} \log L = \frac{z e^{-\beta \varepsilon_{\vec{p}}}}{1 - z e^{-\beta \varepsilon_{\vec{p}}}}. \tag{1.14}$$

Since $< f_{\vec{0}} >$ is equal to $z/(1-z)$ for the ground state, ($\varepsilon_{\vec{p}} = 0$). Eq.1.14 becomes:

$$\frac{< f_0 >}{V} = n - \frac{2s+1}{\lambda^3} g_{3/2}(z). \tag{1.15}$$

where $g_{3/2}(z)$ increases monotonically over the range $z = 0 \ldots 1$ with $g_{3/2}(1) = 2.612$. Eq.1.15 implies that there is a finite number of particles in the ground state if:

$$n > \frac{2s+1}{\lambda^3} g_{3/2}(z). \tag{1.16}$$

The macroscopic occupation of the ground state is called Bose-Einstein condensation

By substituting the values of λ and $g_{3/2}(1)$ in eq.1.16, one obtains a temperature-dependent expression for the critical density above which particles in the ground state of an ideal Bose gas will condense.

$$n_c = 2.612 \cdot (2s+1) \cdot \left(\frac{m k_B}{2\pi\hbar^2}\right)^{3/2} T^{3/2}. \tag{1.17}$$

One can also determine the fraction of total particles within the condensate by dividing both sides of eq.1.15 by the density n:

$$\frac{< f_0 >}{N} = 1 - \frac{2s+1}{n\lambda^3} g_{3/2}(z). \tag{1.18}$$

We then substitute $g_{3/2}(z)$ by $g_{3/2}(1)$ ($z \to 1$ for a non-zero condensed fraction), and use $g_{3/2}(1) = \frac{n\lambda_c^3}{2s+1}$, where λ_c is calculated at the critical temperature T_c, in eq.1.18 to obtain:

$$\frac{< f_0 >}{N} = \begin{cases} 1 - \left(\frac{T}{T_c}\right)^{3/2} & T \leq T_c \\ 0 & T \geq T_c \end{cases}. \tag{1.19}$$

Eq.1.19 is graphically shown in Figure 1.2 where a fraction of the total particles is seen to occupy the ground state for $T < T_c$. None of the energy states are occupied by a finite fraction of all particles for the case when $T > T_c$. In the latter case, particles are spread over all available energies, and there is no condensation. However in the case when $T < T_c$, a condensate will form and all remaining particles will spread thinly over the excited states. Studied in this thesis is the condensation of $s = 0$ excitons (paraexcitons) in Cu_2O crystals (discussed in section 1.2.2). Initial exciton densities are estimated at approximately $10^{17} - 10^{18}\, cm^{-3}$ in our experimental conditions. Using this value for

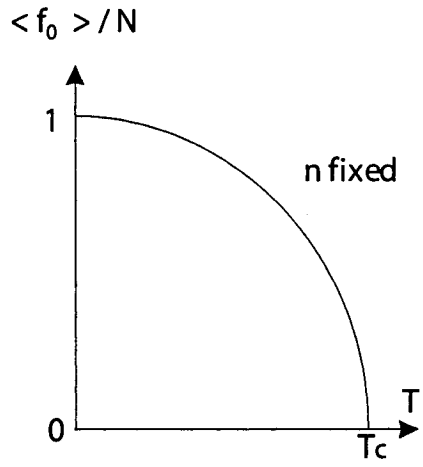

Figure 1.2: Average occupation of the ground state as a function of temperature.

n_c in eq.1.17, and substituting m by the paraexciton mass of $2.7m_0$ [24], where m_0 is the free electron mass, a critical temperature range of approximately $T_c = 4 - 16\,K$ is obtained. A corresponding condensed fraction range of $\sim 65 - 95\,\%$ is calculated with eq.1.19, for a sample temperature of $T = 2\,K$.

1.1.3 Condensate Properties

An important condensate property related to the BEC phenomenon is superfluidity, similarly observed in ^{4}He below the λ-point of T=2.17K. The condensate contains two components: a superfluid component composed of the particles in the ground state ($\varepsilon_{\vec{p}} = 0$), and a normal component formed of all the particles in the excited states ($\varepsilon_{\vec{p}} \neq 0$). The normal component behaves as a liquid at high density and a classical gas at low particle density. The superfluid component however behaves differently; it has irrotational flow which enables the condensate to move as a whole. The latter is a manifestation of the general principles of quantum mechanics where many particles occupying a single state are invariant under translation. As a result the condensate can be described by a single wavefunction (product of all of the wavefunctions of the condensed particles). The condensate can therefore be viewed as a "giant matter wave" having a definite phase, enabling it to interfere with similar condensates. The interference of two condensates was demonstrated in [15, 16, 17].

During BEC experiments, paraexcitons formed in a semiconducting (Cu_2O) crystal are the system of bosons used. This particle system is described in section 1.2.2.

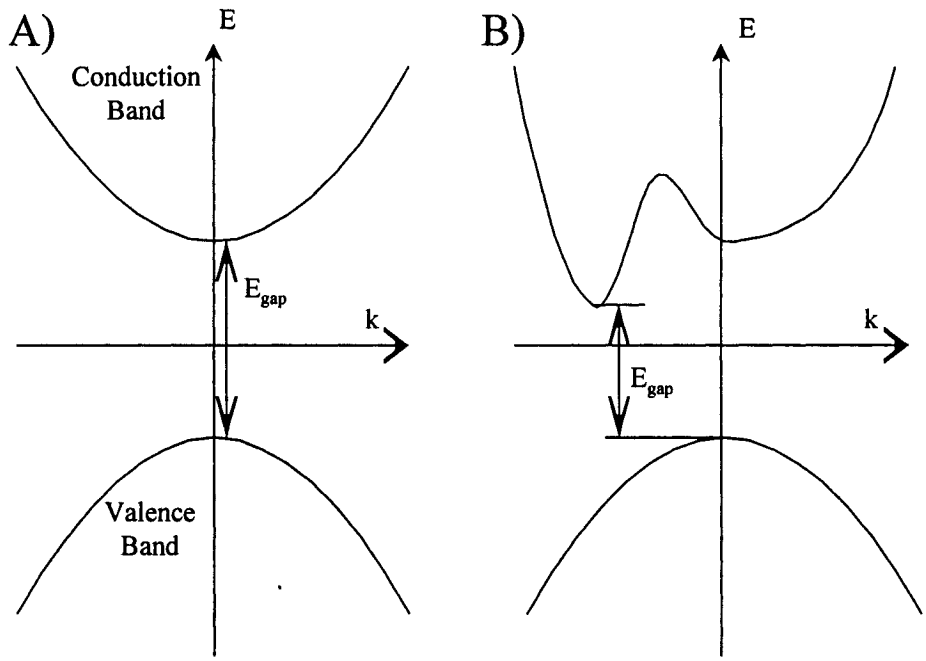

Figure 1.3: A) direct transition, B) indirect transition.

1.2 Excitons

1.2.1 Band Structure of Semiconductors

From the periodicity of the lattice, electrons in a crystal are confined to energy bands, separated by a forbidden gap (band gap) where no energy levels are permitted. The second last highest filled band is called the valence band, while the next band (above the band gap) is called the conduction band. If the conduction band is partially filled as it is in the case of most metals, the material is characterized as a conductor. If however the conduction band is empty, the electrons cannot travel and the material is said to be an insulator. A semiconducting material is characterized as having a conductivity in between the two latter cases (insulator and conductor). An intrinsic semiconductor is essentially an insulator for which the thermal energy ($E_{gap} \approx k_B T$) may be sufficient to promote electrons from the valence band to the conduction band.

The energy bands of a semiconductor can result in either a direct gap or indirect gap. Figure 1.3 illustrates the two common band structures as a function of the electron wavevector "$\vec{k}$". In Figure 1.3A), a direct transition is represented by a vertical line

linking the minimum of the conduction band to the maximum of the valence band. This transition does not require a change in $\vec{k}$; A transition may occur by the simple absorption of a photon of energy $E_{gap} = \hbar\omega$, where ω is the absorbed photon's frequency, and E_{gap} corresponds to the band gap energy. An indirect transition is depicted in Figure 1.3B), where the valence band maximum and the conduction band minimum are not directly aligned with each other. In this case, absorption can only occur with the help of the emission or absorption of phonons which induces the required change in electron momentum $\hbar\vec{k}$. In a phonon assisted transition the absorbed photons will have energies of $\hbar\omega = E_g \pm E_{phonon}$, a substraction of "$E_{phonon}$" for phonon absorption, and an addition of "E_{phonon}" for phonon emission.

The transition probability of the absorption process is proportional to the density of states of the initial and final energy levels. The experimental representation of the transition probability is usually referred to as the absorption coefficient "$\alpha(\lambda)$", which is a function of the incident photon wavelength "λ".

The intensity of light "I" transmitted through a medium of distance z is given by the Beer-Lambert law:

$$I = I_0 e^{-\alpha(\lambda)z}, \tag{1.20}$$

where I_0 is the intensity of light incident on the sample surface. The absorption coefficient's units of inverse length, represents a loss factor due to absorption for a given trajectory per unit length within the absorptive medium.

1.2.2 Types of Excitons in Cu_2O

After an electron has been excited out of the valence band, it leaves behind a hole which has a positive charge. Due to the electron and the hole's close proximity, they interact with each other via the Coulomb potential. Analogous to the interaction between the electron and the proton in an hydrogen atom, an exciton consists of an bound electron-hole pair. However, in the case excitons the Coulomb interaction is screened by the periodic lattice field, resulting in the effective Rydberg much smaller when compared to the hydrogen atom. The combination of the two component of the exciton results in a neutral particle with spin magnitude of zero or one, since an electron and a hole both have spins of $\pm\frac{1}{2}$. Excitons having a spin of zero are called paraexcitons, while excitons with a spin magnitude of one are labelled orthoexcitons.

The exciton's binding energy follows the same type of series as the hydrogen atom,

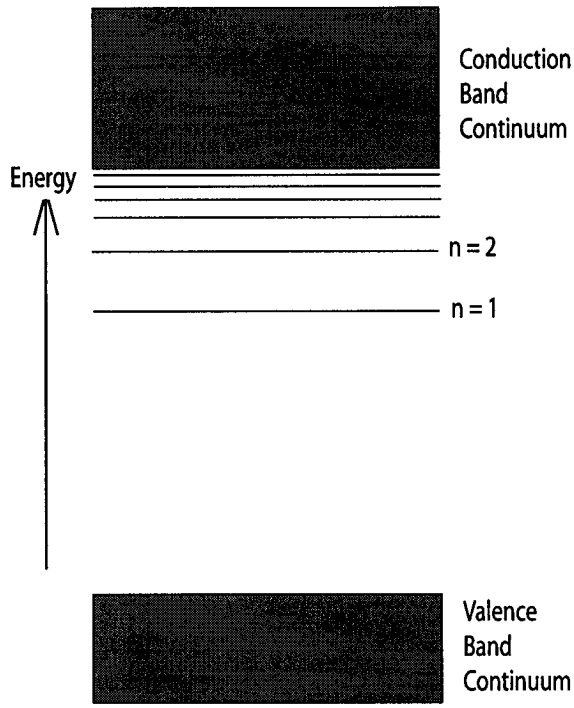

Figure 1.4: Exciton energy levels for $\vec{k} = 0$. Excitonic levels were not drawn to scale with respect to the band structure.

with the exception of additional parameters (ϵ and μ), to account for the screening effect of the ions in the lattice:

$$E_{binding} = \frac{e^4 \mu_{ex}}{2\hbar^2 \epsilon^2 n^2} \qquad n = 1, 2, 3, \ldots , \tag{1.21}$$

where e is the electronic charge, ϵ is the static dielectric constant of the medium ($\simeq 7$ in Cu_2O [25]) and $\mu_{ex} = m_e m_h/(m_e + m_h)$ is the exciton reduced mass where m_e and m_h are the electron and hole effective masses, respectively. From eq.1.21 (schematically represented in figure 1.4), the exciton energy levels are located within the band gap just below the conduction band, meaning that absorption of photons less energetic than the band gap energy will take place; such photons would otherwise be completely transmitted through the material in the absence of excitonic levels. The binding energy of the 1S paraexciton is $\sim 150meV$.

There are two types of excitons (Frenkel and Wannier-Mott) categorized according to their average radii (the distance between the electron and the hole). The Frenkel type of excitons have a radius on the order of the lattice constant and are bound to their parent atoms; Wannier-Mott excitons have a radius larger than the lattice constant and are free to move throughout the crystal. The latter type of excitons are the one studied in Cu_2O. The exciton radius is given by:

$$r_{ex} = a_0 \frac{m_0}{\mu_{ex}} \epsilon n^2, \tag{1.22}$$

where a_0 is the Bohr radius and m_0 is the free electron mass.

1.3 Excitonic BEC

Excitons created in Cu_2O crystals are excellent candidates for BEC, since their mass is relatively small ($2.7\, m_0$ [24]) and the average excitonic radius is $\approx 0.7\, nm$ [26]. According to the ideal Bose gas approximation of $n r_{ex}^3 << 1$ where n is the exciton density, excitons in Cu_2O satisfy the ideal gas criterion for densities up to $10^{20}\, cm^{-3}$. Such a density is well above the maximum densities reached in our experimental conditions. Furthermore, the exciton's small radius prevents Mott dissociation (breakdown of the excitons into an electron-hole plasma at $n r_{ex}^3 \approx 0.3$) which would take place at $n > 10^{21}\, cm^{-3}$, a condition definitely not reached in our laboratory. The repulsive exciton-exciton potential reported in [27] promotes the creation of excitonic condensates, and discourages the formation of

biexcitons and all other excitonic compounds. This provides an added stability to the exciton system. Unlike atomic BEC, which requires temperatures in the nanoKelvin range, BEC of paraexcitons can be achieved at superfluid helium temperatures $\approx 2K$. At this temperature, the critical density for condensation (eq.1.17) is on the order of $10^{17}\,cm^{-3}$, easily attainable with a Nd:YAG laser pulse (see section 2.6) permitting adequate study of the condensation process.

The density of excitons created by a Nd:YAG laser pulse absorbed in the crystal, will vary with depth according to the following: the density of excitons in a layer dz parallel to the illuminated surface is equal to the loss of photons by optical absorption in this region divided by dz; we assume that every absorbed photon generates one exciton. With eq.1.20, and the fact that $I(z) \propto \frac{N(z)}{A}$ where $N(z)$ is the number of photons in the crystal at a distance z from the illuminated surface A, the density is given by the following expression:

$$n(z) = -\frac{1}{A}\frac{d}{dz}N(z) = -\frac{1}{A}\frac{d}{dz}N_0 e^{-\alpha z} = \frac{\alpha N_0}{A}e^{-\alpha z} \tag{1.23}$$

where α is the absorption coefficient and N_0 is the number of incident photons. The absorption time of the photons in the crystal must be smaller than the exciton lifetime (as in our crystal), in order for eq.1.23 to be valid. The relatively large absorption coefficient ($\alpha(\lambda)$) at $\lambda = 532\,nm$, enables the excitons to propagate away from the illumination surface by means of a large density gradient:

$$\Delta n(z) = \frac{d}{dz}n(z) = \frac{-\alpha^2 N_0}{A}e^{-\alpha z}, \tag{1.24}$$

If the density is above the critical density needed for BEC, the exciton packet will condense and travel through the crystal displaying properties of superfluidity [14]. The propagation velocity of the excitonic packet will approach the sonic velocity of $v_s = 4.5 \times 10^5\,cm/s$ [28] in Cu_2O. If however the density is insufficient, the packet will not condense but will still diffuse through the crystal at a reduced velocity due to drag from interactions with the crystal lattice; broadening of the packet will also be observed.

Theoretical work by Loutsenko and Roubtsov [29] has suggested a solution to superfluid travel of exciton condensates. The authors of [29] propose that interactions between excitons and phonons play a key role when the propagation velocity of the condensate is near the velocity of sound. Resulting from their calculations, they predicted the existence of a critical velocity v_c, above which superfluidity is achieved. In Cu_2O, the critical velocity is predicted at $0.5 - 0.7v_s$. No solutions apply for velocities above the speed of sound.

Stationary solutions were found for condensates propagation "v" when $v_c < v < v_s$. The resulting particles distribution has the shape of a soliton.

$$n(z) = n_0 sech^2\left(\frac{z - z_0}{\Delta}\right) \qquad \frac{1}{\Delta} = \beta n_0, \tag{1.25}$$

with a peak position at z_0 and an amplitude n_0 related to its spatial width Δ by the parameter β. For exciton packets propagating below the critical velocity ($v < v_c$), the packet is then predicted to travel diffusively through the crystal with a particle density described by the solution of a 1D diffusion equation with a drift term.

In previous experimental works [15, 16], theoretical predictions of Loutsenko and Roubtsov in [29] have been verified. Exciton packets are observed to travel diffusively through the sample below the predicted critical velocity when having relatively low exciton densities. Packets formed at higher excitonic densities condense and travel ballistically at velocities between the critical velocity "v_c" and the velocity of sound "v_s". The detected condensates were successfully fitted by the soliton distribution provided in eq.1.25. However because of the presence of an incoherent tail formed behind the travelling condensate (coherent), a slight modification of the soliton shape was brought forth in [30]. This theory is consistent with the comet analogy for the travelling condensate, first mentioned by Benson [15]. According to the proposed model, the travelling packet consists of a condensed core, surrounded by a coma and followed by a tail of uncondensed excitons. Such a visualization of the exciton packet entity will be useful when discussing various packet induced phenomena, such as the formation of the secondary packet (section 3.1.3).

1.4 Condensate Amplification

As seen in section 1.1.1, bosons can have multiple occupancy in a given quantum state as opposed to fermions who obey Pauli's exclusion principle (one fermion per state). A boson's probability to join a multiply occupied state, increases proportionally to the occupation number of the final state. Therefore a larger boson occupancy in the final state will result in a "quantum attraction" behavior, similarly to the case of the amplification of photons (which are bosons) by stimulated emission (LASER). Somewhat analogous to the case of stimulated emission in a laser, the presence of optically inactive paraexcitons can stimulate the amplification process of a condensate formed of paraexcitons .

Spontaneous exciton scattering process consists of the annihilation of an exciton with

energy E_i and wavevector $\vec{K}_i$, and the creation of an exciton of energy E_f and wavevector $\vec{K}_f$ and simultaneous absorption or emission of an acoustic phonon [22]. The latter describes an elementary three body process occurring when hot excitons are injected into the crystal. The initial exciton (E_i, $\vec{K}_i$) is coupled to a continuum of final states, defined by the set of vectors ($\vec{K}_f$, $\vec{q}$) which satisfy the energy and momentum conservation laws:

$$E_i = E_f \pm \hbar\omega_q \qquad \vec{K}_i = \vec{K}_f \pm \vec{q}, \tag{1.26}$$

with constraints:

$$E_{i,f} = \frac{\hbar^2 K_{i,f}^2}{2m_{eff}}, \qquad \hbar\omega_q = \hbar|\vec{q}|v_s, \tag{1.27}$$

where v_s is the longitudinal sound velocity and m_{eff} is the exciton effective mass. These spontaneous events lead to the diffusive transport of excitons, modeled by the diffusion equation.

For the case of a stimulated process, an incident exciton field (f_c, E_c, $\vec{K}_c$) induces the exciton scattering, where $f_c > 1$ is the occupation number of mode c. Additional conditions are prescribed for the direction and magnitude of E_f and $\vec{K}_c$ given by:

$$E_f = E_c \qquad \vec{K}_f = \vec{K}_c \tag{1.28}$$

The time rate of change of the average number of bosons in mode c gives the growth of the bosonic rate [31]:

$$\begin{aligned}\frac{\partial f_c}{\partial t} = \frac{2\pi}{\hbar}\sum_q \gamma^2(q)\{&f_{c+q}(1+f_c)[(1+f_q)\delta(\hbar\omega_q + E_c - E_{c+q}) + f_q\delta(\hbar\omega_q - E_c + E_{c+q})] \\ &-(1+f_{c+q})f_c[(1+f_q)\delta(\hbar\omega_q - E_c + E_{c+q}) + f_q\delta(\hbar\omega_q + E_c - E_{c+q})]\}\end{aligned} \tag{1.29}$$

where $f_i = f_{c+q}$ and f_q are respectively the occupation number of excitons and acoustic phonons with energy E_q and $\hbar\omega_q$ and $\gamma(q) = \gamma_0\sqrt{q}$ is the matrix element of the exciton-phonons interaction. An excitonic Bose condensate with $f_c >> 1$ on the R.H.S. of eq.1.29 can provide the triggering term for stimulated excitonic transition. Even below the Bose condensation threshold, stimulated exciton scattering can still occur since the modes near $\vec{K} = 0$ already have large occupation numbers in the quantum-degenerate statistical regime. In eq.1.29, the amplification process is expressed by the first term, while the second term of the equation represents the loss process. The amplification of

the exciton condensate is achieved through stimulated exciton scattering induced by the excitonic field (f_c, E_c, $\vec{K}_c$). The loss process occurs when excitons are scattered out of the mode f_c by the creation of excitons having a wavevector $\vec{K}_c \pm \vec{q}$. The dominating term (amplification or loss) of eq.1.29, dictates the overall occurring process. According to [32], stimulated emission of excitons can be observed at densities under the critical BEC density due to the non radiative nature of excitons. Such a process is seen during the formation of a secondary packet when a resonant beam stimulates the diffusive portion of the exciton condensate.

Chapter 2

Experiment

This chapter presents the experimental apparatus used to acquire measurements concerning Bose-Einstein condensation of Excitons.

2.1 Lasers

2.1.1 Pulsed Lasers

During BEC experiments the high density of excitons needed to form a condensate are optically created in the crystal by a high intensity Nd:YAG laser pulse (pump beam). The amplifying medium of a Nd:YAG laser consists of a Neodymium (Nd) doped Yttrium Aluminium Garnet (YAG) rod, in which the population inversion is triggered by a flash lamp. The Lumonics Nd:YAG laser used in the lab has a pulse width of $\Delta t \approx 10\,ns$ and emits at $\lambda = 532\,nm$ due to a frequency doubler.

The probe beam used to stimulate the travelling condensate during experiments is provided by a Lumonics Hyperdye 300 laser with a pulse duration of $\Delta t \approx 9\,ns$; the dye laser is pumped by the Nd:YAG laser. The dye laser was most often tuned at $\lambda = 609.51\,nm$, the 1S orthoexciton energy in Cu_2O at T=2K.

Radiation output of both lasers is vertically polarized. The laser peak power outputs were measured to be $3.5\,MW$ for the dye laser and $15\,MW$ for the Nd:YAG laser. The laser output peak power "P_{peak}" was measured in the following way:

$$P_{peak} = \frac{P_{avg}}{f\Delta t} \tag{2.1}$$

where P_{avg} is the average measured power on a conventional power meter, f is the laser

repetition rate ($10\,Hz$ in this case) and Δt is the pulse duration. In all of the experiments, both the Nd:YAG and dye lasers were simultaneously operational. Therefore, in order to properly pump the dye laser, only half (divided with a beam splitter) of the Nd:YAG laser was directly utilized. The effective peak power during experiments is approximately $7.5\,MW$ and $1.7\,MW$ for the Nd:YAG and dye lasers respectively. Whenever measurements are presented, the indicated peak laser intensities "I_{peak}", are defined as:

$$I_{peak} = P_{peak}/A_{spot} \tag{2.2}$$

where P_{peak} is as defined in eq.2.1 and A_{spot} is the spot size of the laser illumination. Throughout this thesis, peak laser intensities will be reported instead of peak laser powers. Intensities are generally given in units of "I_0", where $1I_0 = 10^5\,W/cm^2$. In eq.2.2, a gaussian beam cross section is not assumed, but rather a stepwise shaped (square) pulse profile. This would result in a considerable overestimation of the peak intensity if it weren't for the fact that the excitation apertures on the sample holder are considerably smaller than the laser beam's spot size, ensuring a fairly homogenous profile. To remain consistent with respect to the cross-sectional beam profile, laser intensity measurements were performed with a conventional power meter on an area comparable to the sample holder apertures.

The wavelength output range of the dye laser can be shifted to a spectral region of interest by simply modifying the dye mixture. The dye laser solution used for an output range of $605 - 610nm$, was a mixture of $87\,mg/L$ of Kiton Red 620 and $24\,mg/L$ of Rhodamine 640 in methanol. The laser average output power for various wavelength is presented in Figure 2.1. The power output is centered at the region of interest (resonance) of $\lambda = 609.51\,nm$, where the power profile is at its flattest; intensity variations related to laser tuning are therefore negligible in the vicinity of the 1S line.

2.1.2 Laser Beam Attenuation

To achieve sample illumination at various intensities, two methods are used to attenuate the laser beam. One method is the use of a stack of properly calibrated neutral filters, which provide attenuation over many orders of magnitude. These filters come in different optical density (OD) values such as OD = 0.2, 0.3, 0.5, 1.0, 1.5, and 2.0. If the filter is not perfectly perpendicular to the laser beam, a lateral displacement is induced, which is the major drawback of this method. Moreover, the filters generally do not have a

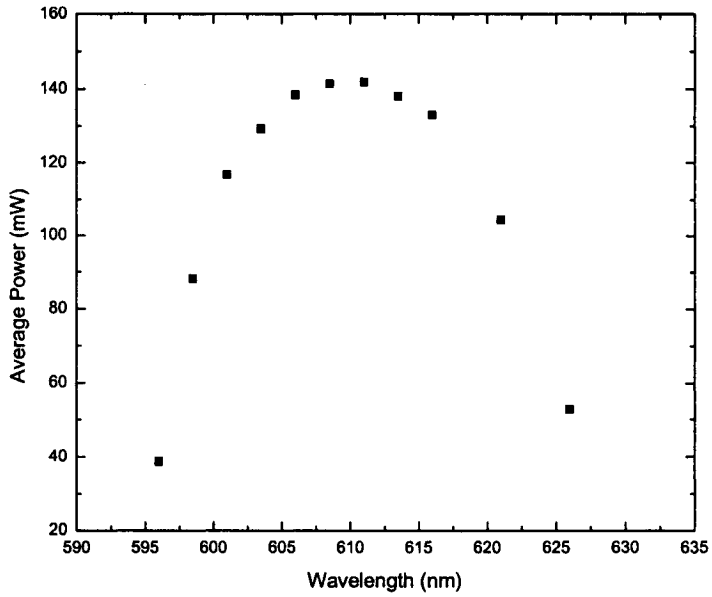

Figure 2.1: Pulsed dye laser average power variation over a range of output wavelengths.

uniform thickness producing a natural slant, making beam displacement inevitable.

A second method must then be used to attenuate the laser beam during experimental manipulations where constant beam position is critical. The method in question was achieved with a computer-controlled multi-prism optical attenuator, which doesn't deviate the laser beam (Figure 2.2). The Fresnel reflection equation for polarized light is the principle behind this device. The quartz wedge absorbs a negligible amount of light which is either reflected or transmitted, the transmission being a function of the incident beam angle. The beam deviation produced by the first wedge is cancelled by the second; and the beam offset produced is then cancelled by the second pair of two counter-rotating wedges. This method however is limited to an intensity variation of two orders of magnitude. The multi-prism attenuator is driven by a computer-controlled stepper motor and can lead to precise intensity dependent measurements once it is properly calibrated. The attenuator was installed at the dye laser output aperture in order to precisely vary the probing beam's intensity. At times, the laser intensities are presented in terms of optical density (OD) attenuation factors. These can be converted to actual measurements of intensity by this simple formula:

$$I = I_0 10^{-OD} \tag{2.3}$$

For instance, an OD of 0.3 corresponds to an attenuation factor of 2, while an OD of 1

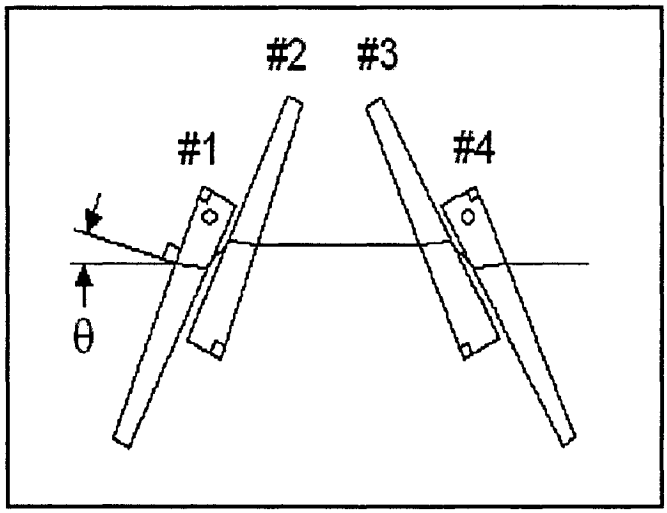

Figure 2.2: The quadruple-wedge optical attenuator.

corresponds to a factor of 10, etc...

2.2 Exciton-Mediated Photovoltaic Effect

Attempts to detect Bose-Einstein Condensation of orthoexcitons in Cu_2O by means of photoluminescence was deemed inconclusive [28, 10, 33, 34, 11]. The relatively short orthoexciton lifetime of $\tilde{}1\,ns$, poses a difficult challenge on using photoluminescence of orthoexcitons to study the BEC phenomenon in Cu_2O.

Paraexcitons have a much longer lifetime than orthoexcitons due to their low radiative efficiency: this enables the condensate to form and propagate from one edge of the crystal to the other. However, a non-optical detection method is required to observe condensates of paraexcitons. The detection method used during the experiments exploited the exciton mediated photovoltaic effect [35]. The latter was originally used in solar cells to extract electric energy from sunlight [36].

In earlier experiments, a semi-transparent gold layer is deposited on the front surface of the Cu_2O sample and a copper electrode is deposited on the back surface (Figure 2.3). The gold layer acts as an ohmic contact, while the copper layer is a rectifying contact where the respective Fermi levels at the Cu/Cu_2O interface line up and lead to a bending of the energy bands. The potential barrier (Φ_B) at the interface is of the order of $1\,V$ [37, 36], which results in a high electric field region of depth W ranging around

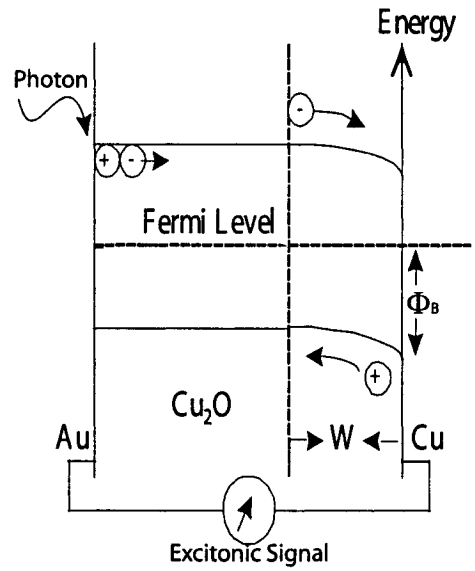

Figure 2.3: Schematic of the exciton-mediated photovoltaic effect.

$10 \ldots 100\,nm$ in Cu_2O [38]. The resulting static electric field within the depletion width $\Phi_B/W \approx 10^5 - 10^6\,V/cm$, is on the order of the required field to dissociate an exciton in Cu_2O ($\approx 10^6\,V/cm$). Therefore, a fraction of the excitons will be dissociated and detected as an external current.

The sandwich electrode configuration presented in Figure 2.3 can only be used at low laser intensity to prevent damage to the gold electrode. At low temperatures, the large series impedance ($\tilde{}10^9\Omega$) of the sample would result in long time constants for the detected signals; the nanosecond resolution needed for BEC observation would therefore be unattainable. To resolve this difficulty, the gold and copper electrodes were deposited in a ring configuration on the same sample surface as depicted in Figure 2.4. During BEC experiments, sample illumination was usually performed on the opposing or adjacent sample faces with regards to the electrodes. Several other types of electrode configurations were studied in [14], but the configuration illustrated in Figure 2.4 produced the best excitonic signals. The exciton detector's copper electrode has a diameter of 2mm (same as the laser spot size) and is surrounded by a gold ring (see section 2.3.3). The effective detector region generated by the Cu/Cu_2O barrier is $\approx \pi r^2 W$, where r is the Cu spot radius and W is the depth of the depletion width (high electric field region). The detector measures excitons having travelled through the crystal and into its effective region. Stray light caused by multiple reflections inside the cryostat results in a signal created by light becoming incident directly on the electrodes (see section 2.5.2).

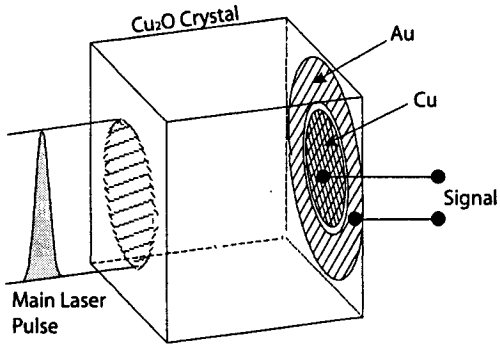

Figure 2.4: Electrode configuration for high intensity time-resolved photovoltaic detection.

A sturdy sample holder with a light cap to cover the exposed portion of the electrodes is required to correctly isolate the desired signal. Inevitably, a small amount of stray light still trickles through to the electrodes because of the internal reflections between the crystal and the sample holder (see Nd:YAG front signal in Figure 2.21).

The detector's linearity and efficiency were studied at $\lambda = 532\,nm$ by direct illumination of the electrodes [15]. The detector behaved linearly over a large range of laser intensities spanning many orders of magnitudes, where an efficiency of ~1% was measured for the on-electrode geometry. Due to losses in the sample an efficiency of ~0.1% was measured for the illumination geometry shown in Figure 2.4. These efficiency results are in agreement with those of solar cell researchers [40].

The linearity and efficiency of the detector under BEC experimental conditions (illumination not directly on the electrodes) is investigated in section 2.6.

2.3 Sample Preparation

This section presents the complete, step by step instructions for preparing our samples. It begins with a presentation of the samples themselves, followed by a description of the polishing, etching, and mounting techniques.

The samples used during the experiments performed for this thesis were high quality natural single crystals cut into a parallelepiped with nominal (100) crystal symmetry. Two Cu_2O samples of different dimensions were used (see Figure 2.5): Sample#1 had dimensions of $1.94 \times 3.60 \times 3.50 mm^3$, and Sample#2 had dimensions of $2.44 \times 3.76 \times 3.57 mm^3$.

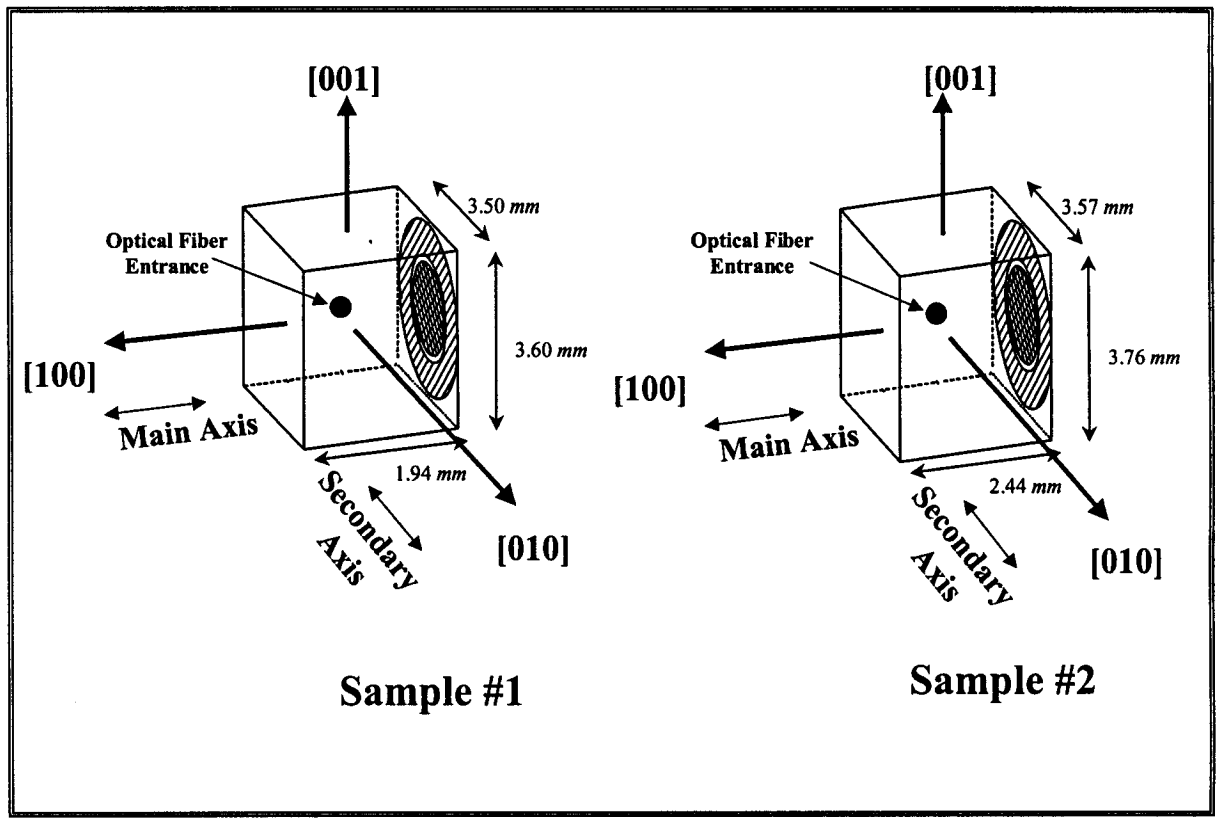

Figure 2.5: Dimensions of the two Cu_2O samples used during experiments. (Not drawn to scale)

1	▷ 12.5 μm Al_2O_3 powder on glass sheet with distilled water for $\sim 1\,min$, longer if epoxy and/or electrodes persist. ▷ Rinse with distilled water/methanol solution in ultrasonic cleaner. ▷ Wipe dry with tissue paper. *N.B: This step removes the greatest quantity of material. Since crystals are small, one should stop once previous electrodes/epoxy are removed.*
2	▷ 5 μm Al_2O_3 powder on glass sheet with distilled water for $\sim 1\,min$. ▷ Rinse with distilled water/methanol solution in ultrasonic cleaner. ▷ Carefully touch dry with optical tissue paper.
3	▷ 1 μm Al_2O_3 powder on glass sheet with no lubricant for $\sim 1\,min$. ▷ Rinse with distilled water/methanol solution in ultrasonic cleaner. ▷ Carefully touch dry with optical tissue paper.

Table 2.1: Guidelines for sample polishing.

2.3.1 Sample Polishing

In order to remove unwanted scratches and dents from the crystal faces, the samples must be polished. These surface defects provide local exciton disassociation points that reduce the efficiency of the exciton detector and dampen the creation of high exciton surface densities required for BEC experiments. Previous broken or damaged electrodes and leftover contact epoxy must be removed before depositing a new set. Table 2.1 presents the basic guidelines for sample polishing. Note that results and polishing times will vary with the operator's skill and experience.

All of the polishing is performed with the sample held down by the tip of one finger; no use of any particular type of holder is necessary. The polishing process is done by carefully moving the sample in a circular motion over the polishing elements. Applying unnecessary pressure to the sample during the polishing process is not recommended, as it increases the likelihood of polishing a preferred region (usually a corner) of the surface, resulting in a tilted crystal face. Sample viewing through a microscope will help determine when to change the powder; if polishing improvements are no longer visible, it is time to change the powder. A properly polished sample should demonstrate reflective surfaces.

1	▷ Rinse crystal in distilled water.
2	▷ Soak for $1\,min$ in methanol with final $20\,sec$ in ultrasonic cleaner.
3	▷ Etch for $3\,min$ in HBF_4 ($\sim 5\,\mu m/min$), then dilute quickly with distilled water.
4	▷ Repeat steps 1 and 2.
5	▷ Soak for $90\,sec$ in Bromine(2% vol.)/Methanol solution with final $30\,sec$ in ultrasonic cleaner.
6	▷ Repeat steps 2 and 5.
7	▷ Repeat steps 2 and 1. ▷ Quickly blow dry with He or N_2 to eliminate water spots.

Table 2.2: Guidelines for chemical etching.

2.3.2 Chemical Etching

Once the sample is correctly polished, chemical etching of the crystal is executed to remove the top atomic layers of the crystal faces that may have been damaged during the polishing. The etching process described in table 2.2 was developed by solar cell researchers and has been found to lower the surface recombination rate and maximize the barrier field at the Cu/Cu_2O interface [39].

After the sample has been etched, the crystal dimensions are carefully remeasured to get an idea on how much material was lost in the polishing and etching process. These remeasurements are important in determining the precise velocity of the condensate during experiments.

2.3.3 Electrode Depositions

Consisting of a deposited Cu disk surrounded by an Au ring, the exciton detector is designed to exploit the exciton mediated photovoltaic effect (section 2.2) for producing excitonic signals. To obtain the electrode pattern shown in Figure 2.4, the metal layers are deposited on a polished Cu_2O surface in three successive vacuum evaporations through carefully crafted masks. These masks are used to deposit two different materials within a separation of $250\,\mu m$, and prevent the overlapping of electrodes which would cause a short circuit. A mask holder having four posts is utilized to securely hold the mask in place during the evaporation process, while four teflon screws on the holder are used to align and hold the crystal in the mask's effective region. The evaporation of the gold ring

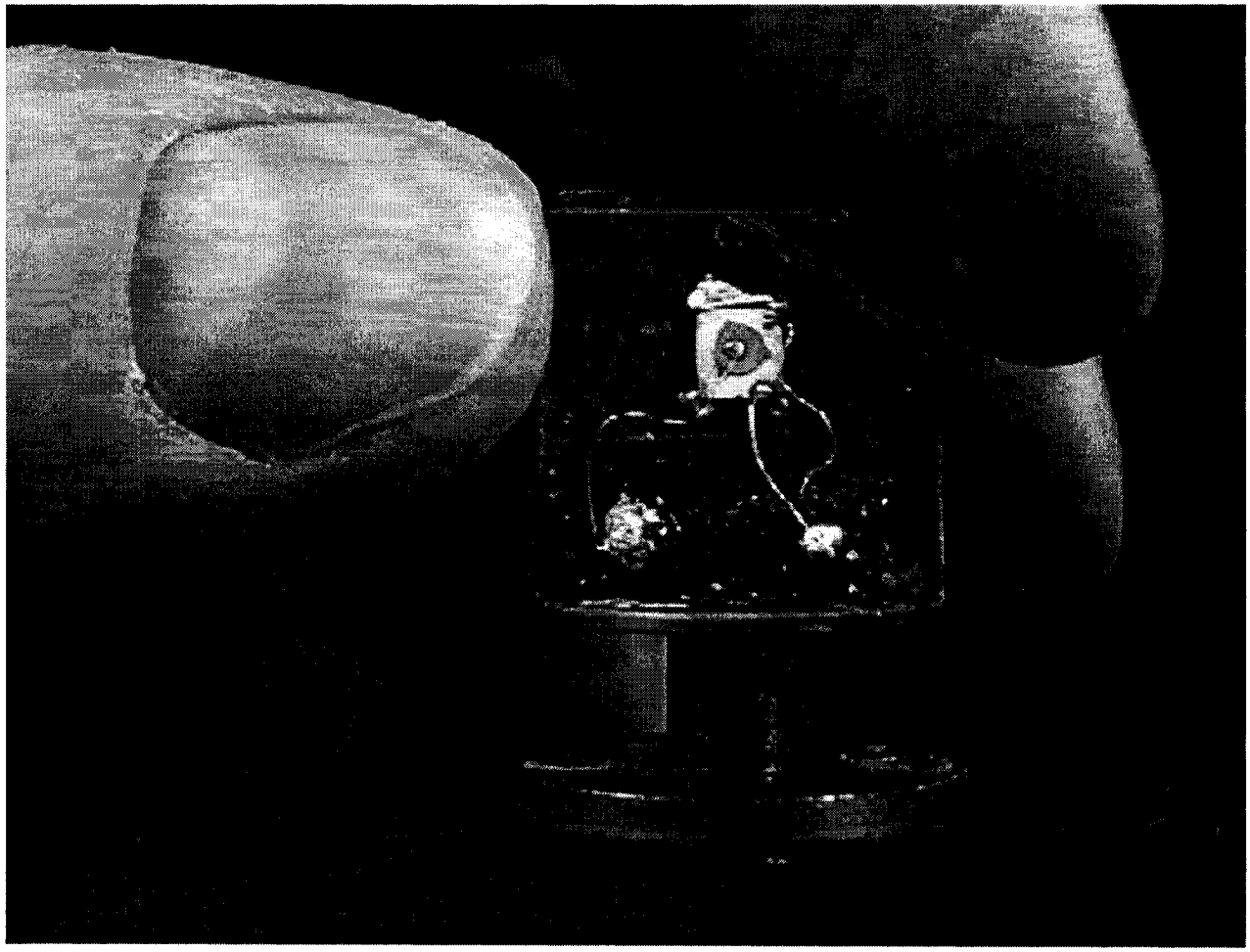

Figure 2.6: Cu_2O crystal mounted on a sample holder, depicting the Au (ring) and Cu (disk) electrodes. Gold wires are firmly fixed to the electrodes by a special conductive epoxy compound.

is done in two steps using the same mask. After the first evaporation, the mask consisting of a three-segment ring is rotated by 180^o, to close out the ring pattern. The copper disk is deposited with the use of a different mask, once the gold ring has been successfully evaporated. Each deposited layer has a thickness of $\sim 80 - 100\,nm$, enough to prevent penetration of the epoxy used to secure the electrical wire contacts (see section 2.3.4). The finished product (deposited electrodes) is shown on a mounted sample, connected with the gold wires (see section 2.3.4) in Figure 2.6.

1	▷ Put sample in sample holder. ▷ Secure with teflon tape without blocking the illumination aperture and conduits.
2	▷ Solder short gold wires to sample holder connectors.
3	▷ Form a small foot at the end of wires ▷ Position the wires on the electrodes.
5	▷ Use a small wire hook to drop epoxy at the foot of the wires
6	▷ Let cure for 3-4 days

Table 2.3: Guidelines for wire contacts.

2.3.4 Wire Contacts

The most delicate task during the whole sample preparation procedure was to properly attach the small gauge ($50\,\mu m$ diameter) gold wires onto the surface of the electrodes. To fix the gold wires onto the deposited material's surface, a two-part silver conducting epoxy (Epo-Tek H20E) was used. This epoxy compound cures at room temperature in 3-4 days, and can thereafter survive multiple thermal cycles ($T = 300K$ to $T = 2K$ and vice versa) while remaining intact and effectively conductive. Guidelines on attaching the wire contacts to the electrodes are summarized table 2.3.

The sample's dimensions compared to the size of human fingers are illustrated in Figure 2.6, clearly showing the level of difficulty in successfully fixing the wire contacts in the absence of any mechanical help. In doing so, the slightest hand movement usually sends the stiff gold wire into an oscillating mode, making it invisible to the naked eye until the oscillations cease. During this procedure, caution has to be taken in order not to mistakenly link both deposited metals (causing a short circuit) with the fluid expansion of the epoxy droplet upon surface contact; failure to do so would lead to the whole sample preparation process having to be restarted. After the contacts were successfully placed on the electrodes, and once the epoxy has had the time to properly cure, the gold wires are then soldered onto the sample holder's two metal posts (contact feed in Figure 2.7).

2.3.5 Sample Holder

While conducting experiments, a sturdy sample holder (Figure 2.7) is required to hold the samples immersed in superfluid helium. The holder is responsible for supporting the crystal and providing optical access to the sample without permitting stray light through to the electrodes. Note that the sample sits in the sample holder under no imposed stress,

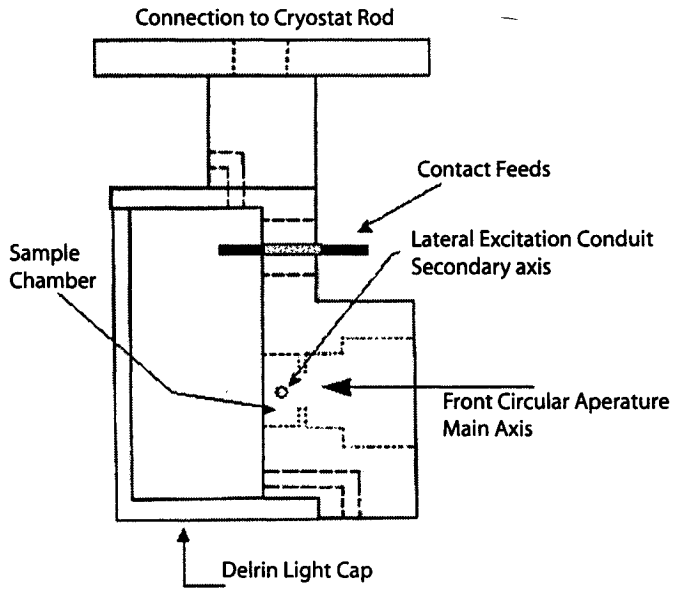

Figure 2.7: Sample holder schematic, as developed in [16].

nor is it attached with any glue which could possibly perturb the sample's surface. Teflon tape is used to secure the corners and edges of the sample to the holder. A delrin light cap was used to protect the exposed portion of the electrodes from parasitic light. In total, three sample holders were used: one was used to accommodate sample#1, while two others were used to conduct experiments on sample#2.

Sample#1 was placed in a holder having an optical access aperture diameter of 2mm for illumination along the main axis (see section 2.5). The optical access along the sample's secondary axis occurred through a circular conduit of 0.5mm in diameter. One of the holders used for sample#2 had the same optical aperture dimensions as in the latter holder, but had a total of three conduits (instead of only one) placed in a vertical configuration (see Figure 2.8). The sample holders presented thus far were made of copper. The other sample holder used with sample#2 however, was constructed out of brass (see Figure 2.9); being easier to machine compared to copper, it facilitated the drilling of five small conduits (0.3mm) for optical access with a separation of 0.2mm. The brass sample holder had a main axis optical access diameter of 3.5mm. All sample holders were built by the Science faculty's machine shop, including the remarkably precise work done by François Saumier on the brass sample holder.

Directly across from the circular conduits used for secondary axis illumination, other

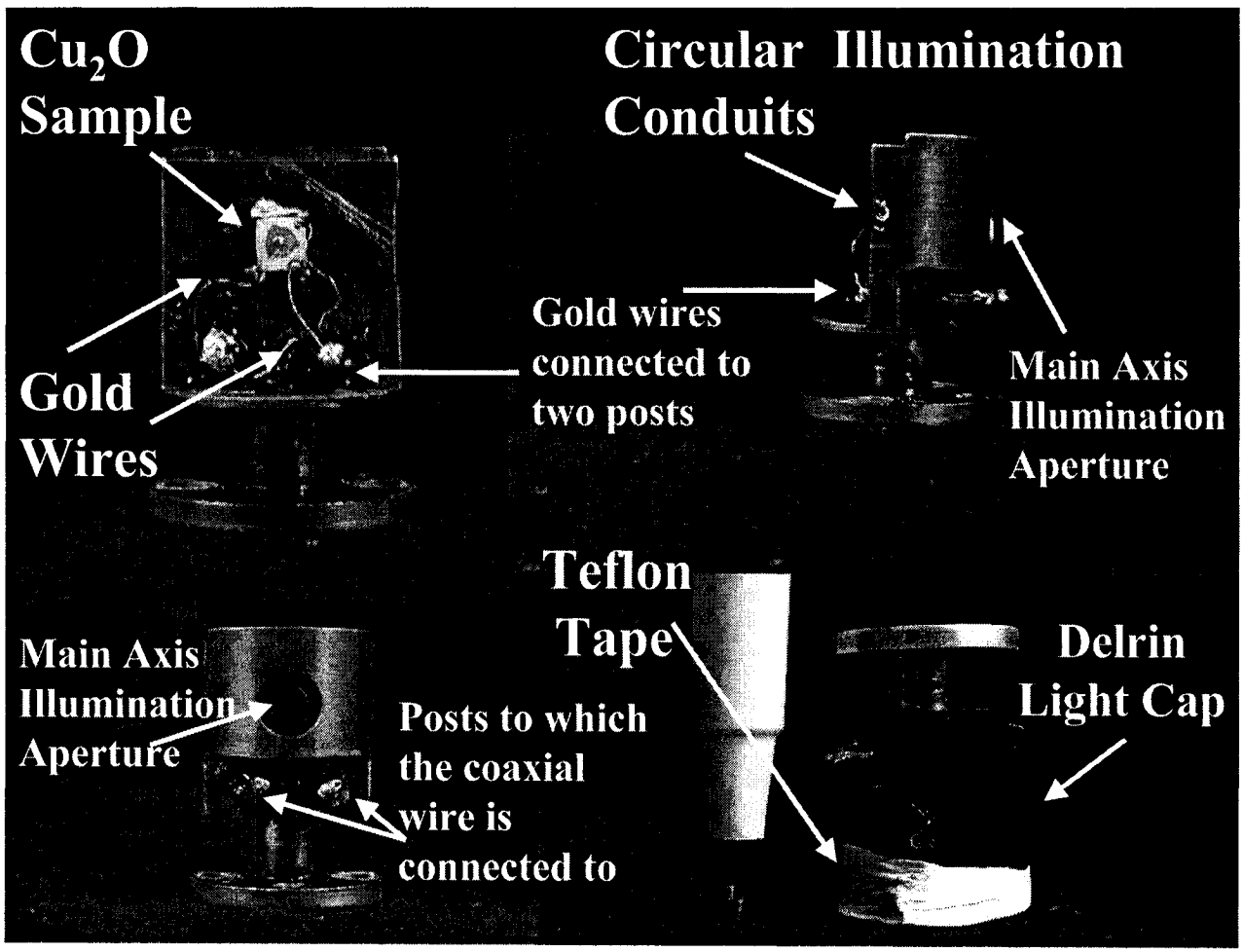

Figure 2.8: Copper sample holder with three illumination conduits. Sample#2 was placed in this holder for most of the experiments

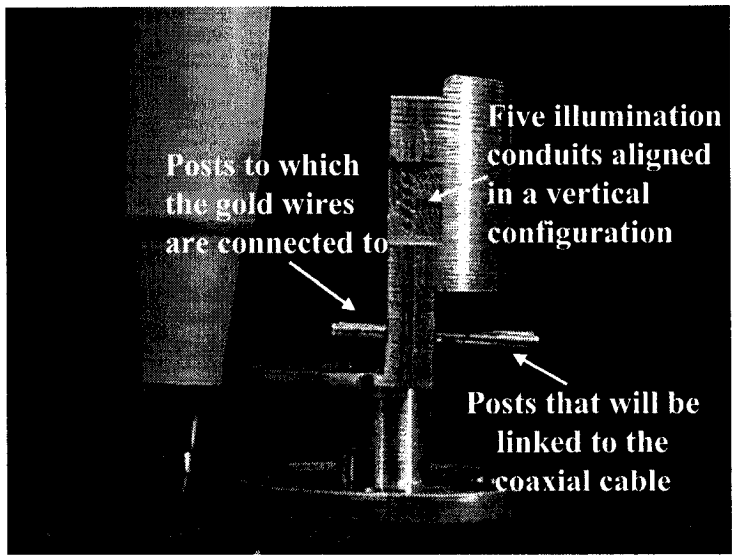

Figure 2.9: Brass sample holder with five illumination conduits; this holder was used to support Sample#2 for several experiments.

conduits were drilled in order to insert the light-collecting end of the optical fibers. These fibers were used to collect the unabsorbed light leaving the sample and direct this light towards an external photodetector (see section 2.4.3).

The excitonic signals transferred from the exciton detector (section 2.2) were captured by two posts (electrically isolated from the holder) linked to a coaxial cable connected to an exterior data acquisition system (section 2.4.2).

Once the crystal is mounted on the sample holder and all the necessary preparations are done, the sample holder is secured to a cryostat rod made of Invar, which is then used to lower the sample into the appropriate position inside the cryostat. Teflon tape is used to secure the light cap in position.

2.4 Experimental Setup

2.4.1 Optical Cryostat

Unless indicated otherwise, all results presented in Chapter 2 and 3, were obtained from experiments performed at superfluid helium temperatures ($T \cong 1.8 - 2K$). Such low temperatures were achieved through evaporative cooling: pumping on the liquid He in the optical chamber through the sample's access tube brought helium to temperatures below its lambda point of T=2.17K.

The cryostat used during experiments is a Janis Research model 8CNDT. It provided optical access through four windows, each consisting of two vacuum spaced fused quartz plates. The cooling system is equipped with two heaters, a computer-controlled valve for the pumping port, and a needle valve controlling the liquid He flow in the sample chamber.

Two sensors mounted in the cryostat provide the temperature reading. One is mounted inside a copper cylinder slightly above the sample holder, while the other sensor is mounted at the bottom of the cryostat's sample chamber. The two sensors are silicon diodes which have a temperature calibrated resistance. A small electrical pulse sent to the sensors by the temperature controller unit determines the resistance. The measured resistance is then converted to a temperature value through pre-programmed calibration charts.

2.4.2 Data Acquisition

Time-resolved measurements were all acquired with a digitizing oscilloscope (Tektronics model 620b), featuring two 500 MHz channels each capable of acquiring 2 $G\,Sample/s$. Two additional channels (auxiliary) also having a bandwidth of 500 MHz, have a maximum sampling rate of 500 $M\,Sample/s$. One of these auxiliary channels was used for triggering purposes. All channels were operated at a 50 Ω load resistor and provided time-resolved current measurements. The traces appearing on the oscilloscope are averaged over many laser pulses (~100 pulses), to reduce random background noise. After adequate averaging, traces are transferred from the oscilloscope to the computer via a GPIB interface card.

Raw data acquired by the computer can be analyzed by a computer program (TEK) which automatically subtracts averaged background signals that could not be removed through averaging (equipment-induced). As opposed to some results presented in the past [15, 16], none of the results in this thesis were modified with a data smoothing algorithm. In fact, smoothing algorithms tend to round off and broaden sharp peaks and even eliminate fine structures.

After the background has been subtracted from the concerned traces, the TEK program creates an ASCII formatted output file, compatible with most spreadsheet and graphing software such as Microcal's Origin .

The program TEK (coded in Visual Basic by Eric Benson) controls the two stepper motors (pumping valve and quadruple quartz wedge attenuator), transfers the data from

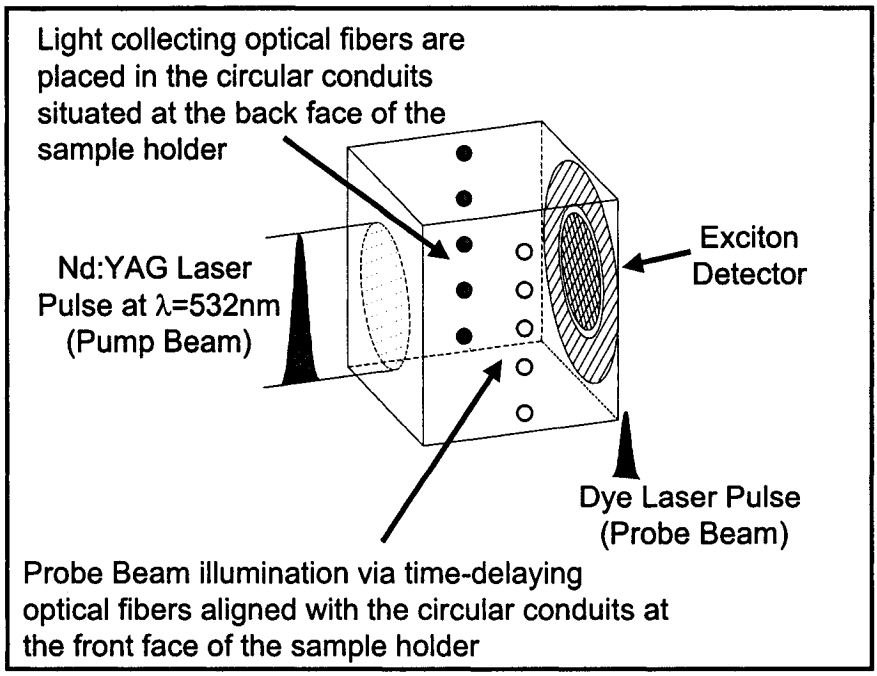

Figure 2.10: Positions of the optical fibers used for two purposes: 1)Light-collecting; 2) Time-delaying.

the oscilloscope, controls the movement of a spectrometer, takes spectra from a lock-in amplifier or the oscilloscope. It also displays and manipulates the data in multiple graphical windows.

2.4.3 Detectors, Optical Fibres, and Connectors

In our experimental setup, optical fibers were used for two purposes: 1) as a collecting and propagation medium for light transmitted through the Cu_2O sample; the transmitted light is directed towards an external photodetector; 2) as a time-delaying medium (optical path difference) of the probing laser pulse with respect to the pump beam laser pulse.

The light collecting optical fiber's cleaved ends are in contact with the sample inside the cryostat and were secured in the vertically positioned conduits (Figure 2.10) at the back face of the sample holder. The opposite ends of the fiber were coupled to a photodetector outside the cryostat. The series of vertical conduits were placed at the longitudinal center of the crystal. Collecting fibers permitted transmission measurements, which lead to the observation of normalized differential attenuation (NDA). The illumination conduits were placed directly across from the collecting fiber positions on the opposite side

of the sample, as shown in Figure 2.10. Note that the sample holder for Sample#1 had only one set of conduits, while the copper sample holder for Sample#2 had three sets also aligned vertically (Figure 2.8). Multiple conduits in a vertical configuration were used to obtain spatially resolved NDA measurements. The brass sample holder (Figures 2.9 and 2.10) yielded the best spatial resolution due to the larger number of conduits (5 compared to 3), having a smaller diameter (0.3mm as opposed to 0.5mm). A much better resolution could potentially be reached with the use of an array of many optical fibers. However, due to the severe bending required to insert the fibers inside the cryostat, the array's lack in flexibility, compared to single fibers, would prevent it to be used with our current experimental setup. A bigger cryostat (with a larger sample chamber) would better accommodate the needed room to allow a modest bending of the optical fiber array, as it is placed correctly in contact with the sample.

In relation to the severe bending conditions encountered by fiber inside the cryostat, a certain amount of radiation is lost. However, since the NDA is a relative measurement (ratio of two measurements), this loss does not influence the results. More so, the optical fibers sometimes broke due to the extreme temperature cycles; frustrating at times, the breaking of the fibers would usually occur during the last cooling stage right before experimental manipulations were set to begin. In such an event, NDA measurements could not be taken.

As mentioned earlier, optical fibers were also useful in establishing a time-delay between the probing beam (dye laser) and the pump beam (Nd:YAG laser) pulses. Different time delays permitted the probing of various longitudinal portions of comet-like structure. i.e. The probe beam could be deliberately delayed to meet the center portion of the travelling exciton packet inside the crystal. Various time delays were achieved by launching the dye laser beam into optical fibers of different lengths. In earlier years, during the research work of E. Benson, time-delays between two pulses were performed by sending one of the laser pulses outside of the laboratory and into the building's hallway, where it was reflected back and forth a few times depending on the desired time-delay, and thereafter directed back into the lab. Numerous optical fiber lengths were used, corresponding to time delays varying from $\delta t = 50ns$ to $\delta t = 2000ns$.

Optical fibers used for both applications (light collection and time-delaying) were multi-mode fused silica fibres with a core diameter of $200\,\mu m$. The end of the light-collecting fibers situated outside the cryostat were equipped with FC (Face Contact) fiber connectors; the connectors permitted the fiber to be appropriately coupled to a photodetector. The photodetector (New Focus, model 1621) relayed the detected signal

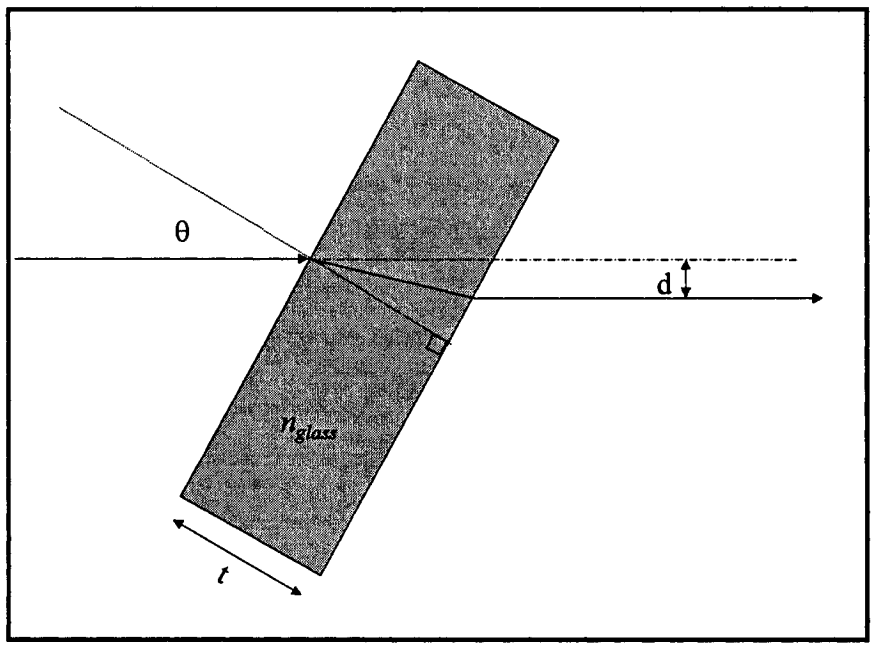

Figure 2.11: Beam displacement with glass plate

to the digitizing oscilloscope. Time-resolved traces were then analyzed as described in section 2.4.2.

After the fiber launched laser pulse leaves the fiber near the cryostat windows, it is collimated and directed towards the circular conduits on the sample holder, through which the sample is illuminated. In some cases, the probing beam's polarization was of importance (light exiting the multi-mode fibers is essentially arbitrarily polarized) as in section 3.2.6. The beam was re-polarized with a linear polarizer while a $\lambda/2$ plate was used to rotate the beams's polarization axis.

For results obtained in Figure 3.27, the Nd:YAG laser pulse was vertically displaced with the use of a tilted silica plate, (see Figure 2.11). The silica plate of thickness $t = 6mm$, was mounted on a graduated holder which was used to determine the tilt angle. The tilt angle "θ" was then converted to the beam displacement "d" with the following equation:

$$d = t \cdot \sin\theta \cdot \left(1 - \frac{\cos\theta}{\sqrt{n_{glass}^2 - \sin^2\theta}}\right) \tag{2.4}$$

where n_{glass} is the index of refraction of silica.

This method displaced the beam, parallel to the original beam. The Nd:YAG laser

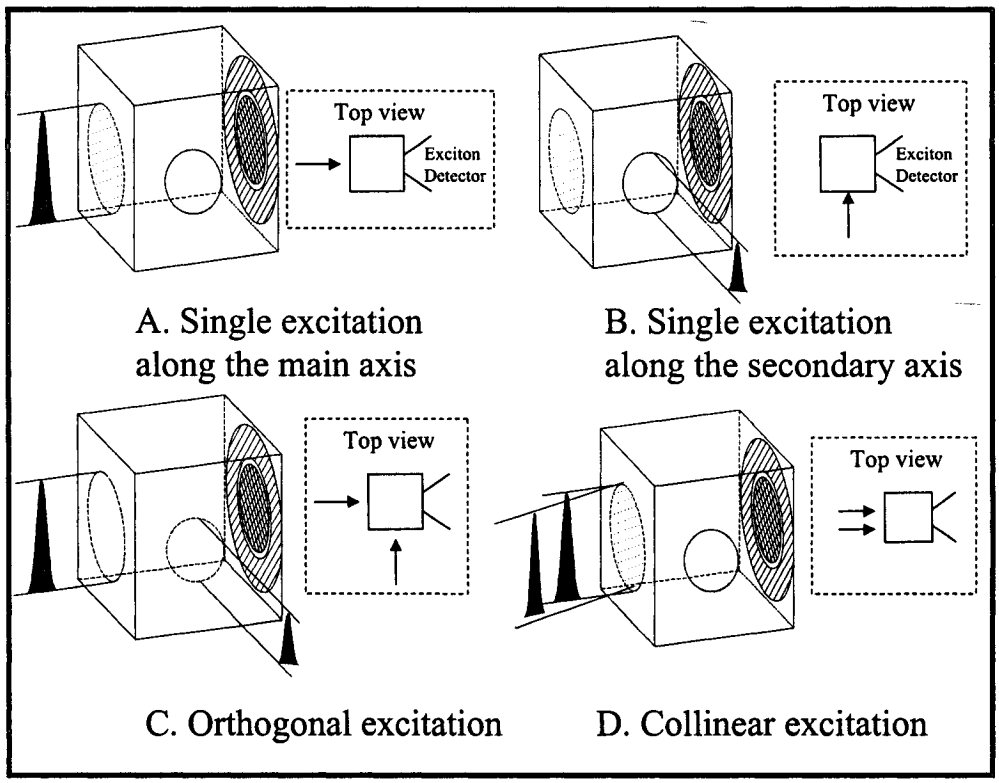

Figure 2.12: Various excitation geometries

beam diameter was reduced with the use of a pinhole.

2.4.4 Excitation Geometries

Results presented in this thesis were obtained from laser excitations in different geometries. In order to prevent repetitive, long explanations each time a result is presented which could lead to confusion, the terms describing the excitation geometries are clearly explained here. The different excitation geometries are illustrated in Figure 2.12 along with their corresponding top-view representations, which are shown on most graphs. Note that for simplicity, illumination conduits were omitted in Figure 2.12. The simplest excitation geometry occurs when a laser pulse is incident on the main axis (please refer to Figure 2.5 for sample axis identification) as shown in Figure 2.12-A. The excitonic packet is created in this geometry when a Nd:YAG laser pulse is used as the excitation source. Some experiments were also performed with the dye laser in this excitation geometry, but usually the dye laser excitation occurred along the secondary axis as shown

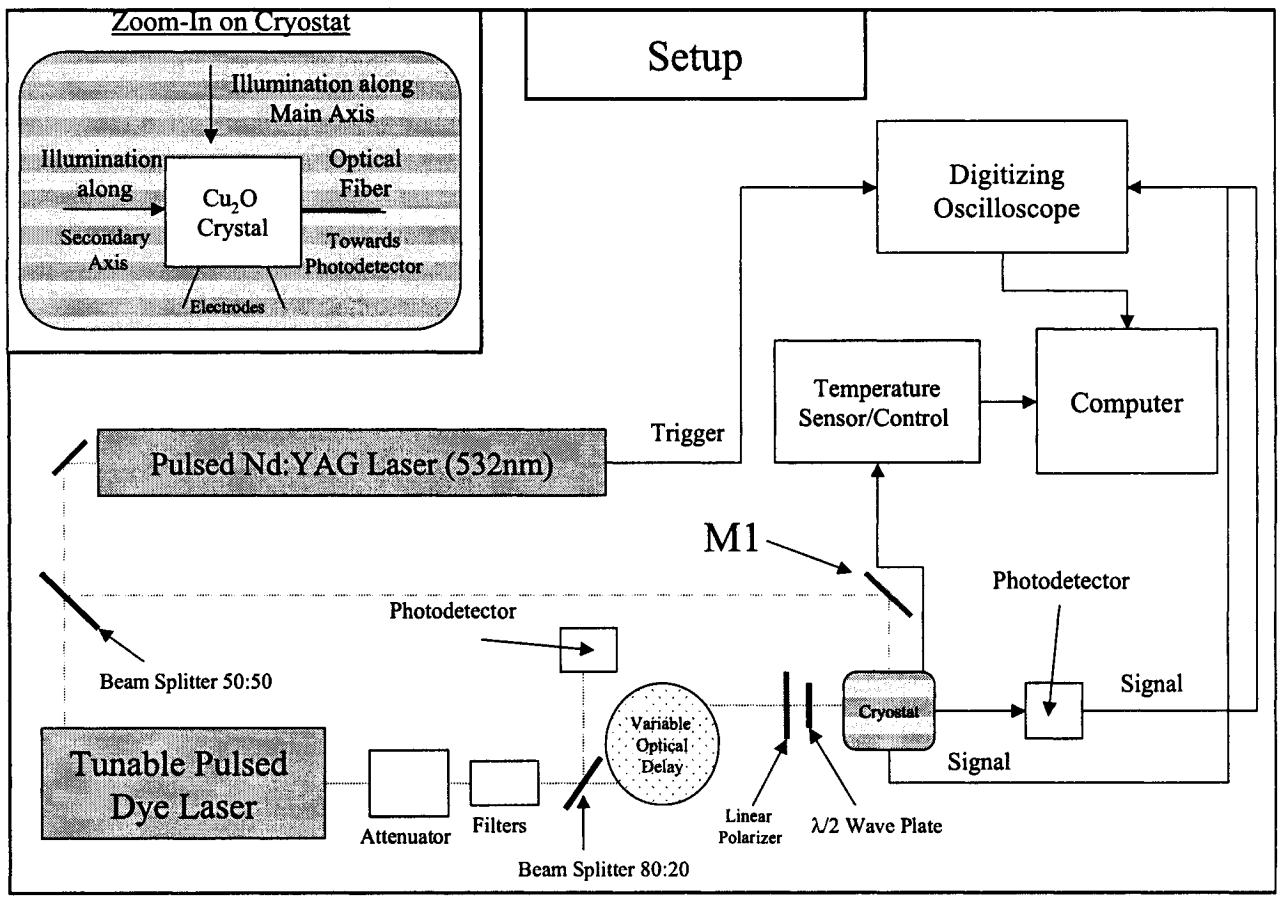

Figure 2.13: General experimental setup

in Figure 2.12-B. The orthogonal excitation takes place in such a geometry where the packet-creating Nd:YAG laser is incident along the main axis, while the probing beam is incident along the sample's secondary axis (Figure 2.12-C). The collinear excitation geometry is illustrated in Figure 2.12-D, and arises when both laser pulses are incident along the main axis.

A simplified representation of the complete experimental setup is depicted in Figure 2.13. The Nd:YAG laser output is separated into two beams by a 50:50 beam splitter designed to operate at $532\,nm$. One beam is directed toward the cryostat and incident along the main axis of the crystal which creates the initial exciton packet. The other beam is sent to pump the dye laser, where it generates pulsed radiation near the 1S orthoexciton resonance (see section 2.1.1). The dye laser pulses go through the computer-controlled multi-prism attenuator (and neutral density filters if needed), providing a precisely variable excitation intensity. The dye laser beam can then be launched into an optical fibre (of variable length) providing various time-delays with respect to the initial Nd:YAG laser pulse. At the fiber exit, the beam is collimated and incident through the sample holder's circular excitation conduits. If polarized light is needed, it is transmitted through a linear polarizer followed by a $\lambda/2$ plate in order to be able to vary the beam's polarization axis. The light transmitted through the sample can then be collected via the optical fiber situated inside the cryostat, directly across the crystal from the appropriate excitation conduit (see section 2.4.3). To monitor any laser fluctuations, a 80:20 beam splitter reflects 20% of the dye laser beam towards a photodetector, before it is launched into the fiber. In order to achieve collinear excitation, two plane mirrors are used to deviate the dye laser beam towards mirror "M1".

2.5 Basic Time-Resolved Signals

Two different detectors were utilized to obtain time-resolved signals. As indicated in section 2.4.3, a photodetector manufactured by New Focus coupled to an optical fiber, is used to detect the light transmitted through our sample, while deposited Au/Cu electrodes forming an ionizing Schottky barrier, were used to detect excitons in the vicinity of the copper electrode surface. Signals from both detectors correspond to a variety of phenomena ranging from the simple transmission of light through the sample, to the time distribution of migrating excitons of various regimes. Such regimes include the coherent excitonic packet, as well as the exciton gradient generated by resonant pulse excitation.

These time-resolved measurements were used to characterize important mechanisms taking place inside the sample, such as the amplification of the travelling exciton condensate due to an interceptive and resonant pulse which is subsequently attenuated. To validate these interpretations, linearity and efficiency tests were performed on both detectors in question.

2.5.1 Transmission Signal (Photodetector)

Amongst the two detectors used, the signal output from the commercially manufactured photodetector is most easily interpreted, since it is only directly sensitive to light and not to excitons in the sample. When taking measurements, this detector is coupled to an optical fiber exiting the interior of the cryostat, while the other end (light-collecting end) of the fiber is in contact with the Cu_2O sample inside the cryostat. Such a method of measuring transmitted light has proven to be quite useful, allowing measurements of the exciton packet-induced attenuation of the lateral pulse. The time-resolved signal produced by this detector is shown in Figure 2.14 to have a FWHM of ~10ns, limited by the dye laser pulse duration of 10ns. This measurement indicates a detector response time equal or lower than 10ns, consistent with the detector's accepted value of 5ns. The time at which the signal's peak appears (~120ns in the case of Figure 2.14), can be varied by modifying the secondary beam's time delay (see section 2.4.3) with respect to the trigger signal.

2.5.2 PV Signal (Exciton Detector)

The most important means of detection during our experiments was achieved through the exciton mediated photovoltaic effect. As described in section 2.4.3, two electrodes, copper (rectifying contact) and gold (Ohmic contact), were deposited in a ring configuration on one of the sample's faces. Migrating excitons resulting from laser illumination are dissociated (ionized) upon arriving in the vicinity of the barrier's depletion width, where a strong localized electric field is present. The deposited electrodes have the advantage of being able to detect migrating excitons in addition to electron-hole pairs resulting from incident light on the Cu electrode. This classifies the exciton detector as being quite unique, in the sense that it can be used for detecting optically inactive and electrically neutral particles, such as the paraexcitons in Cu_2O. However, the signal generated by the exciton detector is generally more difficult to interpret than its all-optical counterpart (section 2.5.1). In particular, the time-resolved signal corresponding to the 1S resonance

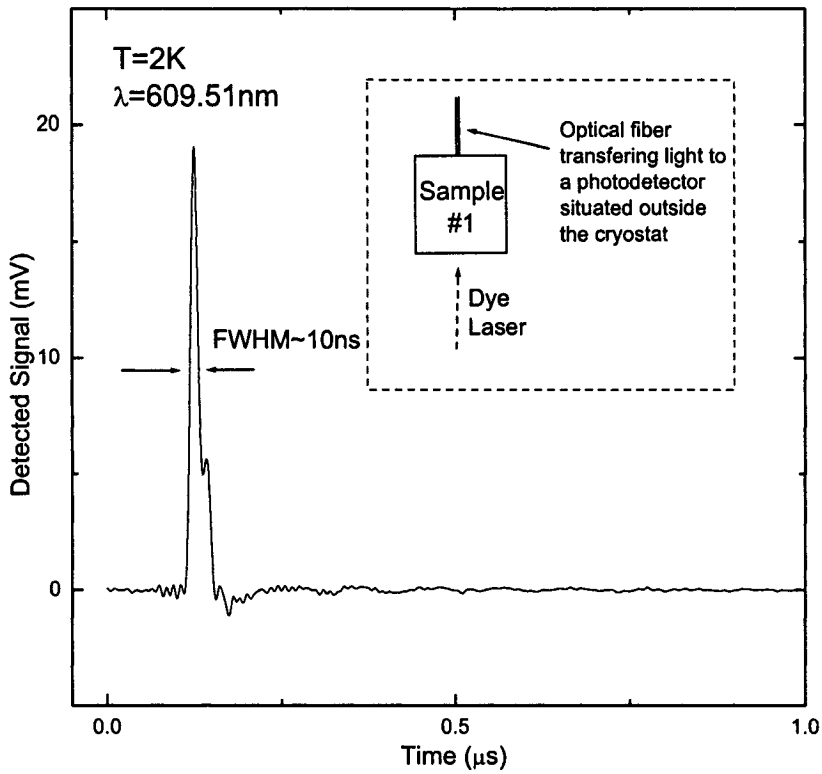

Figure 2.14: Time-resolved transmission signal resulting from a resonant pulsed illumination ($\lambda = 609.51\,nm$), incident along the sample's secondary axis. Light transmitted through the sample was collected and transmitted towards an external photodetector via an optical fiber where light was detected. The signal's FWHM corresponds to the laser pulse duration of 10ns.

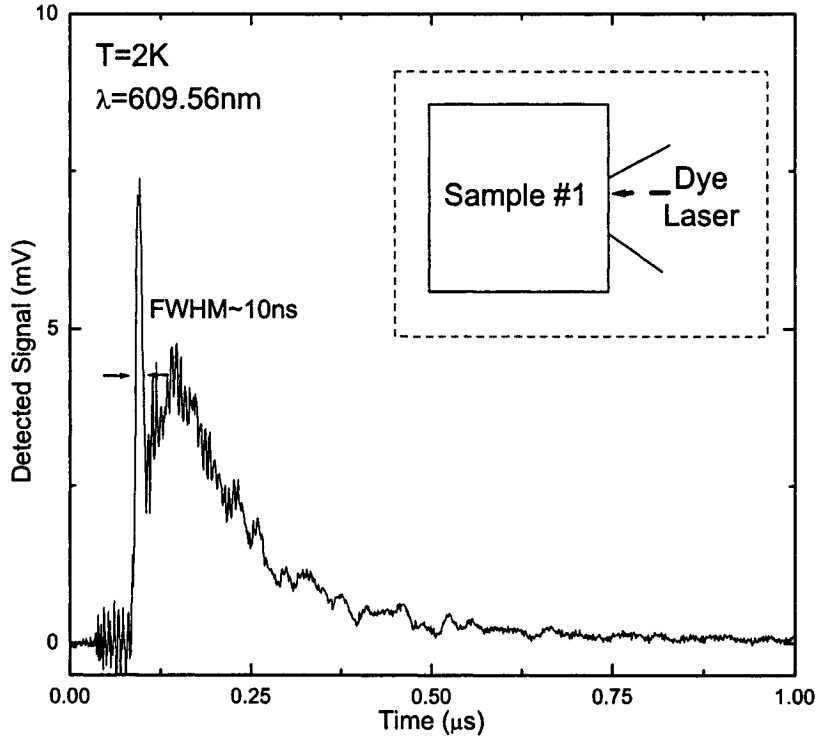

Figure 2.15: Time-resolved "front" signal corresponding to a slightly off-resonant ($\lambda = 609.56\,nm$) pulsed laser illumination, incident on the exposed face of the exciton detector (deposited electrodes). Two signal components (metallic and exciton) are clearly depicted. The "metallic" signal has a FWHM of ~10ns corresponding to the laser pulse duration of 10ns. The broad signal is the result of migrating excitons.

("front" signal) contains several undistinguishable signal components, often making the analysis nontrivial. These components can be discernible under slightly off-resonant excitation. For this reason, we begin our PV signal analysis with a signal (Figure 2.15) corresponding to a slightly off resonance excitation (λ = 609.56nm), in the vicinity of the 1S orthoexciton energy (λ = 609.51nm). The pulsed excitation was aimed at the normally unexposed surface of the exciton detector.

One of the signal components seen in Figure 2.15 is a relatively sharp signal (FWHM ~10ns) which is caused by incident light on the copper portion of the electrode's surface. This signal component, also referred to as the "metallic" signal in [19], occurs when the incident light has sufficient energy to excite electrons from the metal above the Schottky barrier. After being excited above the barrier height, the electrons leave the copper surface and contribute to the electrical signal viewed in Figure 2.15. The signal's FWHM

of ~10ns, is equal to the laser pulse duration, and indicates that under those conditions the PV detetector's response time is equal or less than ~10ns. It is important to point out that this so-called "metallic" signal has no significance to the study of the BEC phenomenon. In fact under resonant excitation, the metallic signal component becomes negligible when compared to the exciton signal component. This signal component is therefore not directly relevant to the work presented in this thesis, but due to its presence in the acquired measurements, it was necessary to acknowledge and explain its existence.

The second component observed in the time-resolved PV signal shown in Figure 2.15, corresponds to excitons created below the sample surface by the resonant portion of the laser illumination. With a spectral bandwidth of 0.02nm, the dye laser still emits a small amount of resonant radiation despite being tuned at an energy lower than resonance (λ = 609.56nm), thus having the ability to create ortho-excitons. A certain amount of excitons created in close proximity of the detector migrate towards the sample surface where the electrodes lie and produce an electrical signature upon being ionized by the strong electric field in the depletion width. Compared to the previously mentioned "metallic" signal, the latter signal is much broader due to various arrival times of the migrating exciton population. Assuming excitons created by resonant light have a constant migration velocity for a given laser intensity, the distance from the detector at which the excitons were created can be related to their time dependence. In the particular case of Figure 2.15, the majority of excitons arrive at ~52ns with respect to the initial incident light, indicating that most of these excitons were created at a depth of ~110μm in the sample (assuming an exciton migrating speed of ~2150m/s for the diffusive transport regime).

In a different aspect of the experiment using the same excitation geometry as in Figure 2.15, a completely off-resonant Nd:YAG laser pulse (λ = 532nm) is employed to once again intentionally illuminate the exposed surface of the electrodes. The resulting signal is shown in Figure 2.16, where only a sharp peak (FWHM~ 10ns) is observed due to the locally created excitons.

Since illumination radiation at λ = 532nm is not in resonance with any specific excitonic energy levels, exciton creation must occur through multiple transitions. The Nd:YAG laser pulse having an energy above the Cu_2O bandgap first creates electron-hole pairs high in the band upon absorption in the sample. Through a series of phonon emitting decays, these electron-hole pairs are converted to orthoexcitons. The short-lived orthoexcitons in turn decay down (~12meV) to a more stable paraexciton state. The whole decay process occurs on a time scale of picoseconds [14]. The question now, is if

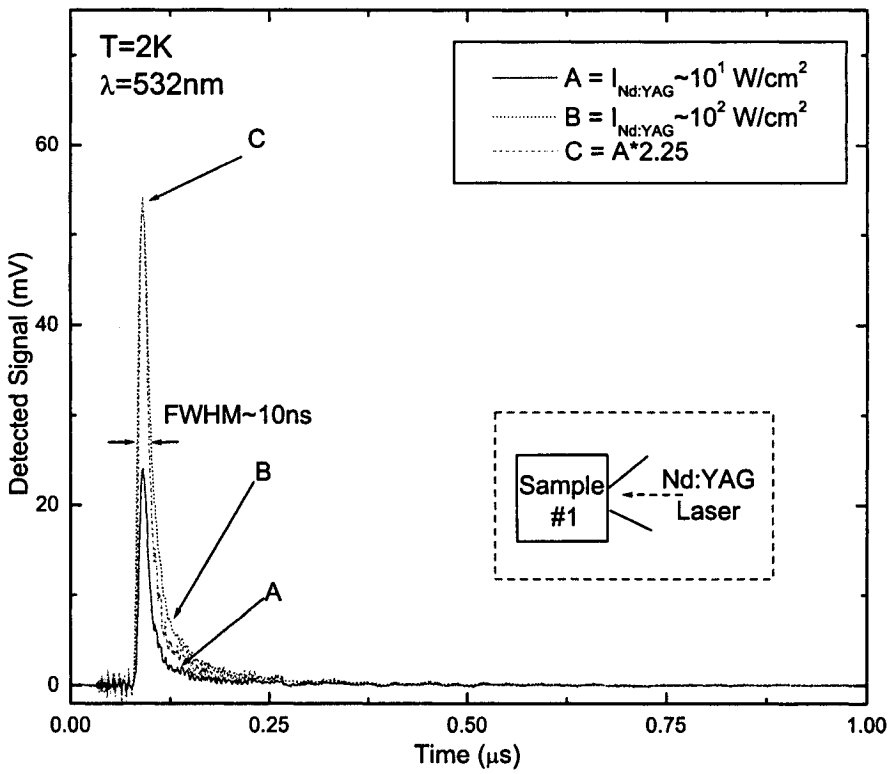

Figure 2.16: Time-resolved signals resulting from a Nd:YAG laser pulse incident on the back face of the electrodes. Signals (A and B) are shown for two laser intensities, while the third signal (C) is normalized to match signal B's amplitude.

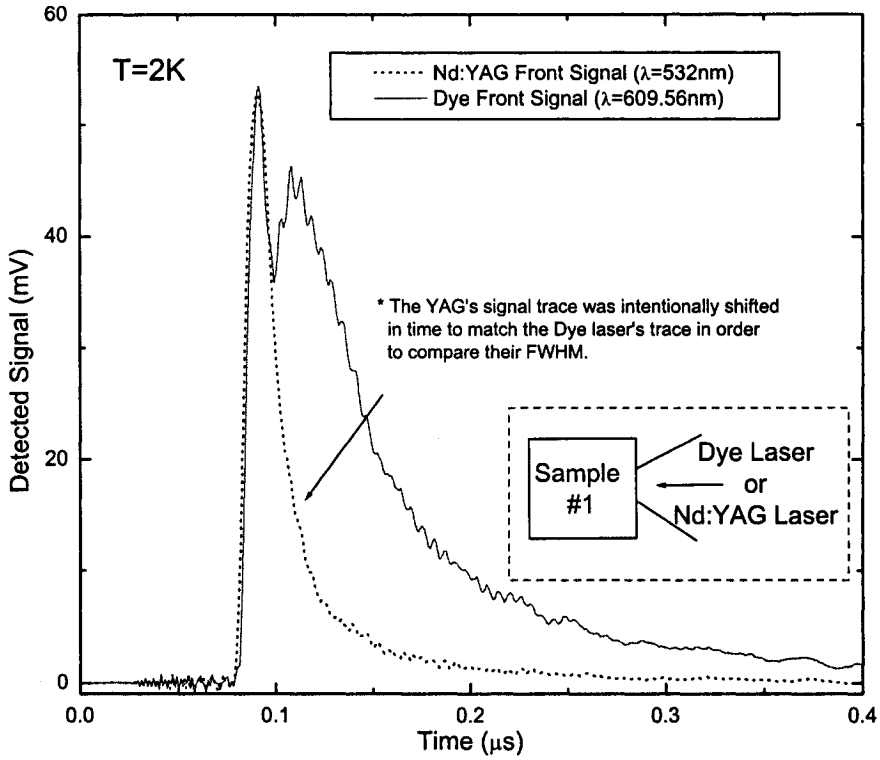

Figure 2.17: Time-resolved dye laser "front" signal in the vicinity of the 1S line, compared to the Nd:YAG laser "front" signal. Both laser excitation were performed on the back side of the exciton detector.

the Nd:YAG pulse is able to create excitons, then why don't we observe (in Figure 2.16) a wider signal to take into account exciton migration times? In reality, the relatively high absorption coefficient value of Cu_2O at this wavelength ($\alpha = 3 \times 10^3 cm^{-1}$) prevents radiation from penetrating more than a few micrometers from the sample's surface, resulting in a localized region where excitons are created. In this case, excitons are created relatively close to the detector and have little to no distance to cover before entering the detector's effective region, which yields a sharp time signal (FWHM~10ns) measurement. This time-resolved signal indicates once again that the exciton detector's response time has an upper limit of ~10ns. According to Figure 2.16, the signal's width is preserved regardless of the laser pulse intensity. This occurrence is not surprising since the radiation's penetration depth (first order absorption coefficient) is not intensity dependent, but rather wavelength dependent.

To further reinforce the fact that the Nd:YAG front signal and the "metallic" component of the dye laser front signal both correspond to a localized mechanism, both signals

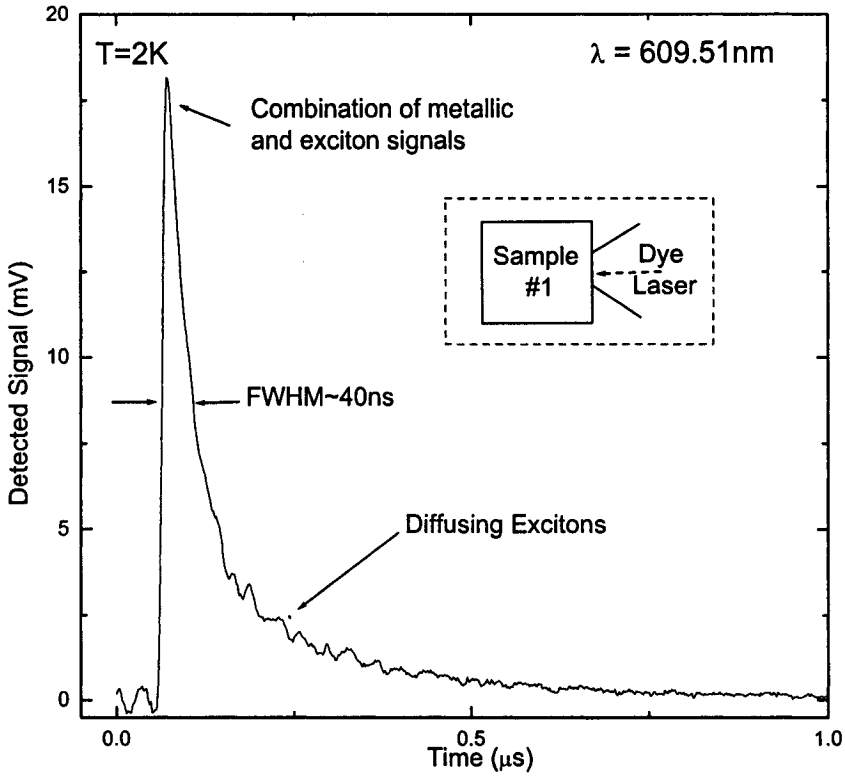

Figure 2.18: Time-resolved "front" signal resulting from a dye laser pulsed illumination tuned at the 1S orthoexciton resonance ($\lambda = 609.51$nm). Excitation is on the back face of the electrodes.

were superimposed in Figure 2.17. The Nd:YAG front signal was intentionally shifted and multiplied by a factor in order to correctly match both signals for comparison purposes. We see from Figure 2.17 that the Nd:YAG front signal fits quite well (same width) within the light induced component (metallic signal) of the signal produced from a slightly off-resonant dye laser illumination ($\lambda = 609.56$nm). However, the non-symmetrical shape (tail) of the Nd:YAG front signal provides evidence that an exciton component is present, clearly demonstrating that both sharp signals (Nd:YAG and metallic) are not due to the same physical mechanism.

Now that the front signal produced by an Nd:YAG laser pulse illumination and the signal by a dye laser illumination in the vicinity of the 1S resonance were both examined, the attention is shifted towards the time-resolved signal produced by a resonant pulse illumination. The resonant signal is of major interest since all studied phenomena stimulated by a secondary pulse of this nature yield the most spectacular effects. The previous statement is not surprising since resonant excitation corresponds to the most

efficient radiation for exciton creation (i.e. creates more excitons per pulse at a given intensity). The shape of the front signal resulting from a resonant pulse (Figure 2.18) displays a fast rise time, followed by an exponential-like decay. The fast rise time is mostly due to excitons created in the detector's effective region with a relatively small contribution from the "metallic" signal. The exponential-like decay on the other hand is solely due to the portion of excitons migrating to the detector's effective region. Unlike the signal observed in the vicinity of the 1S resonance ($\lambda = 609.56$nm), the signal at resonance shown in Figure 2.18 does not openly demonstrate two distinct signal components. The two signal components must therefore be superpositioned, and thus impossible to distinguish apart. The resulting superimposed signal has a FWHM of ~40ns, a signature of different arrival times of migrating excitons.

In order to visualize the evolution of the exciton and metallic components of the signals, time-resolved dye laser front signals were taken at various wavelengths in the vicinity of the 1S line (Figure 2.19). As expected, the exciton component is largest under resonant illumination ($\lambda = 609.51$nm), and is reduced on either side of resonance. Conversely, the "metallic" signal component remains identical (signal height of ~3mV) throughout the various excitation wavelengths in the vicinity of the 1S line as anticipated. This electrical signal creation mechanism does not vary for a small wavelength scale such as $\Delta\lambda = 0.1nm$. Clearly, the "metallic" signal becomes insignificant compared to the excitonic signal component under resonant condition. Weaker exciton signal components are observed away from resonance due to the laser bandwidth as explained previously. In other words, if the results shown in Figure 2.19 were obtained under ideal experimental conditions (with the use of a perfectly monochromatic laser), an exciton signal would appear for a laser pulse tuned at resonance (within the true 1S linewidth at T=2K), while traces taken away from resonance would only contain the relatively weak "metallic" signal component. In acquiring the measurements shown in Figure 2.19, the oscilloscope's scale was set to maximize the resolution of weak signals occurring off resonance, which resulted in several time-resolved signals ($\lambda = 609.51$nm and $\lambda = 609.52$nm) to be squared off at the peak. This does not pose a particular problem in this instance, since the signal's shape was of interest rather than the value of the signal's peak.

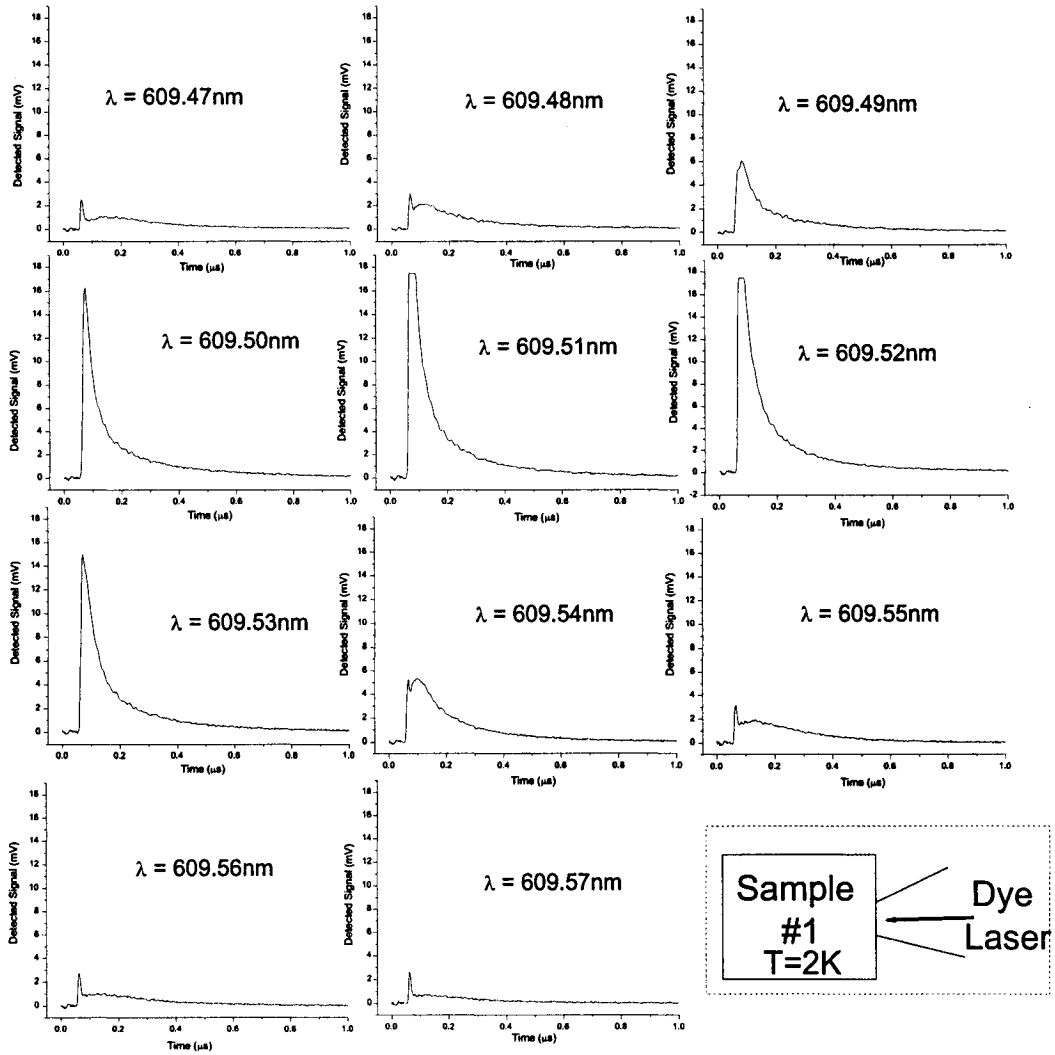

Figure 2.19: Time-resolved front signals resulting from pulsed dye laser illumination at various wavelengths in the vicinity of the 1S line. The laser pulse is incident to the back side of the electrodes.

2.5.3 Time-Resolved Signals Observed in Actual Experimental Excitation Geometries

All time-resolved front signals presented thus far have been signals arising from laser beam illumination directly on the exposed surface of the exciton detector, a circumstance not usually occurring during BEC experiments where the electrodes are covered by a protective light cap. Having access to signals measured from direct electrode illumination introduces the capability of comparing these signals with their counterparts observed during BEC experiments. Such signal comparison can help filter-out effects related to the excitation geometry, such as light scattering.

Time-resolved signals observed during actual BEC experiments are now presented. In Figure 2.20, dye laser front signals corresponding to three different excitation geometries are shown, two of which are from geometries used during BEC experiments (along the main and secondary axis of the sample); for comparison a third signal corresponding to an excitation incident on the exposed surface of the electrodes (taken from Figure 2.18) is shown as well. Surprisingly, all signals demonstrate a similar time dependence regardless of the excitation geometry. Such a result suggests that detected excitons are in much closer proximity to the exciton detector rather than having to migrate from relatively large distances such as previously estimated [19]. As mentioned above, the majority of the detected are those created within ~$110\mu m$ of the electrode surface. The signals observed under experimental-like conditions shown in Figure 2.20, were multiplied by a factor to match the signal obtained from the on-electrode illumination. Light absorption and scattering are the attenuation mechanisms responsible for the relatively small signal amplitude measured for pulses launched along both the main and the secondary axis, as opposed to the on-electrode configuration.

A measured signal central to the research work presented in this thesis is now introduced. This time-resolved signal is produced when an Nd:YAG laser pulse ($\lambda = 532$nm) is used to illuminate (along the main axis) the Cu_2O crystal face opposed to the exciton detector. Upon reaching the crystal surface, the laser light creates an expanding exciton cloud within an absorption length of the surface (~3μm) [12]. The exciton packet then travels across the sample toward the electrodes, where it is thereafter detected. From Figure 2.21, the packet's transit time across a 2.44mm thick crystal is ~600ns, resulting in an average speed of approximately 4000m/s, which is below the speed of sound in Cu_2O (4500m/s) [14].

In fact, it has been determined in the past [14] that the packet's propagation speed is

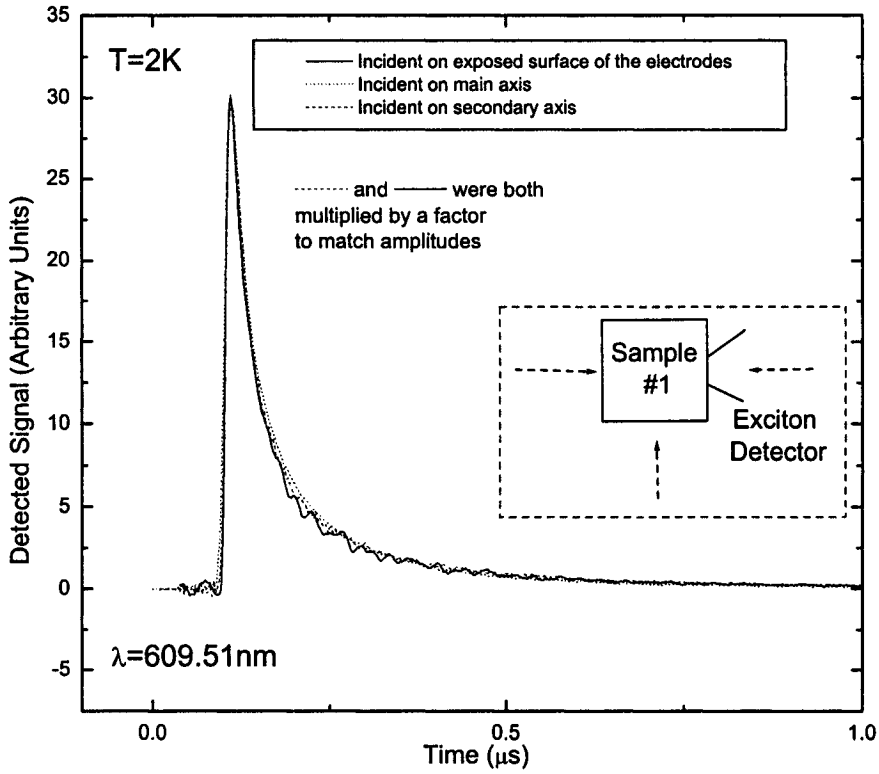

Figure 2.20: Dye laser front signal resulting from a resonant pulsed excitation (λ = 609.51nm). The signals result from three different laser excitation geometries, and are normalized to show the same amplitude.

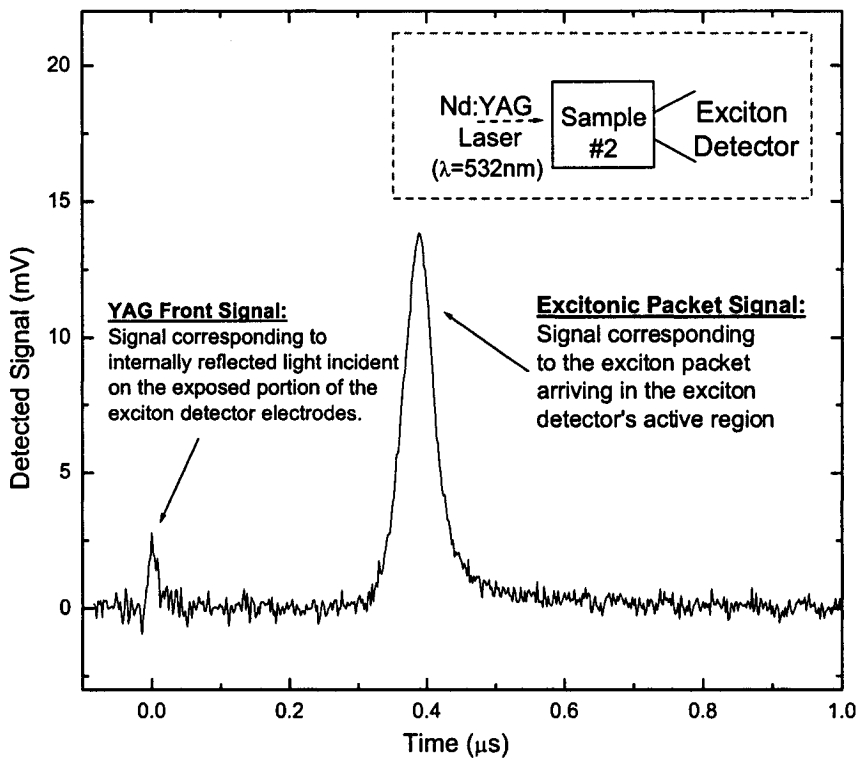

Figure 2.21: Time-resolved signals generated by a pulsed Nd:YAG laser illumination (λ = 532nm) along the sample's main axis. An excitonic packet is detected at the opposing crystal face, where the exciton detector lies.

dependent on its initial exciton density, which can be varied by the illumination intensity and/or the lattice temperature. The additional, smaller signal seen in Figure 2.21 is of much less significance and is caused by a portion of the Nd:YAG pulse being leaked towards the the exposed surface of the electrodes through multiple internal reflections inside the sample holder. We labelled this time-resolved signal earlier (Figure 2.16 and Figure 2.17) as the Nd:YAG front signal. Ironically, the Nd:YAG front signal generated by unwanted light at the electrode's surface, is actually helpful in giving a time-zero reference point at which the laser pulse comes in contact with the Cu_2O sample. The convenience of such a reference point will become evident in later sections when the time-delay of multiple beam excitations will be discussed.

2.6 Linearity and Efficiency of the Exciton Detector

The linearity of the exciton detector has been verified in another work [15] by illuminating the side of the sample with the contacts. However, previously reported results of sublinear behavior of the exciton packet's integrated signals with intensity [14] triggered some criticism about our detector's linearity, leaving doubts on the validity of the signal detected by non-optical means. Criticism [41] has recently been put forth that the detector linearity reported in [15] cannot be justified under excitation geometries different from those used during BEC experiments; it was also mentioned that in a geometry such as the on-electrode illumination, the electron-hole pairs could only be created in the narrow circular slit between the Au and Cu electrodes, and that holes created in this geometry would have a shorter distance to travel in comparison to usual experimental conditions. Although some good points were raised, we remain assured that our detector is in fact linear and that the sublinear behavior of the integrated packet signals was not the result of a saturated detector, but rather due to the nonlinearity of the phenomenon itself. In this section, the linearity and the efficiency of the exciton detector are determined for an excitation geometry similar to the conditions used during BEC experiments, as opposed to the on-electrode configuration.

The temporal shape of the signal (at $\lambda = 609.51\text{nm}$) resulting from dye laser excitation along the main axis is shown in Figure 2.22.

Time-resolved signals are taken at various intensities (actually used in BEC experiments) covering nearly two orders of magnitude. The temporal shape (explained in section 2.5.3) remains the same regardless of the intensity. The peak and integrated signals of Figure 2.22, were plotted as a function of illumination intensity in Figure 2.23.

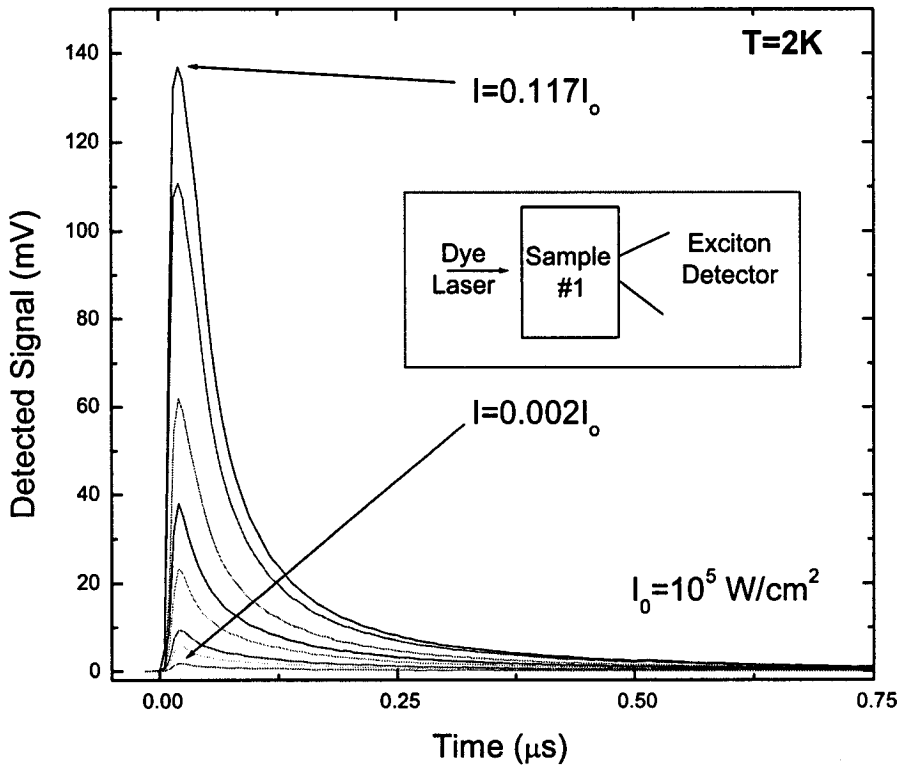

Figure 2.22: Time-resolved dye laser front signals for various intensities. The resonant ($\lambda = 609.51$nm) laser pulse is incident along the sample's main axis.

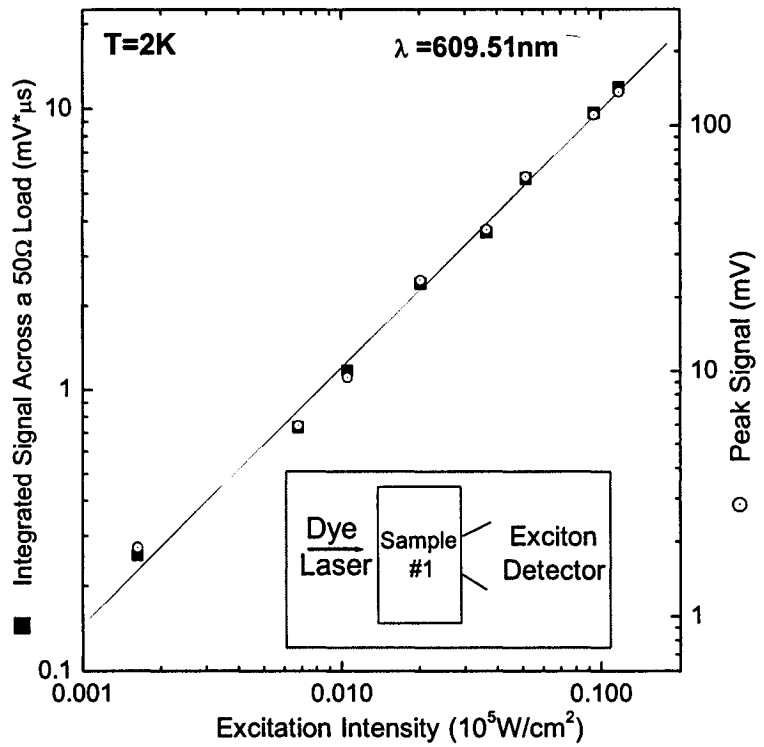

Figure 2.23: Peak and integrated signals of traces shown in Figure 2.22, versus intensity.

The results shown in Figure 2.23 clearly display the linearity of the detector for both the peak and the time-integrated voltaic signals. The maximum signals are in the same range (1-100mV) as observed during experiments reported in [14, 22, 44]. As a consequence, irrespective of the precise mechanism leading to the voltaic effect, the detector yields a signal proportional to the injected orthoexciton density.

It is possible to deduce from the integrated intensity graph an approximate value for the detector efficiency which is defined as:

$$\eta = \frac{Number\ of\ dissociated\ excitons}{Number\ of\ excitons\ created} \tag{2.5}$$

Since the graph is linear, any point in Figure 2.23 will yield the same value. Let us choose the excitation at $0.1I_0$ ($10^4 W/cm^2$) and the integrated response across the 50Ω input of the digital oscilloscope.

$$\int idt = \frac{1}{50\Omega}\int Photovoltage \cdot dt = \frac{10mV \cdot \mu s}{50\Omega} = 2 \times 10^{-10}\ C \tag{2.6}$$

This corresponds to:

$$\frac{2 \times 10^{-10}\ C}{3.2 \times 10^{-19}\ C/exciton} = 6 \times 10^{8}\ \ field - dissociated\ \ excitons \tag{2.7}$$

The number of excitons injected at $0.1I_0$, $10^4 W/cm^2$ during the laser pulse (10^{-8}s) across the 2mm front aperture diameter, assuming 50% reflection losses and further 50% loss due to incomplete absorption, and assuming that all particles reach the detector.

$$\frac{10^4\ \frac{J}{s \cdot cm^2} \cdot 10^{-8} s \cdot (\pi \times 10^{-2})\ cm^2 \cdot 0.5 \cdot 0.5}{3.2 \times 10^{-19}\ \frac{J}{exciton}} = 2.5 \times 10^{12}\ \ excitons \tag{2.8}$$

Thus

$$\eta \approx \frac{6 \times 10^{8}}{2.5 \times 10^{12}} = 2.4 \times 10^{-4} \tag{2.9}$$

We believe this small detection efficiency is mostly due to the magnitude of the built-in field at the interface, which is insufficient to ionize all excitons reaching the back surface [35]. It should be noted in this respect that efficiency values vary somewhat from sample to sample, and for a given sample from one set of electrode deposition to another.

Chapter 3

Results

This chapter involves the presentation and analysis of experimental results. In addition to the basic time-resolved signals explained in section 2.5.3, signals demonstrating two important BEC-related phenomena are first presented in this chapter: 1) condensate amplification resulting from a resonant probing pulse (Figure 3.1); 2) additional attenuation (NDA) experienced by the probing beam in the presence of an exciton condensate (Figure 3.2). Afterwards, results depicting the formation of a secondary packet under various conditions are introduced in section 3.1.3.

In this chapter's next major section (3.2), the wavelength dependence of all the three packet-induced phenomena (condensate amplification, NDA, and onset of a secondary packet) are illustrated via highly-detailed continuous spectra (Sections 3.2.4, 3.2.5, and 3.2.6). Detailed spectra also provided help in: showing a clear relationship between the transmission spectrum and the PV spectrum (Figure 3.12 and 3.17); characterizing the 1S line's temperature evolution (section 3.2.3), observing never-seen-before features of the 1S line, and demonstrating its impact on some condensate-induced phenomena (Figure 3.17 and 3.19).

Most importantly, longitudinal and lateral dependent measurements of NDA (Figures 3.22 and 3.26) with respect to the packet were used to construct a three-dimensional representation (Figures 3.23,and 3.24) of the travelling exciton packet in Cu_2O.

Unless indicated otherwise, all results presented in this section were obtained during experiments performed at T=2K. For the remainder of this thesis, laser intensities will often be expressed in units of I_0, where $I_0 = 10^5 W/cm^2$. In addition, please note that different dimensions of the main axis for the two utilized samples (1.94mm for Sample#1 and 2.44mm for Sample#2) yield different condensate transit times. Therefore, different time delays need to be used for each sample in order to properly synchronize the probe

beam with the travelling condensate (half-transit time: $\delta t \approx 200ns$ for Sample#1 and $\delta t \approx 300ns$ for Sample#2).

3.1 Time-Resolved Signals Related to Bose-Einstein Condensation

3.1.1 Condensate Amplification

A key phenomenon, crucial to the development of this thesis, occurs when a secondary pulse tuned at the 1S orthoexciton energy intercepts the exciton condensate travelling inside the sample. The result is a significant amplification of the excitonic condensate. In the orthogonal excitation geometry, the amplification process is most spectacular when the secondary illumination pulse is specifically timed to intercept the middle portion of the travelling exciton condensate. Amplification of the exciton packet was attributed [16, 19] to the secondary excitation's ability to stimulate the nearly-condensed excitons surrounding the condensate in joining the coherent entity.

In Figure 3.1a, the resulting signals from two distinct excitations are shown. One signal corresponds to a Nd:YAG laser illumination along the main axis, where a similar signal was displayed and explained in Figure 2.21. The other signal shown in Figure 3.1a, corresponds to a time-delayed ($\delta t = 170ns$) resonant dye laser excitation along the sample's secondary axis. An equivalent signal having a different time-delay was featured in Figure 2.18. Figure 3.1b depicts the signal resulting from the orthogonal excitation by both (Nd:YAG laser and Dye laser) radiation sources. An amplification factor of ~1.7 is observed, where the amplification factor is defined as the ratio between the amplified and unamplified condensate's peak signal. The secondary excitation's time-delay of $\delta t = 170ns$ corresponds to a lateral pulse arriving slightly ahead of the exciton packet (the packet and the resonant pulse are not exactly synchronized). This situation does not represent an optimal condition for the amplification process and is the reason behind such low amplification factor. Nonetheless, the amplification factor does not correspond to the algebraic sum of the packet and front signal. A proper explanation of the amplification process was attempted in [16, 19], but will be revisited in further sections of this thesis in order to improve our understanding of the phenomenon.

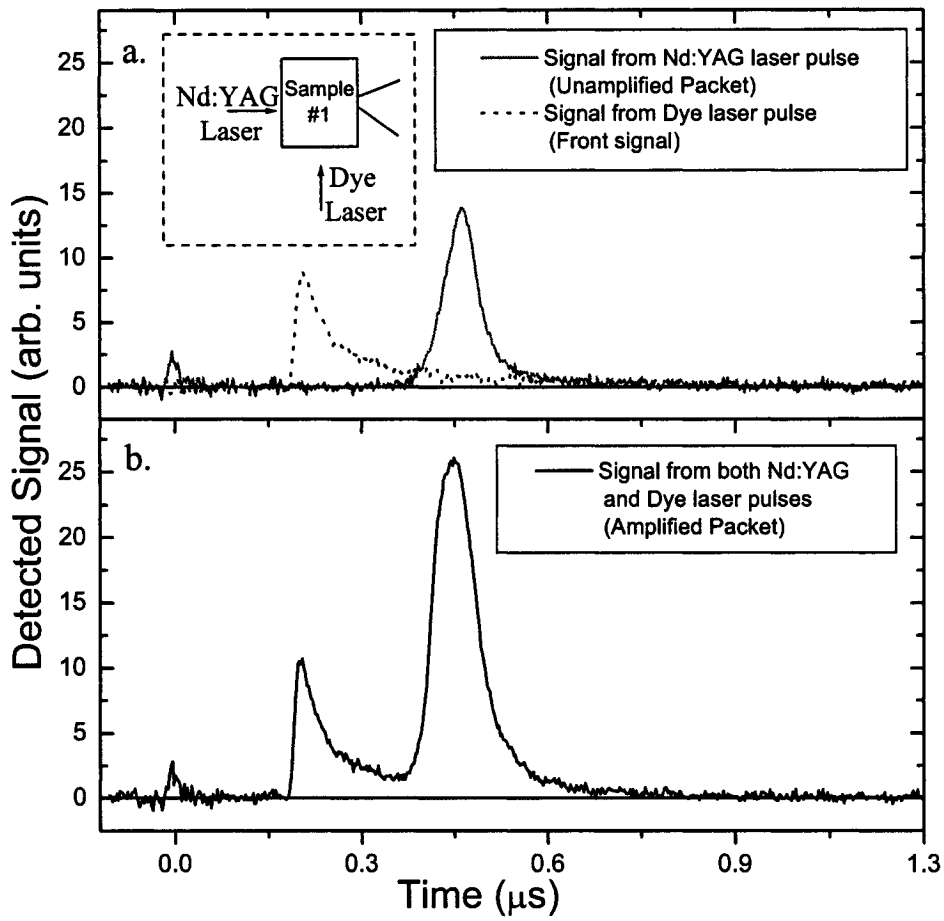

Figure 3.1: Time-resolved signals resulting from excitation in the orthogonal geometry. a. A Nd:YAG laser pulse is incident on the sample's main axis. In a separate measurement, a time-delayed ($\delta t = 170ns$) dye laser pulse tuned at $\lambda = 609.51$nm is incident on the sample's secondary axis. b. The signal resulting from the orthogonal excitation of both laser pulses described above.

3.1.2 Normalized Differential Attenuation (NDA)

Earlier during the signal analysis (Figure 2.14), the transmission signal was seen to be the consequence of a laser illumination along the sample's secondary axis. The attenuation experienced by light travelling through the sample is due to scattering losses and absorption processes governed by the wavelength dependent absorption coefficient ($\alpha \cong 3.5cm^{-1}$) at $\lambda = 609.51$nm. Transmitted light is collected by an optical fiber in contact with the sample, which is coupled to an external photodetector. In experimental conditions similar (orthogonal excitation) to those used to obtain the condensate amplification in Figure 3.1, the time-resolved transmission signal was measured in the presence and in the absence of the excitonic condensate. As depicted in Figure 3.2, the signal measured in the presence of the travelling condensate experienced considerable additional attenuation. Such additional attenuation must evidently be due to a packet induced phenomenon. This phenomenon was explained in [43] to result from either a resonant interaction with the exciton packet and the probing beam, or caused by a crystal distortion induced by the passage of the packet introducing a transient increase in the absorption coefficient.

The measurement of such additional attenuation is termed normalized differential attenuation (NDA). It is defined as the ratio between the difference in signals (signal in the absence and in the presence of the exciton packet) and the signal in the absence of the packet. More precisely NDA= $(I - I_p)/I$, where the transmission signal in the absence of a packet is denoted by "I", while "I_p" corresponds to the signal detected in the presence of the packet. As shown in Figure 3.2, the lateral laser pulse is additionally attenuated by a factor of ~2.22 in the presence of the excitonic packet. The seemingly large signal to noise ratio was a result of an electrical interference in the wire that was induced by the laser's pockels cell, which generated periodic noise. This noise remained essentially the same for each measurements as seen from the two traces (solid and dotted lines) in Figure 3.2, and could therefore be easily eliminated by subtracting the desired signal from the background signal.

Because of its dimensionless nature, the NDA measurement is invariant to various experimental parameters, such as the probe beam intensity. The latter was successfully verified in [19]. The measurement of NDA proves to be a very useful tool to effectively probe the travelling condensate. In later discussions, condensate amplification and NDA measurements are found to be complementary to one another. Results of condensate amplification and NDA measurements from various longitudinal parts of the packet (time

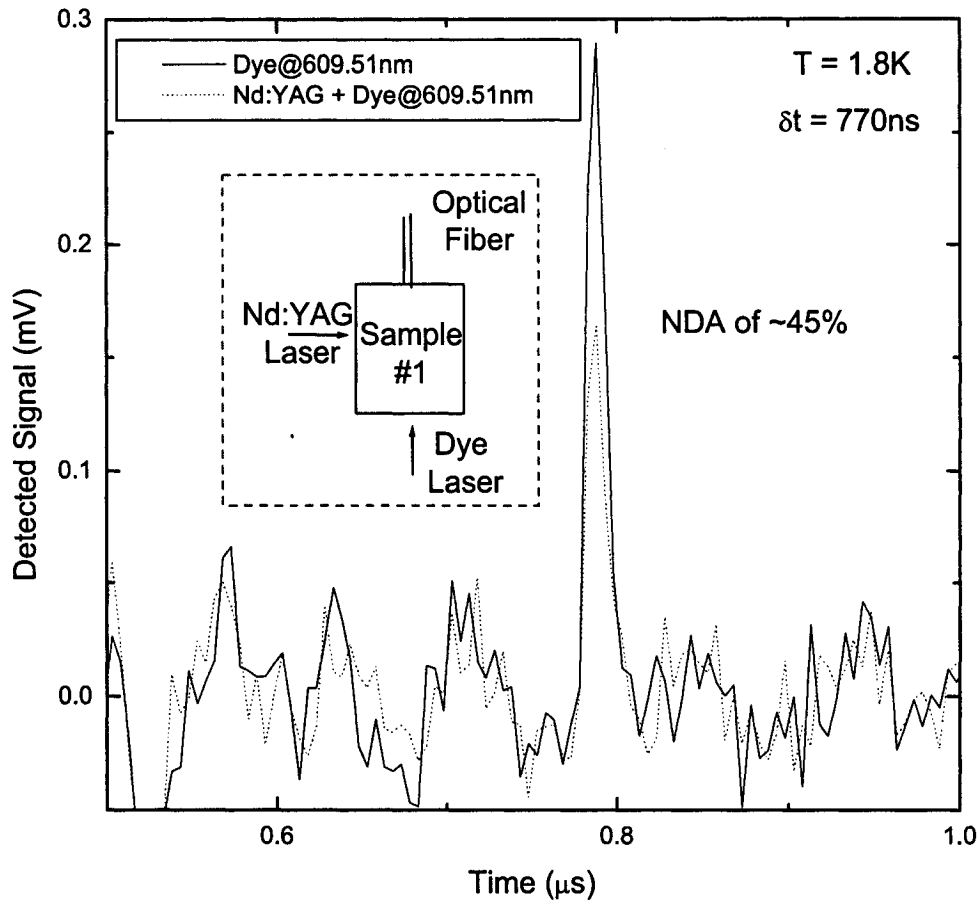

Figure 3.2: The time-resolved transmission signal resulting from a resonant (λ = 609.51nm) dye laser pulse excitation along the sample's secondary axis. Light transmitted through sample was collected with an optical fiber and thereafter detected by an external photodetector. The transmission signals were measured in the presence and absence of the exciton condensate, where an NDA of ~45% was observed. The dye laser time-delay of $\delta t = 770ns$, corresponds to the resonant pulse intercepting the tail end of the exciton packet.

delays) will be presented in section 3.3. The packet's lateral distribution of excitons can also be estimated by observing the NDA for several probe-beam vertical positions for a particular region of the exciton condensate (fixed time delay). For the remainder of this thesis, this detection method will be the main tool used to optically probe excitonic condensates.

3.1.3 Secondary Packet Formation

A secondary exciton packet is observed when the the resonant ($\lambda = 609.51$nm) probe beam is configured to stimulate the tail exciton condensate. This observation was first reported in [44], under the orthogonal excitation geometry. In order to determine the proper formation mechanism of the secondary packet, new experiments were performed under various experimental conditions: excitation geometries, pump-probe beam time-delays, pump and/or probe beam intensities. The wavelength dependence of the secondary packet formation will also be presented in this thesis in section 3.2.5.

In the orthogonal excitation geometry, the emergence of a secondary exciton packet occurs at relatively large time delays ($\delta t >$ half-transit time) i.e. the probe beam is incident on the crystal after the passage of the exciton condensate. In Figure 3.3, four graphs depicting secondary packets formed at different probe-pump beam delays are presented. The top-left graph was taken at a time delay of $\delta t = 300ns$ (half-transit), representing complete synchronization between the probe beam and the exciton condensate (i. e. the lateral beam probes the middle portion of the condensate). A significant amplification of the condensate is observed but no secondary packet is formed since the probe beam stimulates the core of the condensate and not its tail portion. In the top-right figure where the lateral beam arrives in the center of the crystal after the passage of the condensate ($\delta t = 770ns$), an emergence of a secondary packet is seen (pointed out by arrow). At this time delay, the lateral beam probes the tail component of the condensate and not the condensate's core (no amplification). The dye laser front signal overlaps part of the secondary packet, obscuring a complete view of the secondary packet. At delays of $\delta t = 1200ns$ (bottom-left figure) and $\delta t = 1500ns$ (bottom-right figure), a secondary packet is still observed even though the main condensate has long ceased to exist. This therefore corresponds to the stimulation of quasi-stationary (cold) excitons left in the sample by the travelling exciton condensate. During experiments, the formation of secondary packets was observed at time delays as long as $\delta t = 2000ns$. This observation reflects the presence of cold excitons remaining in the sample due to

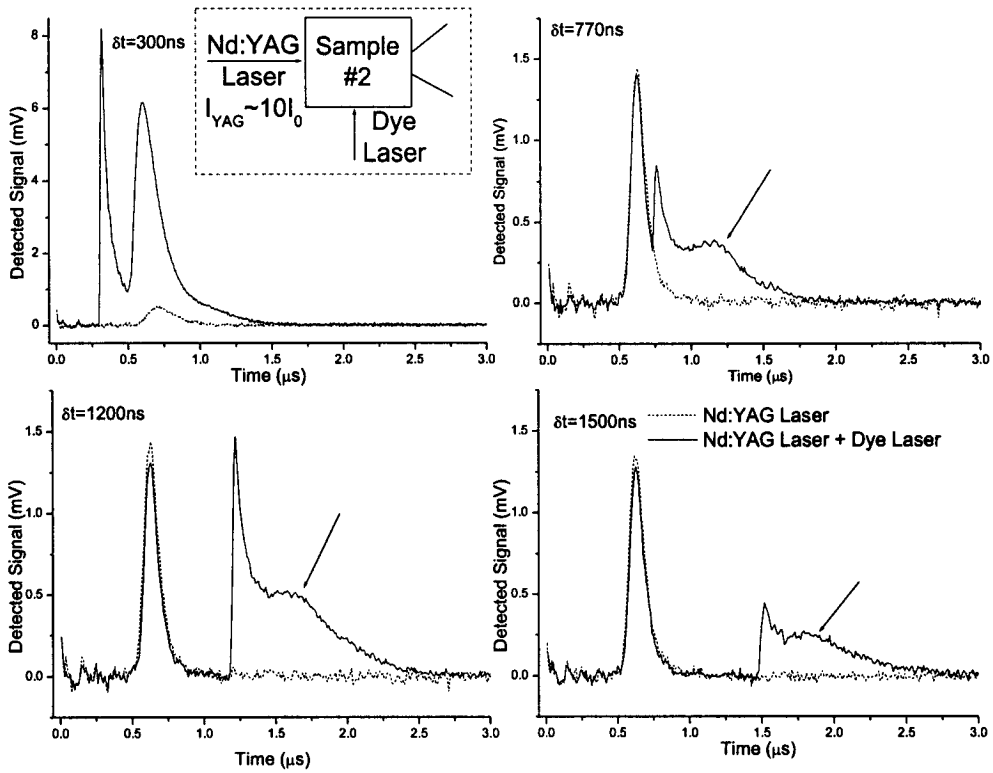

Figure 3.3: Onset of a secondary packet at time-delays "δt" larger than the condensate's half-transit time ($\delta t = 300ns$). Excitations were performed in the orthogonal geometry, with a dye laser tuned at resonance ($\lambda = 609.51$nm). The secondary packets are pointed out by arrows. The top-left figure is presented on a different scale to better show the condensate amplification.

the long exciton lifetime (up to $10\mu s$ [42]). In principle, a secondary packet would be stimulated for delays equal to or shorter than the paraexciton lifetime given a sufficient density (see Figure 3.9). The relationship between secondary packet amplitude and the dye laser front signal amplitude seen in Figure 3.3, is reminiscent to the amplification of the exciton condensate for various dye laser intensities reported in [43]. The changes in the pulse intensity (front signal) throughout Figure 3.3 are caused by the use of time delaying optical fibers of various lengths, resulting in various fiber losses. Larger delays usually yield a larger attenuation because of the extended optical path taken by the light pulse through the fiber. Since the condensate no longer exists in the sample (dissociated by the exciton detector) by the time a resonant pulse is incident on the crystal, when delayed at times larger than 700ns, no amplification process can take place as observed in Figure 3.3.

In Figure 3.4, a secondary packet is formed in the collinear geometry as opposed to the orthogonal geometry seen in Figure 3.3. Figure 3.4 depicts the formation of secondary packets for a time delay at $\delta t = 770ns$, and various dye laser illumination wavelengths. A closer view of these secondary packets is displayed in Figure 3.5. The largest secondary packet amplitude is formed by a dye laser pulse tuned at $\lambda = 609.51$nm, which corresponds to resonance. Under resonant conditions, the largest amount of excitons are created at a given intensity, leaving more excitons to interact with the distribution of cold excitons in the sample left behind by the packet. In Figure 3.6, secondary packets are shown to form at a delay of 1200ns. A closer view of the secondary packet formation is presented in Figure 3.7, where a dye laser tuned at resonant once again delivers the largest secondary packet formation amplitude. There are no major differences in secondary packet formation at $\delta t = 770ns$ (Figure 3.5) and $\delta t = 1200ns$ (Figure 3.7), they are essentially equivalent in terms of secondary packet creation. In both cases, relatively cold excitons left behind by the exciton condensate, are stimulated to form a secondary packet. In these cases, the condensate has long been detected (no longer in the crystal) and is the reason for not being amplified.

However, unlike the case of orthogonal excitation, in the collinear excitation geometry a secondary packet is observed at shorter time delays as seen in Figure 3.8 ($\delta t = 300ns$). This occurs since the dye laser pulse must necessarily cross the tail portion of the condensate in this excitation configuration, a secondary packet is therefore observed regardless of the time delay.

Moreover, a noticeable condensate amplification is visible in Figure 3.8, making the secondary packet difficult to discern at $\lambda = 609.51$nm. In this geometry, amplification

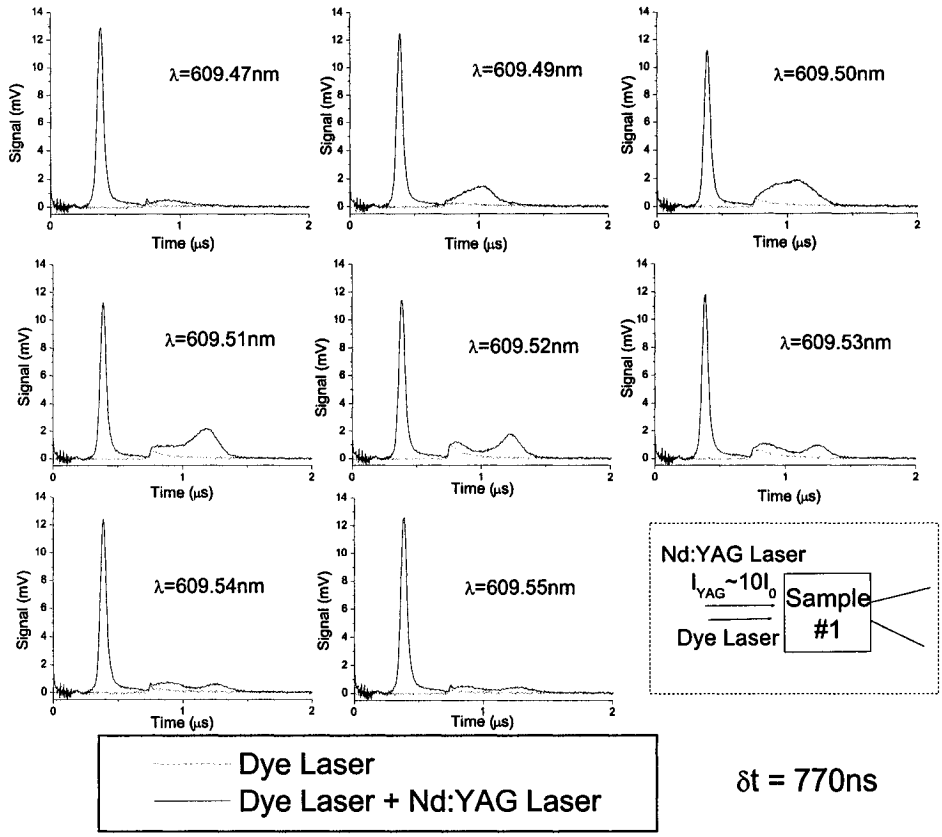

Figure 3.4: Secondary packet created in the collinear excitation geometry with various dye laser wavelengths. The dye laser pulse is delayed by 770ns with respect to the Nd:YAG laser pulse.

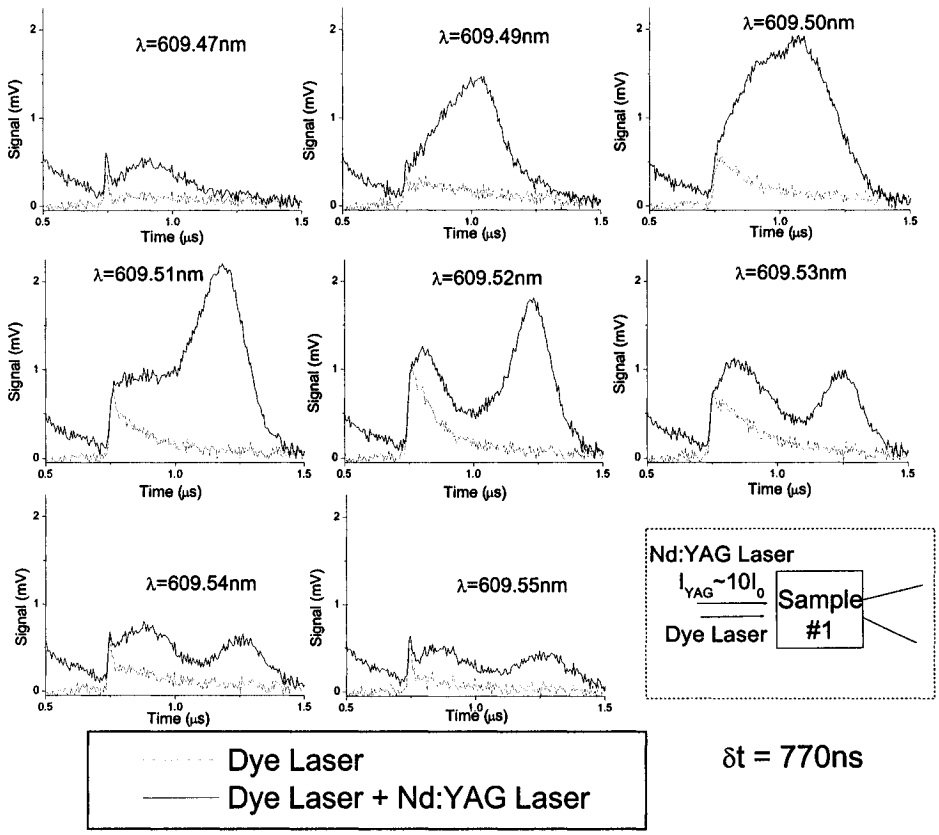

Figure 3.5: Zoom-in view of the secondary packet signals presented in Figure 3.4.

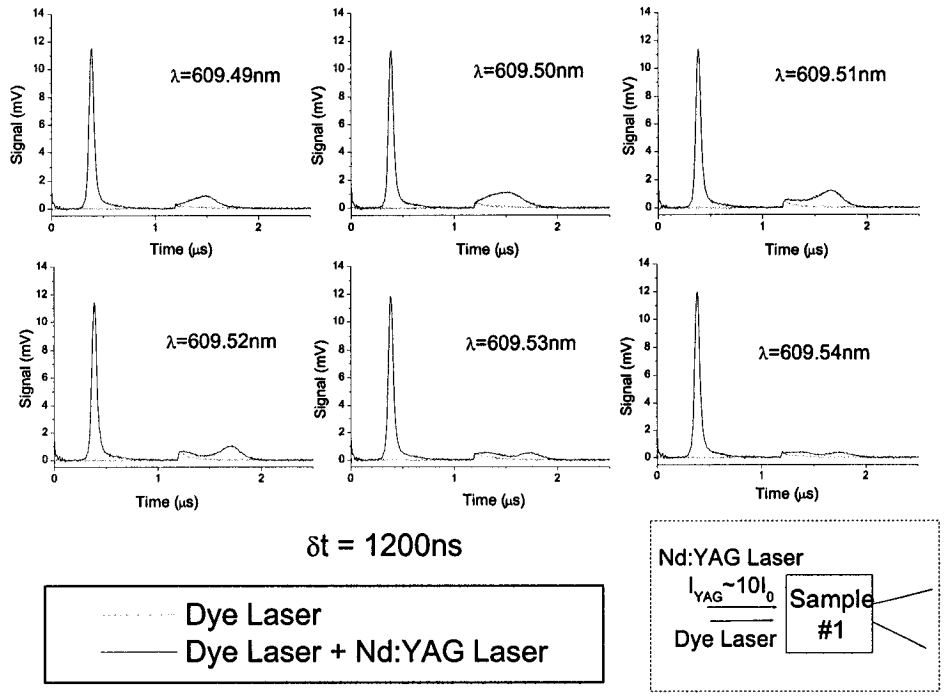

Figure 3.6: Secondary packet created in the collinear excitation geometry with various dye laser wavelengths. The dye laser pulse is delayed by 1200ns with respect to the Nd:YAG laser pulse.

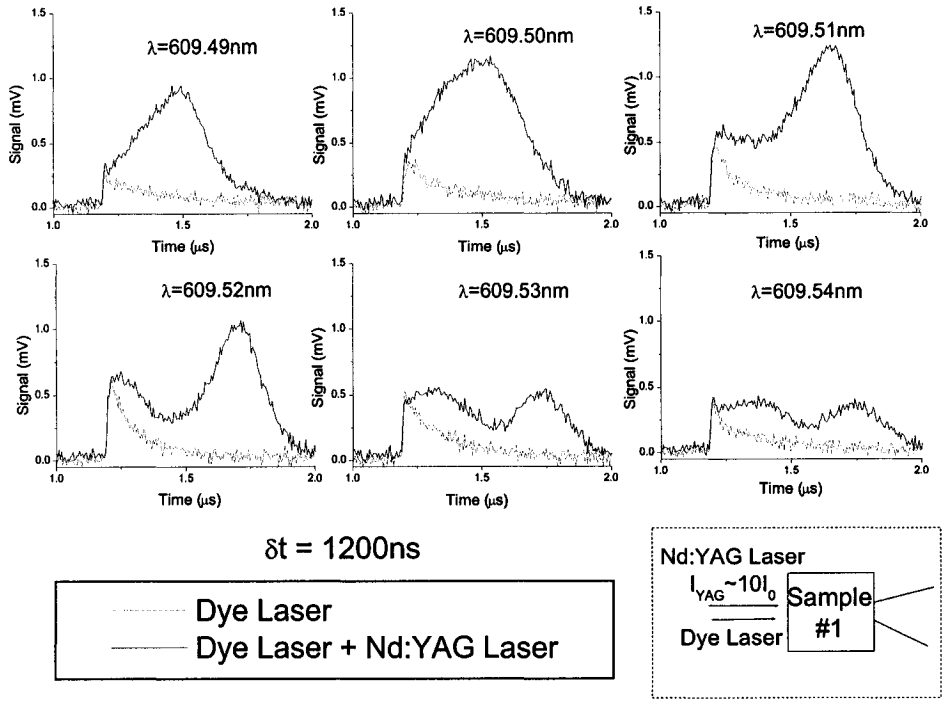

Figure 3.7: Zoom-in view of the secondary packet signals presented in Figure 3.6.

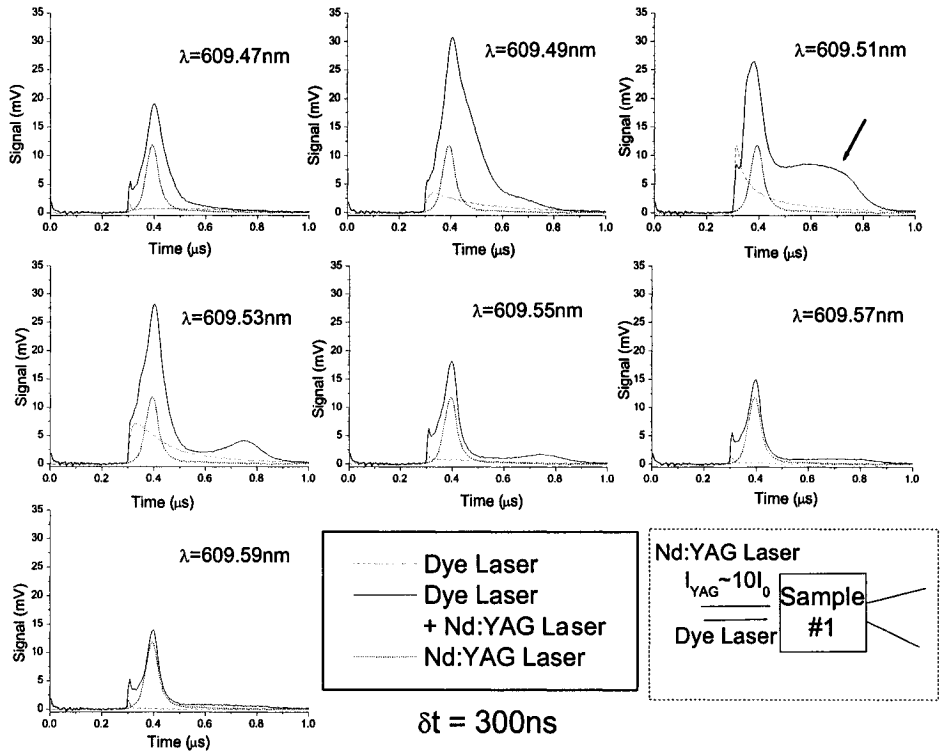

Figure 3.8: Secondary packet created in the collinear excitation geometry with various dye laser wavelengths. The dye laser pulse is delayed by 300ns with respect to the Nd:YAG laser pulse.

was observed at $\delta t = 0$ suggesting the packet collects excitons along its way towards the exciton detector, contributing to the amplification process. In fact, condensate amplification under collinear excitation will occur as long as the condensate is present in the sample ($\delta t = 0$ to one transit time).

Assuming similar experimental conditions (same laser intensities and $\delta t = 300ns$) but with different excitation geometries, the orthogonal excitation geometry will yield a larger amplification factor as opposed to the collinear geometry, since for the latter one the probe beam must first interact with the tail portion before participating in the amplification process of the condensate (core). Only at large delays ($\delta t >$ half-transit time) do both excitation geometries (collinear and orthogonal) become somewhat equivalent.

The formation of a secondary packet was found to be extremely sensitive to the Nd:YAG laser pulse intensity responsible for creating the original exciton condensate. In Figure 3.9 the secondary packet is largest when $I_{Nd:YAG} \cong 6.3I_0$. The secondary packet amplitude is noticeably smaller for a Nd:YAG laser intensity of $I_{Nd:YAG} \cong 1.6I_0$, and completely disappears under a laser intensity of $I_{Nd:YAG} \cong 1.0I_0$. The onset of the secondary packet and its disappearance occurs all within an intensity difference of less than an order of magnitude. A Nd:YAG laser pulse having a larger intensity creates more excitons but since the peak amplitude of condensate was reported to saturate [14] (finite size), the rest of the created excitons remain diffusive and surround the condensate. Therefore, the tail portion of the condensate has a higher density of excitons at larger pump pulse intensity, yielding a more pronounced secondary packet formation.

As mentioned earlier, resonant pulse creates the largest exciton density for a given illumination intensity. The secondary packet formed at various wavelengths shown in Figures 3.4 and 3.6 clearly displays this relationship (smaller secondary packet formed at off-resonant illumination $\Rightarrow$ smaller exciton density). Using different wavelengths to form secondary packets is therefore equivalent to varying the laser intensity.

The formation of a secondary packet at two different time delays is shown in Figure 3.10. At first glance, the secondary packets formed at both delays look similar apart from the shift due to different arrival time of the dye laser. A closer look reveals a difference in dye laser front signal amplitude of both cases ($\delta t = 770ns \Rightarrow 0.77mV$ and $\delta t = 1200ns \Rightarrow 0.45mV$). Once again, the weaker front signal at $\delta t = 1200ns$ can be explained by the attenuation related to the additional distance travelled in the optical fiber. As a consequence, the secondary packet at $\delta t = 770ns$ has a larger amplitude (~1mV) than the packet observed at $\delta t = 1200ns$ (~0.5mV). The amplitude

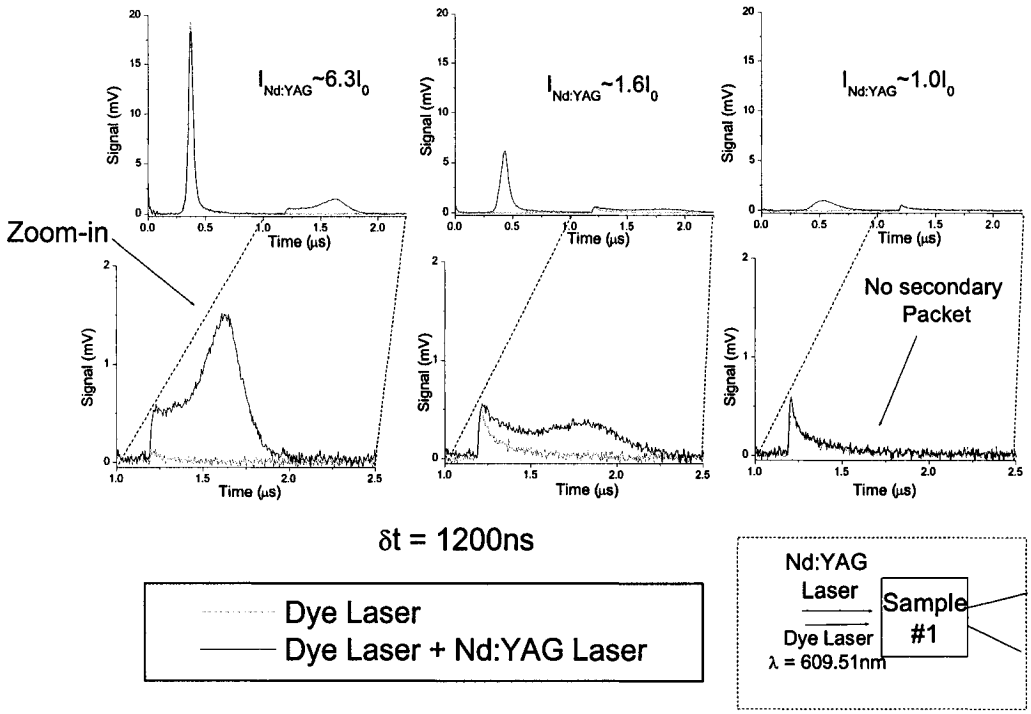

Figure 3.9: Secondary packet created in the collinear excitation geometry with various Nd:YAG laser intensities. The dye laser pulse is delayed by 1200ns with respect to the Nd:YAG laser pulse.

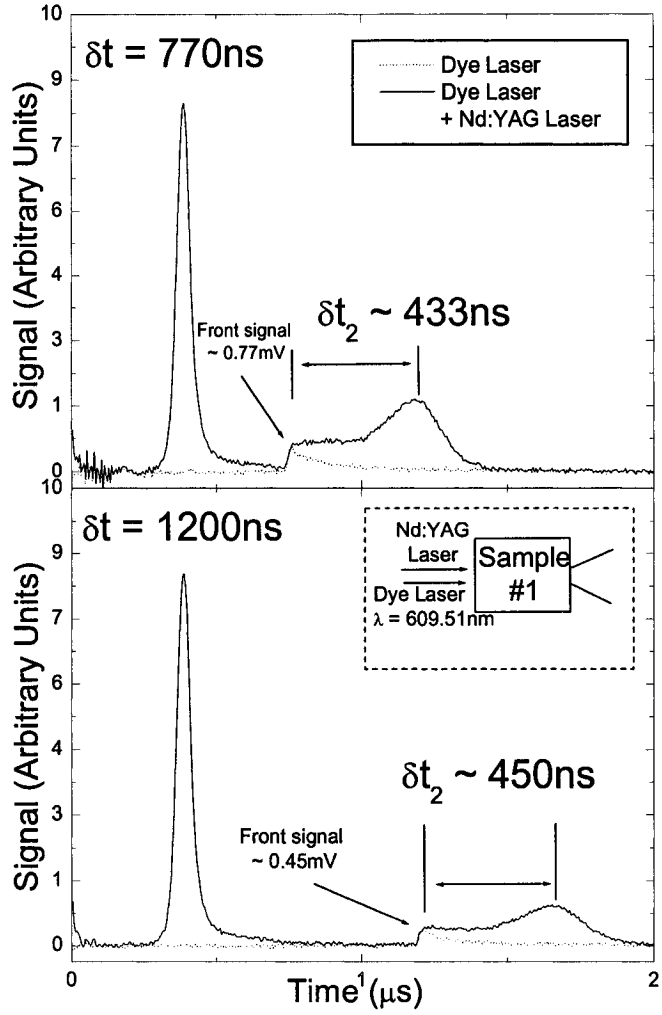

Figure 3.10: Time-resolved signals demonstrating the presence of a secondary packet with various pump-probe beam time-delays.

of the secondary packet is therefore proportional to the front signal amplitude. Moreover, the temporal separation "δt_2" between the dye laser front signal and the center position of the secondary packet, is slightly different from one time delay to the other ($\delta t = 770ns \Rightarrow \delta t_2 \cong 433ns$ and $\delta t = 1200ns \Rightarrow \delta t_2 \cong 450ns$). The larger secondary packet is a little faster, reminiscent to the behavior of the exciton condensate under increasingly intense illumination [14]. In Figure 3.10, both secondary packets are classified as being in the diffusive regime since their average velocities are ~2700m/s corresponding to a velocity slightly above half of the speed of sound in cuprous oxide ($v_s \cong 4500m/s$).

The temporal separation between the dye laser front signal and the center position of the secondary packet seems to remain constant (for a constant incident illumination intensity) regardless of the time-delay used. According to the results presented thus far, there is reason to believe that the condensate's tail contains numerous non-condensed excitons nearing the BEC critical density. An injection of additional exciton could therefore satisfy this critical density, initiating the formation of a secondary exciton packet.

3.2 Continuous Spectra

A pulsed tunable dye laser was used to acquire highly detailed spectra in the proximity of the 1S orthoexciton line in Cu_2O. The spectra were taken in the following way: a digitizing oscilloscope linked to a computer recorded the average signal amplitude for a certain time interval "τ" (in most cases τ=2s equivalent to 20 pulses), while a tunable dye laser continually scanned through a preset range of wavelengths. Due to the type of dye mixture used (see section 2.1.1) during experiments, the dye laser's spectral range of 600-620nm had a power output difference of approximately 40%. However, all significant measurements were taken within 1nm from 610nm where the laser power output is relatively constant.

3.2.1 PV Spectrum between 600-610nm

The spectral region of interest in Cu_2O (T=2K) is situated within the wavelength interval of 600-610nm, where three absorption mechanisms are observed: high energy absorption into the band, phonon-assisted absorption, and n=1 resonant absorption line. A spectrum containing all three mechanisms is presented in Figure 3.11. In this figure, the deposited electrodes (exciton detector) were used as a mean of detection through the exciton mediated photovoltaic (PV) effect.

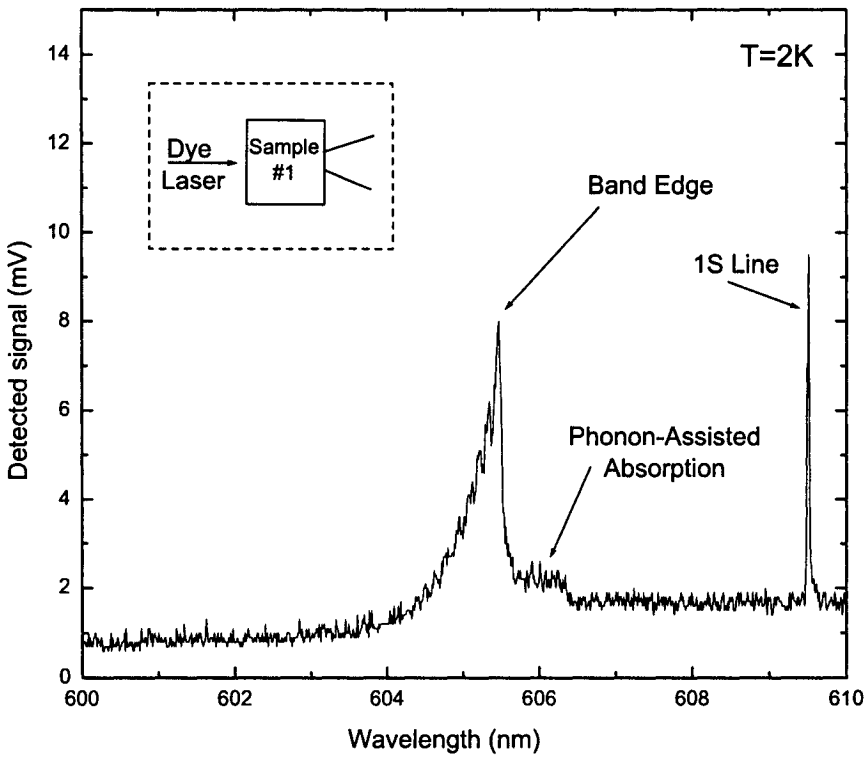

Figure 3.11: Absorption spectrum of Cu_2O depicting three regions of interest: absorption at the band edge, phonon-assisted absorption, and n=1 resonant absorption line.

Beginning with the analysis of Figure 3.11 from the high energy (smaller wavelength) end of the spectrum, a relatively weak signal is detected since most photons are absorbed by the sample before reaching the exciton detector due to the crystal's strong absorption coefficient at these wavelengths. As the incident radiation's wavelength increases (photons lower in energy) the absorption coefficient decreases, consequently permitting more photons to reach the effective region of the exciton detector. Near $\lambda = 604$nm a rapid increase in detected signal is observed resulting from the creation of electron-hole pairs by the increasingly penetrating incident radiation. An abrupt falloff in detected signal occurs at $\lambda = 605.4$nm (band edge), due to the photon's lack of energy to excite electrons. However, the signal falloff does not immediately drop to its original value due to a series of phonon-assisted transitions. The most significant absorption mechanism shown in Figure 3.11 is represented by a sharp peak centered around $\lambda = 609.51$nm (2.034eV), and corresponds to the 1S orthoexciton energy level. Due to a calibration error of the dye laser, the observed position of the 1S excitonic line of 2.034eV is slightly shifted with respect to the accepted value of 2.033eV [20].

This figure was presented in order to give a general idea of the excitonic processes taking place in Cu_2O. In previous work [19], condensate amplification was studied in both the band edge region and the 1S orthoexciton resonance. For the remainder of this thesis however, our study will be limited simply to the 1S line region.

3.2.2 Transmission and PV Spectrum in the Vicinity of the 1S Line

The 1S orthoexciton spectral region ($\lambda \approx 609.51$nm) of Figure 3.11 is of importance in this thesis since resonant secondary excitation intercepting the travelling condensate results in both condensate amplification (section 3.1.1) and packet-induced attenuation of the resonant pulse (section 3.1.2). In later sections the spectrum of the condensate amplification and the packet-induced attenuation will effectively demonstrate that resonant excitation yields the best results for both of these phenomena. In order to further investigate resonant absorption, a highly detailed spectrum of this region was measured.

The PV spectrum in the vicinity of the 1S line (609.45-609.60nm) is represented by a dotted line in Figure 3.12, while the solid line represents the transmission spectrum measured by an external photodetector. Each of the spectra's extremum is centered at resonance ($\lambda = 609.51$nm) and both linewidths are ~0.028nm (~$93\mu eV$), compared to the value of $1\mu eV$ reported in [20]. The resolution of the 1S line is limited by the dye laser

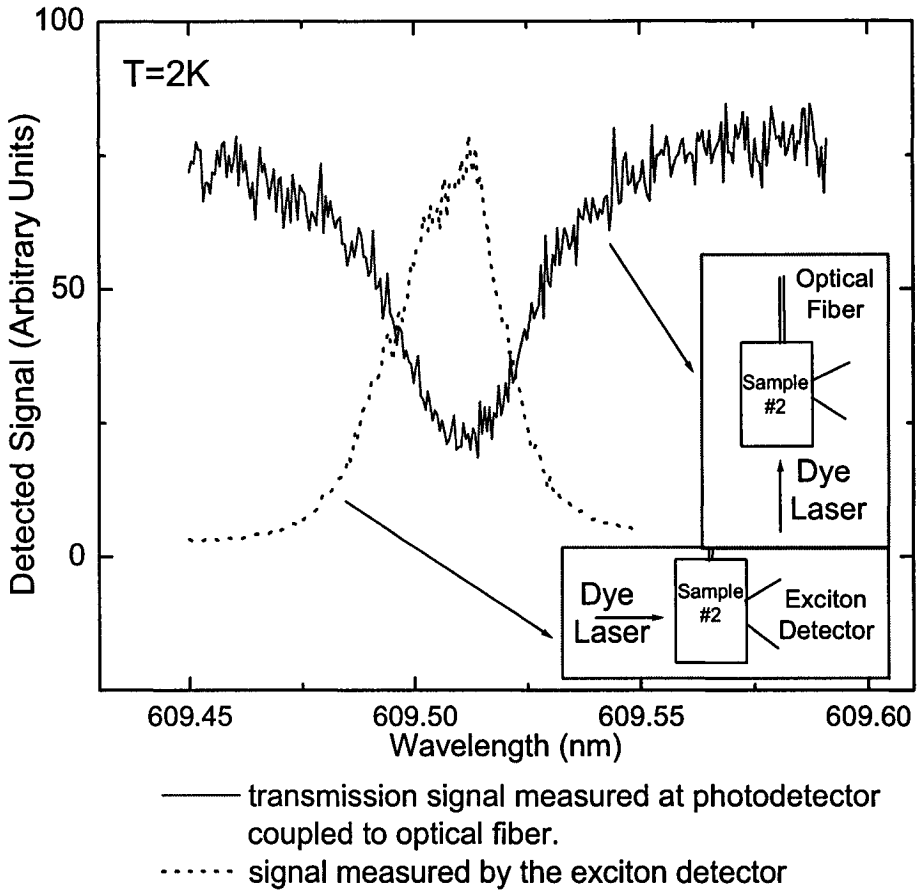

Figure 3.12: Transmission and PV spectra in the vicinity of the n=1 orthoexciton line.

bandwidth of $\Delta\lambda = 0.015nm$ ($50\mu eV$). A comparison of the two curves in Figure 3.12, clearly demonstrates that the PV signal is directly related to the 1S orthoexcitons produced by the light absorption process.

3.2.3 Temperature Evolution of the 1S Line

Using the method described above, transmission spectra of the 1S line were taken at various temperatures between $T = 1.8K$ to $T = 36K$ (Figure 3.13). As expected, the position of the 1S line is shifted towards the lower energies as the lattice temperature increases, while the linewidth increases due to thermal broadening.

According to Figure 3.14, which was extrapolated from Figure 3.13, the thermal broadening varies linearly with temperature, while the n=1 excitonic energy level varies proportionally to the square of the temperature.

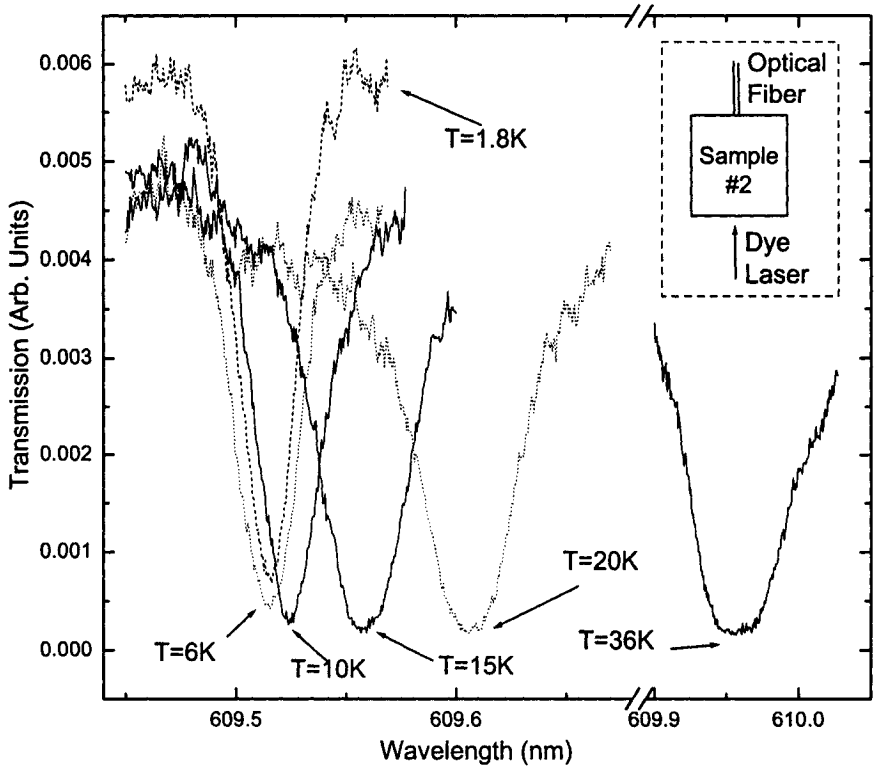

Figure 3.13: Temperature evolution of the 1S line.

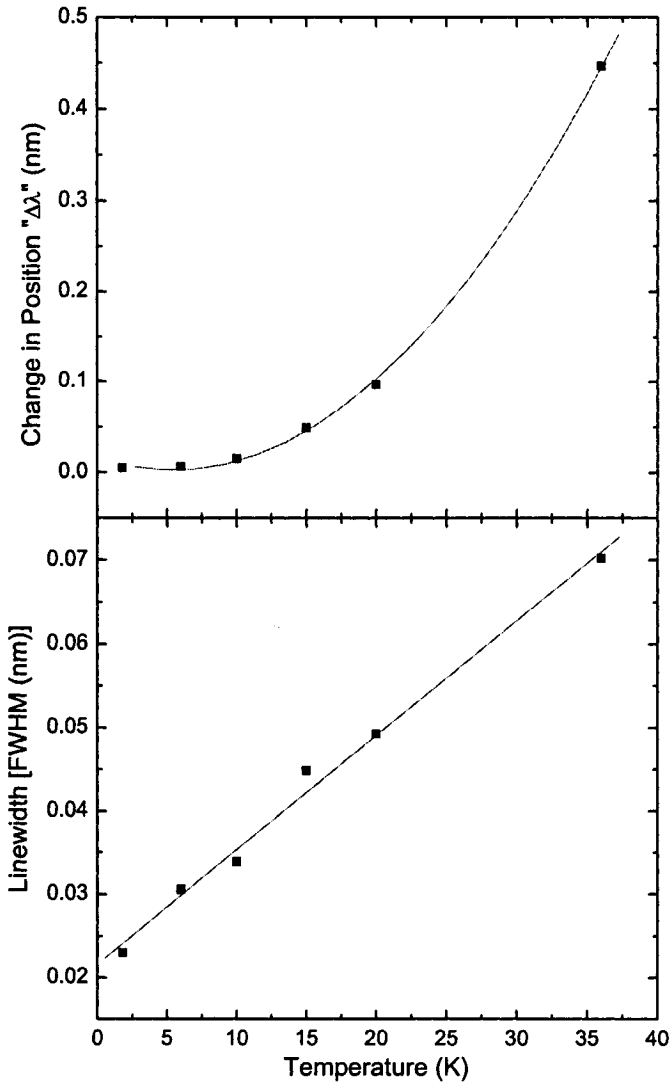

Figure 3.14: Change in position and linewidth of the 1S orthoexciton absorption line for various temperatures. This figure was constructed with the use of Figure 3.13

A rise in sample temperature corresponds to a lattice expansion, where the oscillations of atoms about their lattice equilibrium point increases, resulting in the energy gap to decrease (band edge shift towards the low energies)along with its excitonic energy levels. The increased motion of the exciton due to phonon scattering, broadens the energy levels.

An interesting fact about the thermal broadening observed in Figure 3.14 should be mentioned at this point. If the 1S orthoexciton line had an actual width of $1\mu eV$ ($\Delta\lambda = 0.03 \times 10^{-3}$nm) as reported by Fröhlich in [20], no thermal broadening should be observed with a laser bandwidth fifty times larger ($50\mu eV$ or $\Delta\lambda = 0.015$nm) than the reported linewidth. The true measurement of linewidth can only be done with a laser bandwidth smaller or equal to the width of the line in question. By considering the thermal broadening to be linear with T (as measured), a visible line broadening should only be expected above T=50K (assuming linear broadening), with the current laser bandwidth. But that is not the case since thermal broadening is immediately visible after the first temperature change ($\Delta T \approx 4$K), suggesting the 1S line to be much wider than previously anticipated. In a recent paper [45], a transmission spectrum of Cu_2O taken with a laser having a bandwidth of $10\mu eV$ revealed a linewidth of $80\mu eV$ for the 1S line. Unfortunately, in this publication D. Fröhlich did not make reference to his previous work [20].

3.2.4 Wavelength Dependence of Condensate Amplification

The wavelength dependence of the exciton condensate amplification is shown in Figure 3.15. The measurement was taken under orthogonal excitation with $\delta t = 300ns$. The dye laser was therefore synchronized with the middle of the packet. This figure demonstrates how resonant stimulation ($\lambda = 609.51$nm) of the condensate yields the largest amplification factor (a factor of ~6 in this case), consistent with the model proposed by Benson. According to that model, amplification occurs when excitons that are injected into the condensate by a resonant pulse entice nearly-condensed excitons of the coma component of the packet to fall into the condensate. One again, a variation in wavelength towards resonance can be viewed as a rise in illumination intensity, as resonant excitation delivers the largest exciton density thereby observing the largest amplification factor as expected from this model. Note that a larger amplification factor can be achieved with a relatively weak Nd:YAG laser pulse and an intense dye laser pulse [16].

The spectral width of the condensate amplification's dependance on wavelength (~0.026nm)

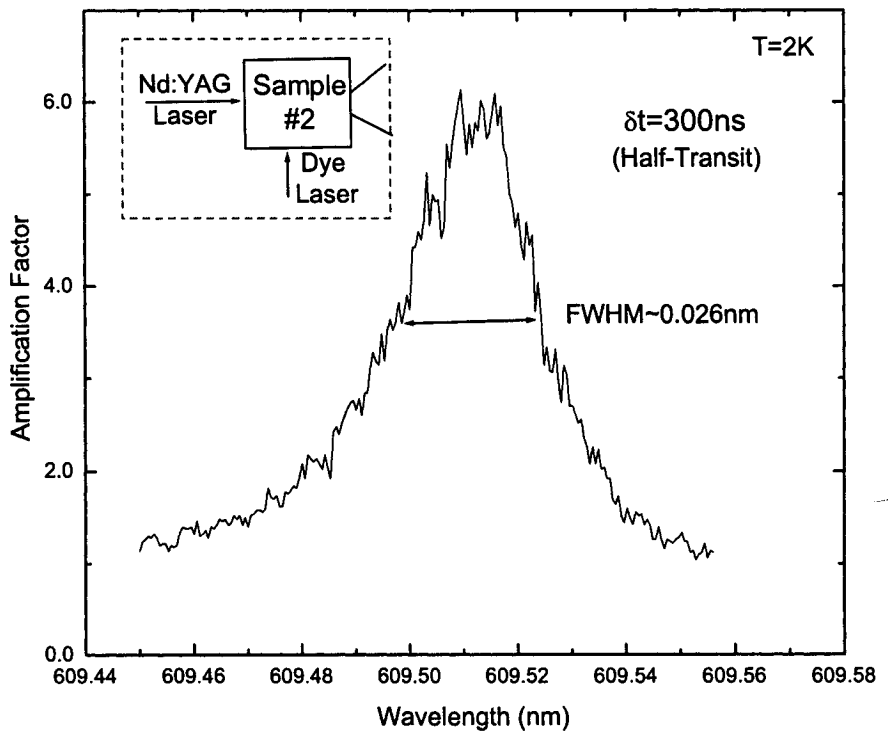

Figure 3.15: Wavelength dependence of the condensate amplification.

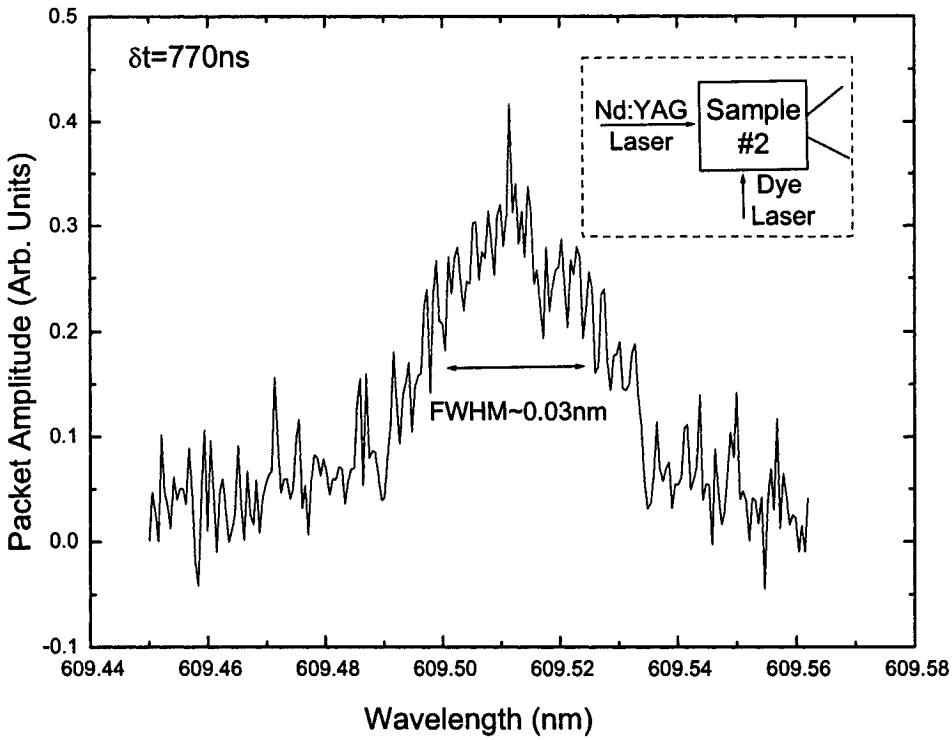

Figure 3.16: Wavelength dependence of the secondary packet formation, for a probe beam time delay of $\delta t = 770ns$ with respect to the Nd:YAG laser pulse.

is comparable to the FWHM of the 1S line spectrum spectra shown in Figure 3.12 (~0.028nm). This suggests that the spectral widths are limited by the laser bandwidth.

The packet-induced attenuation was also found to be maximum for resonant excitation, therefore suggesting that NDA and the amplification process are closely related. Convincing spectra relating both NDA and condensate amplification will be presented in section 3.2.6.

3.2.5 Wavelength Dependence of the Formation of the Secondary Packet

The wavelength dependence on secondary packet formation (Figure 3.16) is shown to be centered at $\lambda = 609.51$nm, consistent with previous results (Figure 3.5, Figure 3.7). This measurement was taken under orthogonal excitation for $\delta t = 770ns$; the tail of the condensate was thus probed by the dye laser pulse.

The wavelength dependence of the secondary packet formation has a FWHM~0.03nm,

similar to the corresponding value for the exciton condensate (FWHM~0.026nm). However, the accuracy of the FWHM value for the wavelength dependence of the secondary packet formation, is limited due to the large signal to noise ratio visible in Figure 3.16.

3.2.6 Spectral Splitting of the 1S Line

In sample #1, the 1S absorption spectrum reveals a splitting when a vertically polarized dye laser illumination is incident along the sample's main or secondary axis. The first observation of the 1S line splitting occurred with an excitation along the secondary axis similarly to the PV spectrum shown in Figure 3.17(solid line). One of the peaks corresponds to resonance (λ = 609.51nm), while the other situated at λ = 609.53nm is of unknown origin for the moment. The total linewidth of ~0.047nm (~157μeV) is almost double that of figure 3.12 where no splitting is observed. This unexpected result led us to believe that an experimental artifact was responsible for the splitting, since no such splitting of this nature was ever reported for Cu_2O. Possibly since the instruments available at the time (1960's), where properties of Cu_2O were heavily studied might not have had enough precision to properly resolve features of the 1S line. An approximate spectrum (with limited set of points) of the 1S line was taken in [43] where no splitting was observed, however more resolution is offered with the use of the current spectrum acquisition technique (with the tunable dye laser). In any event, a search to find an explanation was sought after to determine the cause of the splitting, beginning with tests and followed by experiments.

It was first suggested that the dye laser output spectrum could contain two peaks (splitting) due to the dye mixture. However, this proved to be false when measurements taken with a spectrally (in the region of interest) flat detector did not reveal a splitting, therefore dismissing the dye mixture as the source of the splitting.

An interesting paper was found where a splitting of the 1S line attributed to the Stark effect in the presence of an electric field was reported [46]. A Cu_2O crystal exposed to an electric field magnitude of 47 kV/cm, resulted in a splitting of ~0.04nm, similar to the splitting depicting in Figure 3.17. The localized electric field used to dissociate excitons (section 2.2) in the depletion width near our deposited electrodes had become a prime candidate for the possible source of the occurring splitting. However, a transmission spectrum (dotted line in Figure 3.17) was eventually measured where surprisingly a prominent splitting was observed, thereby refuting the possibility of a Stark splitting.

Next, resonant scattering was considered once the transmission and the PV spectra

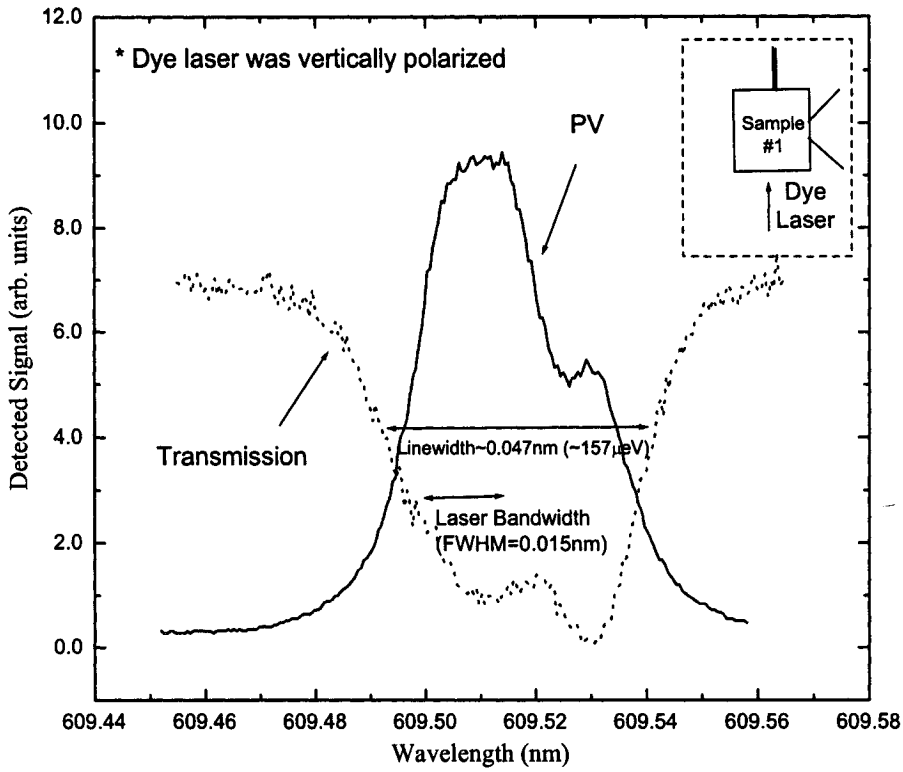

Figure 3.17: PV and Transmission spectra demonstrating a prominent splitting.

were plotted in Figure 3.17. Both spectra are consistent with each other; in both cases light is better transmitted at $\lambda = 609.51$nm compared to radiation at $\lambda = 609.53$nm, and vice versa. To test this possible scenario, a PV spectrum was taken with a dye laser directly incident on the electrodes, where no scattering effects should be detected. However, the splitting remained present.

At a later time, while discussing these results with an external researcher having expertise in the theoretical treatment of excitons, a polariton model was suggested to explain our results. A strong coupling of excitons with photons (polariton) under resonant conditions could yield two peaks corresponding to the photon-like and exciton-like polariton branches. However, a different polarization angle of the laser beam with respect to the crystal axis could yield weak coupling of the photons and excitons, where a single excitonic line would be observed as in Figure 3.12 (Sample#2). A change in laser intensity would lead to a change in the oscillator force, thereby obtaining a different splitting value. Spectra taken under various laser intensity did not reveal a change in position of the two peaks. Once again an attempt to pinpoint the source of the splitting falls short.

However, hope was renewed when D. Fröhlich recently presented results [47] demonstrating a similar splitting of the 1S line for specific polarizations with respect to certain crystal orientations. The nominal crystal orientation of our samples (100 symmetry) should correspond to polarization independent absorption [48]. However, low counts observed during XRD analysis revealed the poor orientation of surfaces of sample #1. Using a very well oriented Cu_2O sample (untouched since being cut by the crystallographer), XRD analysis of this sample yielded 400 000 counts. The same face yielded only 500 counts when it was slightly tilted on purpose with respect to the X-ray beam. Therefore, an imperfectly oriented sample face (unwanted component from another crystal orientation) due to numerous polishing procedures does have a large impact on the absorption process. This other component (possibly similar to the one used in [47]) could explain the splitting of the 1S line, however further investigation is still required to get a definitive answer.

In addition to the transmission spectrum presented in Figure 3.17 (dotted line), the equivalent spectrum in the presence of the packet ($\delta t = 220ns \Rightarrow$ half-transit time) are both displayed in Figure 3.18. The transmission spectrum taken in the presence of the exciton condensate (solid line in Figure 3.18), displays generally weaker signals compared to the spectrum measured in the absence of the condensate (dotted line). The splitting is still visible in the spectrum taken in the presence of the packet, suggesting that the

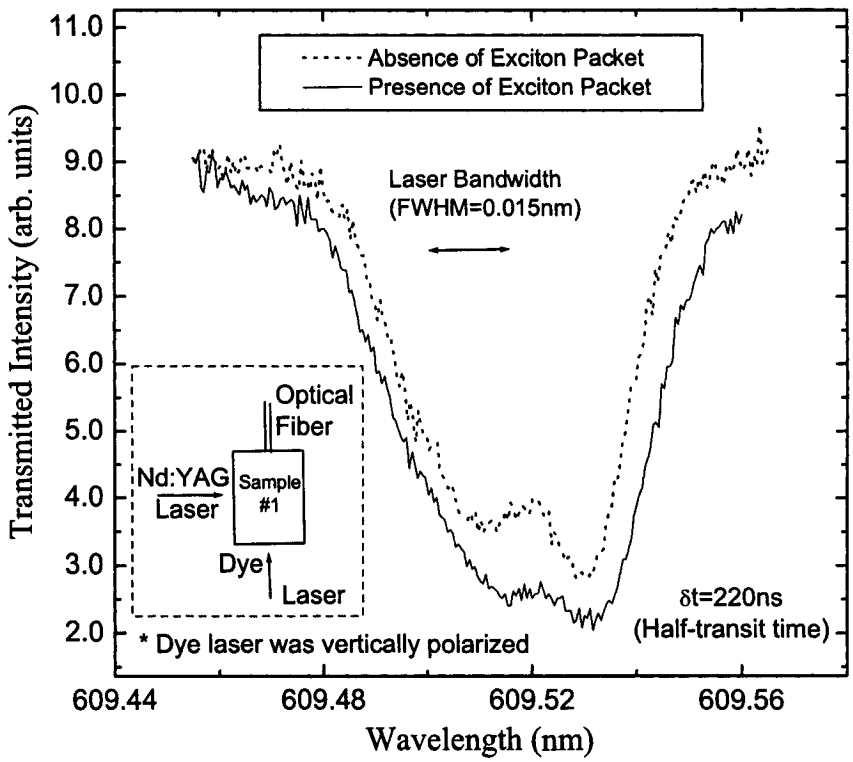

Figure 3.18: Transmission spectra taken in the absence and presence of the exciton condensate, where a prominent splitting is shown.

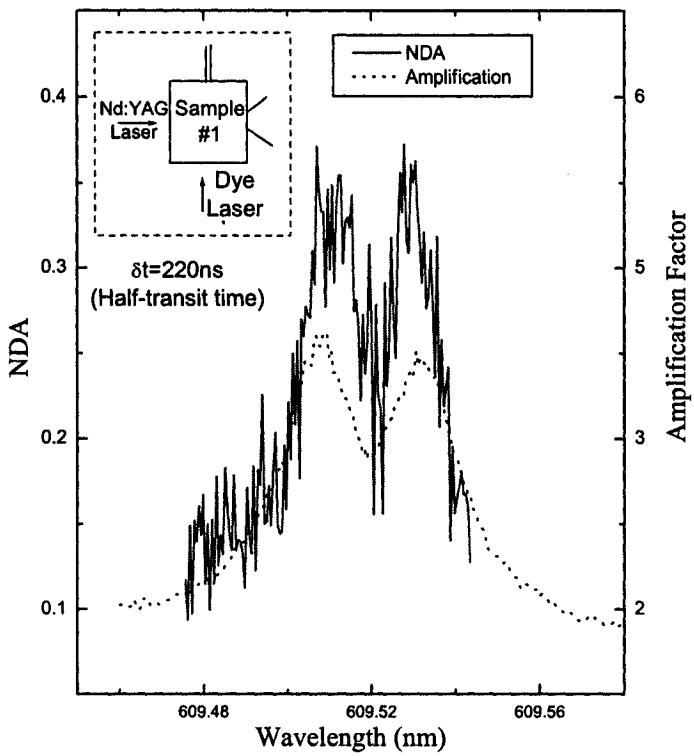

Figure 3.19: Wavelength dependance of both the condensate amplification and the NDA, where a prominent splitting is displayed.

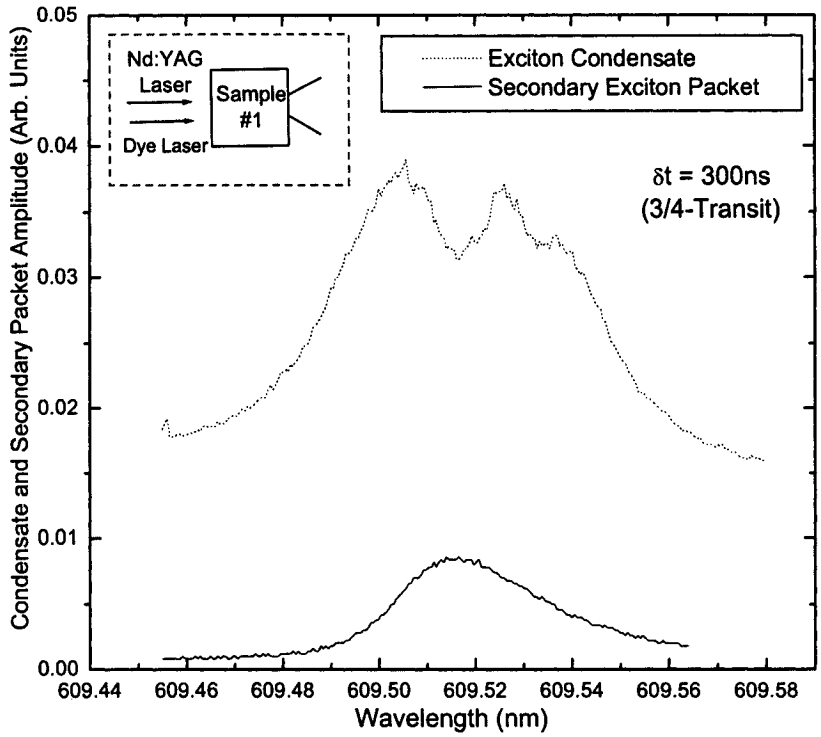

Figure 3.20: The wavelength dependence of both the condensate amplification and the secondary packet formation.

packet induced additional attenuation is dependent on the creation of excitons regardless of the splitting mechanism.

The packet-induced attenuation (NDA) formula discussed in section 3.1.2 for the case of resonant excitation, can also be applied to the whole spectral region of interest by using the two spectra presented in Figure 3.18. The result of the mathematical operation is shown (solid line) in Figure 3.19, where a significant splitting is depicted. The condensate amplification (dotted line) displayed in Figure 3.19 behaves similarly to the PV spectrum presented (solid line) in Figure 3.17, suggesting an amplification process dominated by the injection of resonantly created excitons into the packet.

Regardless of the exact mechanism producing the 1S line splitting observed in Figure 3.17, the spectral similarities (shape and splitting) of the NDA and condensate amplification spectra in Figure 3.19 clearly confirm an intimate relation between the two phenomena.

The wavelength dependence of both the exciton condensate amplification and the formation of the secondary exciton packet are shown in Figure 3.20. The discrepancy

between both curve profiles suggests that each phenomena must arise from a different mechanism. In fact, resonant stimulation of a somewhat dense (with sub-critical density) homogeneous distribution of cold excitons left behind by the packet results in the formation or onset of a secondary packet. However, in the case of condensate amplification, a resonant probe beam stimulates a well defined packet causing the condensate to be intensified.

The wavelength dependence on the secondary packet formation (no splitting) behaves differently from the observed PV spectrum, which suggests that cold excitons already present in the crystal are enticed to condense into a secondary packet by the resonant beam. The secondary packet is therefore not due to resonantly injected exciton as in the case of the condensate amplification process.

3.3 Longitudinal Measurements

Varying the path length difference of two laser pulses is equivalent to having a time delay between the two pulses. During experiments a dye laser pulse was launched into an optical fiber in order to extend its path length, hence generating a time delay between the dye laser pulse and the Nd:YAG laser pulse. The time delay is simply varied by using optical fibers of different lengths.

Specifically in the orthogonal excitation geometry, the time delay between the Nd:YAG and dye laser pulses is used to stimulate various parts of the travelling condensate. Knowing the transit time of the excitonic condensate, one can deliberately time delay the probing beam (dye laser) to intercept the center of the travelling condensate with a delay time equal to the half-transit time of the condensate. Longer time delays will result in probing the coma or tail portion of the condensate. Measurements at various time-delays determined the longitudinal profile of the exciton condensate.

3.3.1 Longitudinal Condensate Amplification & NDA

In the orthogonal excitation geometry, the condensate amplification as well as the NDA were measured for various longitudinal positions of the condensate (different time delays); the results are presented in Figure 3.21. The amplification factor is greater for time delays nearing complete synchronization of the dye laser with the travelling packet and drops to unity after the condensate has left the crystal (already detected). The NDA is also maximum at $\delta t \approx$ half-transit time, since the resonant pulse is incident on the

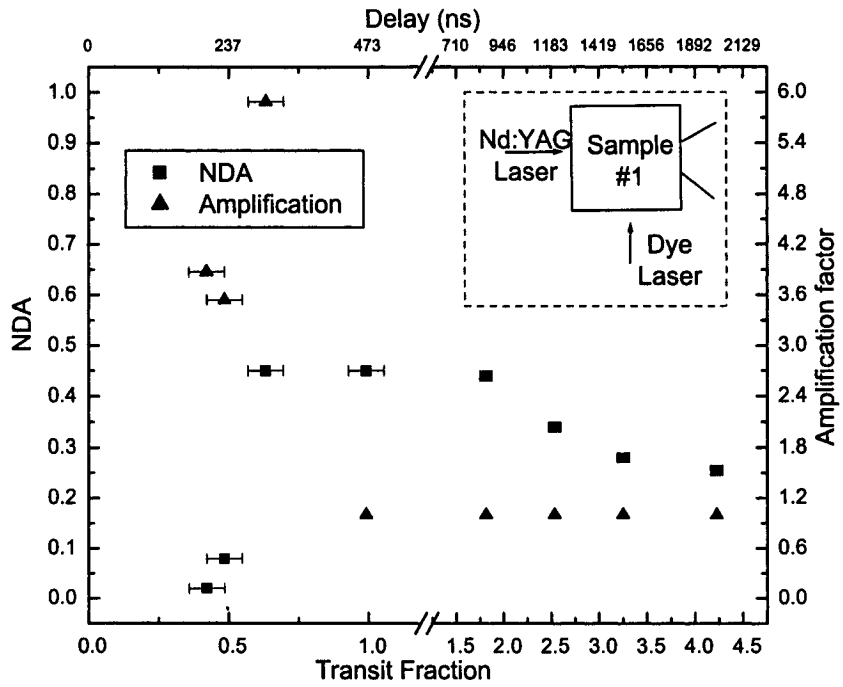

Figure 3.21: Probe beam time-delay (longitudinal) dependance of condensate amplification and NDA, in the orthogonal excitation geometry. The dye laser was tuned at the 1S orthoexciton resonance.

largest exciton density. At relatively larger delays (δt >1000ns), the NDA falls and tends towards a non-zero value due to secondary packet formation (section 3.1.3) of long lived paraexcitons still present in the crystal left behind by the condensate.

At time delays corresponding to pre-synchronization configuration ($\delta t <$ half-transit), the amplification factor drops while the NDA is zero until the synchronization condition between the packet and the probe beam is satisfied. The latter suggests that the travelling packet is able to collect excitons left over from the resonant pulse, while the resonant beam cannot be additionally attenuated (NDA) before the passage of the packet. Moreover, the reduced amplification factor observed at low time delays (low transit fractions) confirms the condensate's ability to collect left over excitons along its way towards the exciton detector, since the amplification factor is related to the time delay difference between the pump and probe beam. The sooner the packet intercepts the exciton gradient created by the resonant probe beam, the more excitons are available to be "collected", leading to a larger amplification factor.

As opposed to the NDA explanation given in [19], the NDA cannot be a result of a crystal distortion induced by the packet, since it is still observed at time delays larger than the transit time (in the absence of the packet). The NDA is therefore a direct measurement of the exciton density "$\rho_{exciton}$" in a specific region in the sample (NDA increases with $\rho_{exciton}$).

3.4 Lateral Measurements

As opposed to section 3.3 where the exciton condensate's longitudinal profile was measured, this section will deal with determining the lateral profile of the condensate. The lateral probing of the condensate is achieved from measurements taken at several vertical positions for a fixed time delay. This probing method can be viewed as a lateral profile for a longitudinal slice of the condensate. Equivalent measurements at different time delays will yield a lateral profile for a different longitudinal slice of the condensate. With the use of the average speed value of the unamplified exciton packet, time delays of the longitudinal probing can be converted to an equivalent spatial dimension. Numerous probed slices can be used to generate a 3D mapping of the exciton density present in the sample. This positional (longitudinal and lateral) probing method can be effectively used to construct a three-dimensional representation of the travelling exciton condensate in Cu_2O.

3.4.1 Lateral NDA

The lateral probing of the exciton condensate was achieved with the use of several optical fibers placed in a vertical configuration, as shown in Figure 2.10 of section 2.4.3. To insure proper light collection, the fibers were placed in contact with the sample. The dye laser pulse was incident on the various circular illumination conduits (at different vertical positions) on the sample holder (Figures 2.8 and 2.9), each having a corresponding optical fiber on the opposing side of the sample to collect the transmitted light.

The result of lateral probing for three different fiber positions is presented in Figure 3.22. The delay corresponding to synchronization ($\delta t = 300ns$), displays the most NDA and the sharpest contrast with respect to the lateral position. Such a result is expected when probing the core of the condensate, where the density of excitons is the greatest in addition to being spatially localized. The non-zero value of NDA at the edges correspond to the coma (non-condensed excitons surrounding the core) portion of

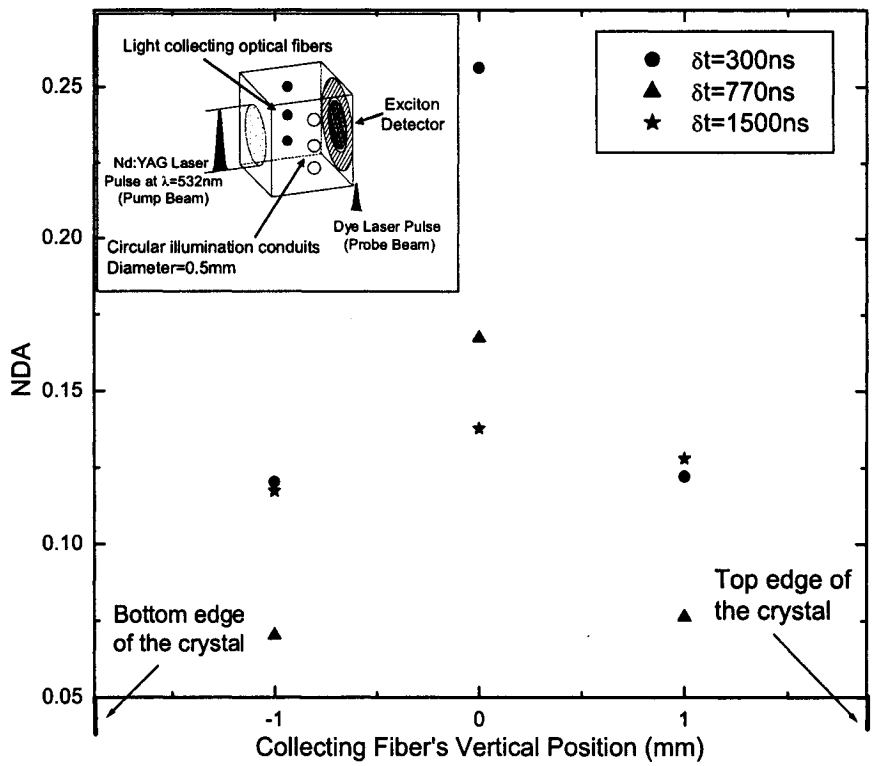

Figure 3.22: NDA measured at three different fiber positions, for various probe beam time delays.

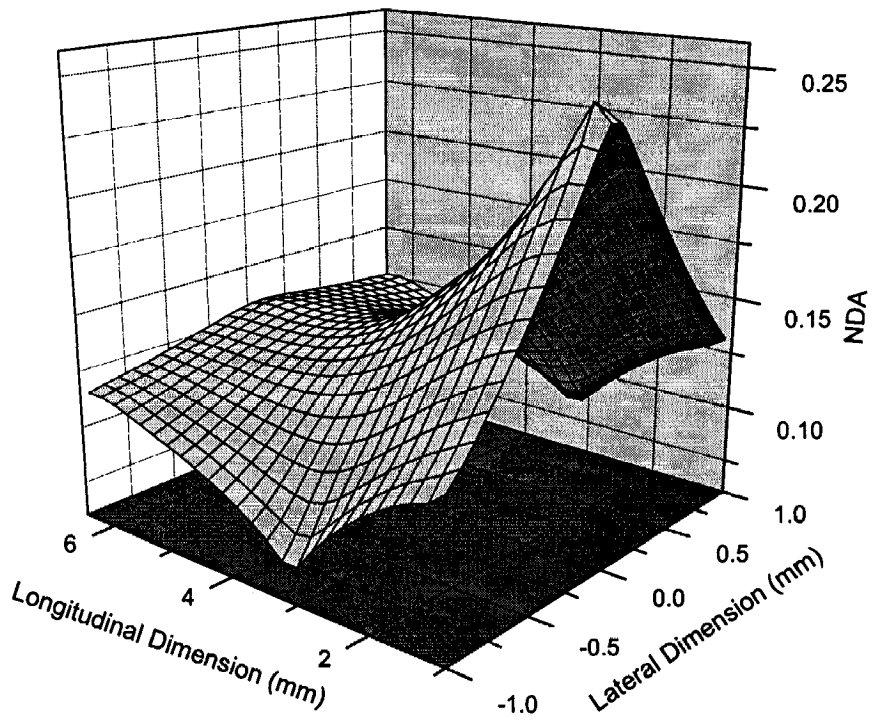

Figure 3.23: Side view: 3D representation of the travelling exciton packet with NDA.

the condensate. When the tail component ($\delta t = 770ns$) of the condensate is probed, a significantly weaker NDA and a lower lateral contrast is obtained. This indicates that the tail portion is wider than the core of the condensate and contains a lower exciton density compared to the core. To no surprise, the probing of cold excitons ($\delta t = 1500ns$) left behind by the condensate yielded the broadest NDA contrast (spatial distribution of excitons is almost the same everywhere), while the NDA is at its weakest (the density of excitons is low).

A peculiar aspect of Figure 3.22 is depicted for off-center positions where the NDA is greater at $\delta t = 1500ns$ than at $\delta t = 770ns$. This can be explained by the fact that at $\delta t = 770ns$ the tail of the condensate has not yet had a chance to broaden as in the case of $\delta t = 1500ns$.

The resulting 3D representation of Figure 3.22 is shown in Figures 3.23 and 3.24 from different perspectives. The longitudinal dimension was calculated according to the observed unamplified condensate velocity of 3900m/s. Note that the longitudinal dimension is larger than the crystal dimensions, and only represents the shape the packet would otherwise have in a larger sample. In Figure 3.25, the top view of the packet's 3D

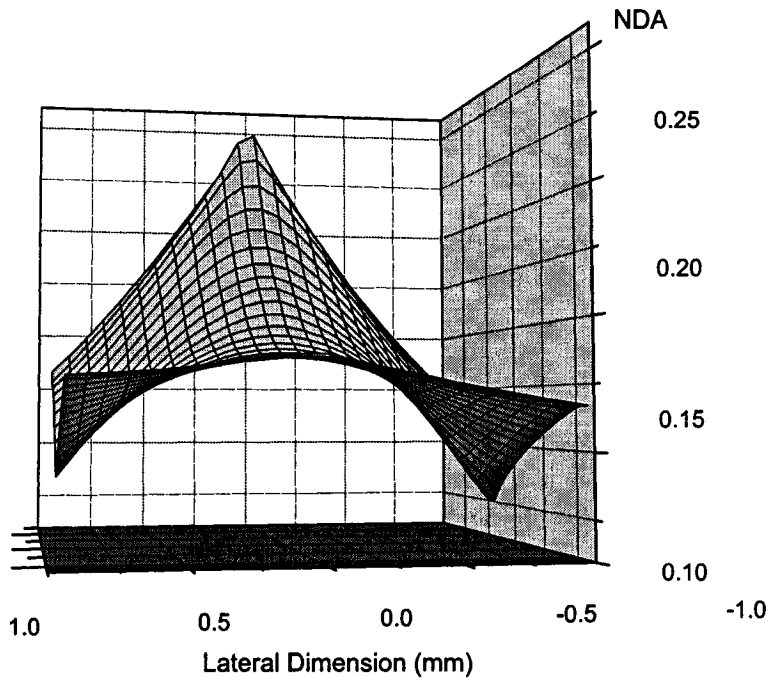

Figure 3.24: Rear view: 3D representation of the travelling exciton packet with NDA.

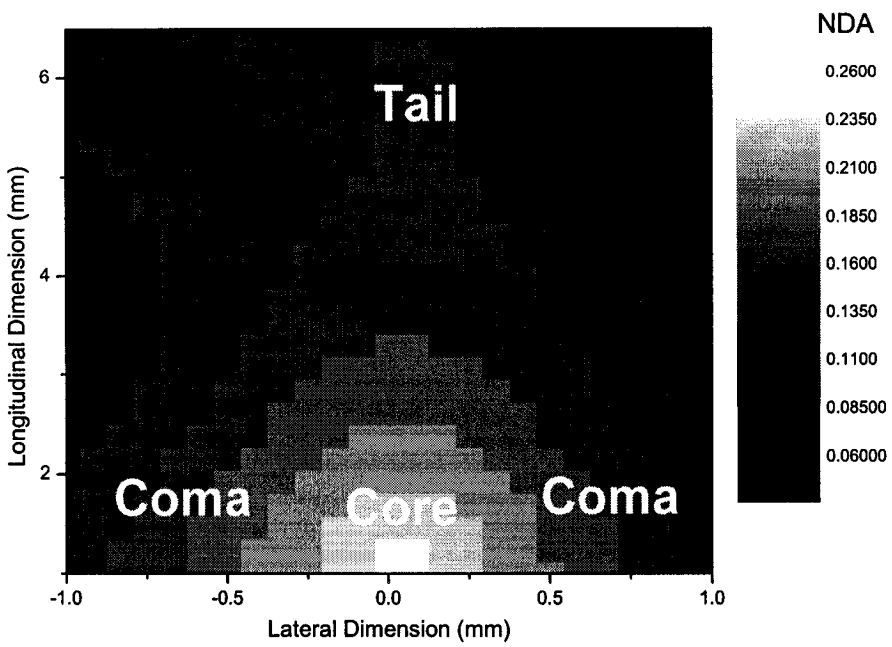

Figure 3.25: Top view (contrast) of the 3D representation of the travelling exciton packet constructed with spatial NDA measurements.

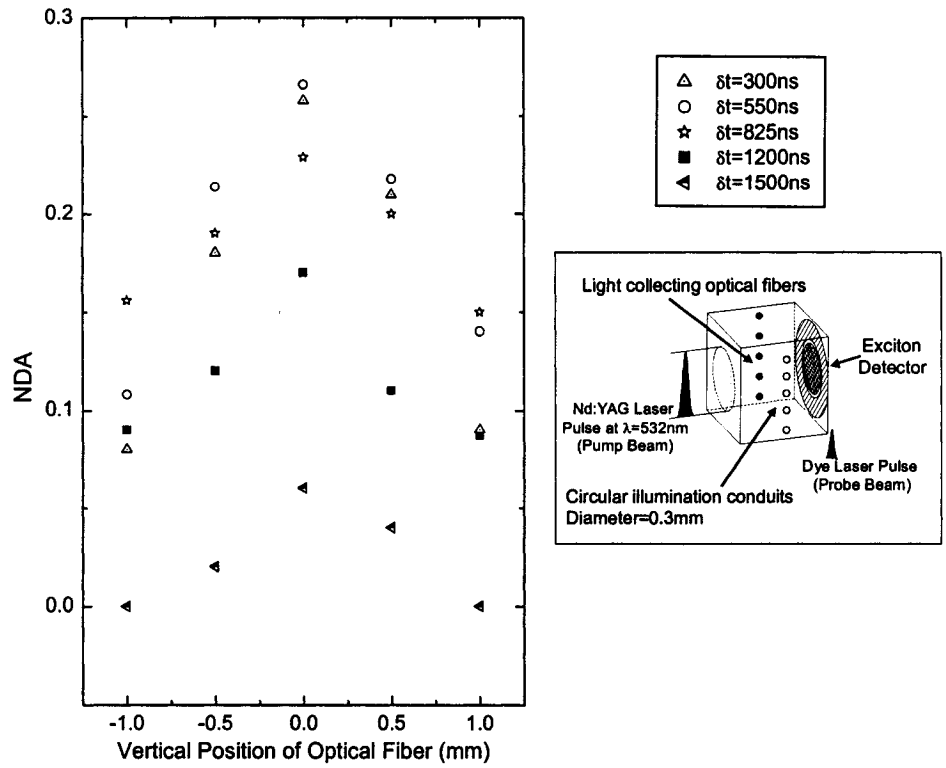

Figure 3.26: NDA measured at five different fiber positions, for various probe beam time delays.

mapping is shown with the NDA represented with color contrast. In the latter figure, the three condensate components are clearly depicted; 1) the core: yielding maximum NDA with a sharp lateral profile reflecting the large localized exciton density present; 2) the coma: relatively small exciton density surrounding the core is represented by relatively weaker NDA; 3) the diffusive tail is represented by the weakest NDA (corresponding to lower exciton density), and a fairly wide lateral profile. Please note that the contrast interval used in Figure 3.25 was chosen arbitrarily by the software package, and does not necessarily represent the measurement's spatial precision.

In order to get a better resolution in the lateral probing measurements, two more vertical positions were used, thereby adding two more data points to the lateral profile. In addition to the number of illumination conduits, their dimensions were also smaller (0.3mm) compared to 0.5mm used in Figure 3.22. The results of the lateral probing using five different probing positions are shown in Figure 3.26. The trend is essentially the same as the one seen with three probing positions (Figure 3.22). That is measurements taken at shorter time delays resulted in larger NDA values and sharper contrasts, whereas

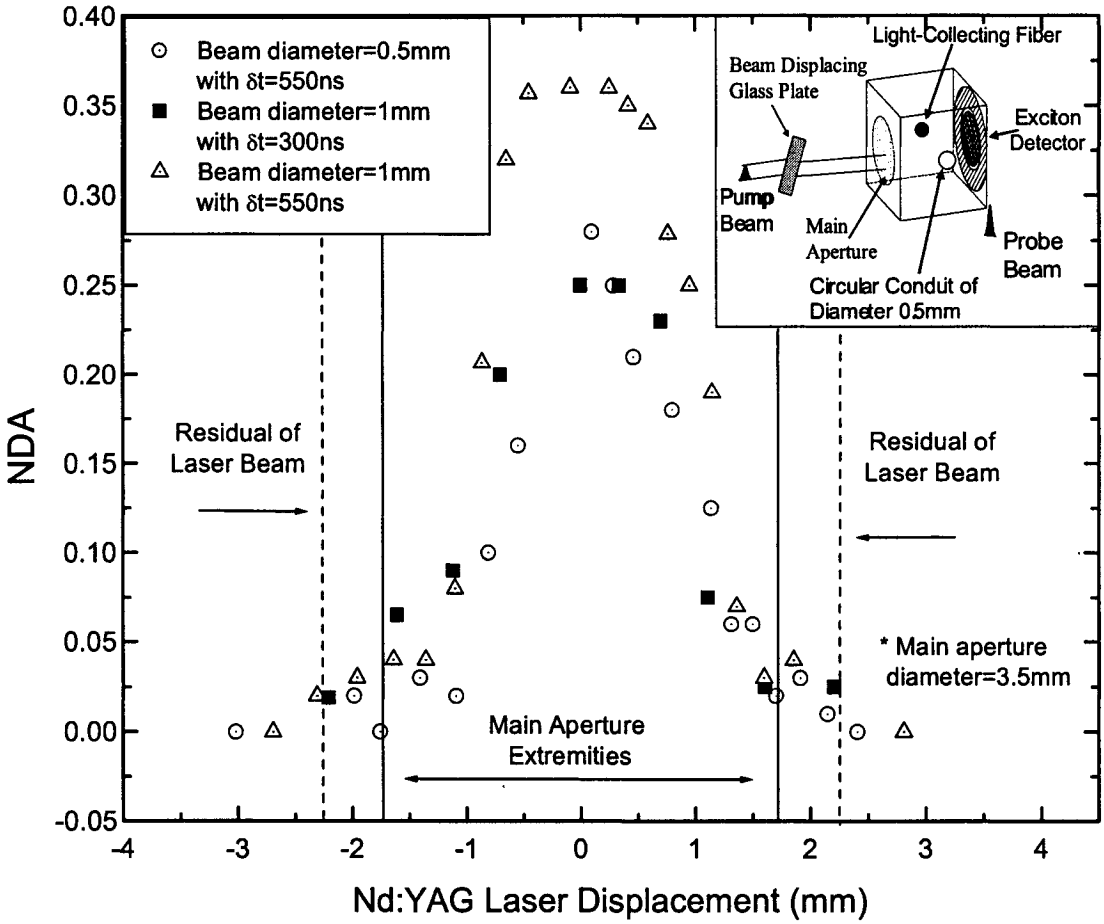

Figure 3.27: NDA measured by different vertical positions of the Nd:YAG laser.

longer delays have a weaker NDA with a broader contrast.

3.4.2 The Impact of the Pump Beam's Vertical Position on NDA

An alternative yet equivalent method of laterally probing the exciton condensate is achieved by vertically displacing the pump beam (Nd:YAG laser) while maintaining the probe beam (dye laser) at a fixed vertical position (usually at the center), as opposed to the method used in section 3.4.1 where a fixed pump beam position was used for various probe beam vertical positions. The pump beam was displaced by the glass plate as explained in Section 2.4.3.

Figure 3.27 clearly depicts the lateral profile of the exciton condensate at two different time delays for a beam diameter of 1mm. In agreement with the previous results

(section 3.4.1) the lateral profile is noticeably sharper for $\delta t = 300ns$ compared to a probe beam time delay of $\delta t = 550ns$. The resolvable packet width (lateral) $\approx$ 1mm), is comparable to the results shown in Figure 3.26. Resolution related to the various aperture size is evident in Figure 3.27 when comparing the FWHM of the profiles obtained with an aperture size of 1mm and 0.5mm for $\delta t = 550ns$ of the probe beam. The smaller aperture corresponds to a significantly sharper profile.

Conclusion

Experimental results concerning the optical probing of an excitonic Bose-Einstein Condensate in Cu_2O were presented. Three BEC-related phenomena were particularly studied in this thesis; the amplification of the exciton condensate resulting from a resonant probing beam stimulation; the additional attenuation (NDA) of the resonant beam induced by the passage of the packet; and the formation of a secondary packet attributable to resonant stimulation of cold exciton left behind by the travelling condensate. Each of these phenomena were carefully examined under various experimental conditions and lead to improvements in the condensate amplification model originally proposed by E. Benson.

During our experiments, the probe beam was targeted to stimulate different longitudinal sections of the travelling exciton packet when varying its time-delay with respect to the pump beam. Consequently, the condensate amplification and the additional probe beam attenuation (NDA) were measured at various parts of the condensate. In addition to measuring the longitudinal (horizontal) profile of the exciton condensate, sample illumination at several vertical positions for a specific longitudinal slice of the travelling packet (constant time-delay) revealed the packet's laterally dependent NDA profile. With the use of additional lateral profiles measured at different longitudinal slices of the packet, a three-dimensional representation of the exciton packet in Cu_2O was constructed. This 3D visualization successfully displayed the three condensate components (core, coma, and tail) originally envisioned by E. Benson [15].

In a different set of experiments, stimulating the tail portion of the travelling packet with a resonant probing beam induced the formation of a secondary packet. As a consequence, NDA observed at time-delays larger than the transit time of the condensate, was attributed to the formation of a secondary packet. Generating secondary packets under various experimental conditions proved to be prosperous in determining the mechanisms responsible for condensate amplification.

Also in this thesis, highly detailed spectra of the 1S line were taken with the use of

a tunable dye laser. The 1S line spectra from both the photovoltaic (PV) and transmission signals were used to establish a link between electrical and all-optical measurements. Transmission spectra taken at various sample temperatures enabled us to monitor the temperature evolution of the 1S line. Considering our laser bandwidth, the observation of thermal broadening at a low temperature difference from T= 2K, suggest a greater linewidth than the value reported for the 1S line in [20]. Furthermore, highly detailed spectra of the 1S line for a vertically polarized illumination on Sample#1 revealed an unusual splitting. Even though the origin of the splitting remains unclear, the splitting phenomena provided confirmation of the intimate relation between condensate amplification and NDA.

Further experiments could still be performed with the current experimental setup. Here are a few suggestions: a 3D representation of the packet obtained via spatial NDA measurements could be taken for different packet regimes (diffusive and nearly condensed states) by varying the pump beam intensity; in relation with the 3D mapping of the condensate, a better resolution of the longitudinal profile near the core can be improved with a larger number of time-delaying fibers with nominal length differences yielding smaller time-delay intervals. Apart from these suggested experiments, further study would require a different experimental setup such as having optical fiber arrays to precisely probe the lateral profile of the condensate as mentioned in section 2.4.3. Due to renewed interest in Cu_2O, many researchers around the world are presently conducting BEC-related research with this material. At the University of Pittsburgh, D. Snoke [49] is currently investigating exciton relaxation processes (ortho-para conversion) in view of BEC study. The experimental measurements are done on purposely stressed samples which establishes a harmonic potential for trapping excitons. A group at the University of Karlsruhe (Germany) also utilizing the "Pump and Probe" technique is currently studying the kinetics of excitons in various density regimes. They plan to incorporate our PV detection method, along with their optical detection technique in future experiments [50]. A research team from the University of Tokyo has recently (May 2003) reported the possible observation of BEC in Cu_2O [51]. In their experiments, paraexcitons are created directly via two-photon excitation, while a harmonic potential resulting from an applied stress on the sample is used to trap excitons in a specific region of the sample.

In conclusion we hope the work presented in this thesis will encourage others to pursue research in the field of excitonic BEC.

Bibliography

[1] A. Einstein, *Sitzungsber. Preuss. Akad. Wiss.* **Bericht 3**, 18 (1925).

[2] S. N. Bose, *Z. Phys.* **26**, 178 (1924).

[3] M. H. Anderson, J. R. Ensher, M. R. Matthews, C. E. Wieman, and E. A. Cornell, *Science*, **269**, 198 (1995).

[4] K.B. Davis, M.-O. Mewes, M.R. Andrews, N.J. van Druten, D.S. Durfee, D.M. Kurn, and W. Ketterle, *Phys. Rev. Lett.*, **75**, 3969-3973 (1995).

[5] The Toronto Star, August 14, 1994.

The Los Angeles Times, July 13, 1995.

The Washington Post, July 14, 1995.

The New York Times, January 27, 1997.

[6] A. Griffin, D.W. Snoke, and S. Stringari, *Bose-Einstein Condensation*, Cambridge University Press, Cambridge, 1995.

[7] S.A Moskalenko, and D.W. Snoke, *Bose-Einstein Condensation of Excitons and Biexcitons: and Coherent Nonlinear Optics with Excitons*, Cambridge University Press, Cambridge, 2000.

[8] L.V. Butov, C.W. Lai, A.L. Ivanov, A.C. Gossard, and D.S. Chemla, *Nature*, **417**, 47 (2002).

[9] P. Wachter, B. Bucher, and J. Malar, *Europhys. Lett.* , **62**(3), 343 (2003).

[10] D. Snoke, J.P. Wolfe, and A. Mysyrowicz, *Phys. Rev. B*, **41**, 11171 (1990).

[11] A. Mysyrowicz, D. Snoke, and J.P. Wolfe, *Phys. Stat. Sol. (b)*, **159**, 387 (1990).

[12] E. Fortin, S. Fafard, and A. Mysyrowicz, *Phys Rev. Lett.*, **70**, 3951 (1993).

[13] A. Mysyrowicz, E. Fortin, E. Benson, S. Fafard, and E. Hanamura, *Solid State Commun.*, **92**, 957 (1994).

[14] E. Benson, E. Fortin, and A. Mysyrowicz, *Phys. Stat. Sol. (b)*, **191**, 345 (1995).

[15] E. Benson, *Ph.D. thesis*, University of Ottawa, 140 (1999).

[16] M. Massé, *M.Sc. thesis*, University of Ottawa, 82 (2001).

[17] M.R. Andrews, C.G. Townsend, H.-J. Miesner, D.S. Durfee, D.M. Kurn, and W. Ketterle, *Science*, **275**, 637 (1997).

[18] G.A. Kopelevich, N.A. Gippius, and S.G. Tikhodeev, *Solid State Commun.*, **99-2**, 93 (1996).

[19] A. Merizzi, *M.Sc. thesis*, University of Ottawa, 89 (2001).

[20] D. Fröhlich, A. Kulik, B. Uebbing, and A. Mysyrowicz, *Phys. Rev. Lett*, **67**, 2343 (1991).

[21] E. Benson, E. Fortin, B. Prade, and A. Mysyrowicz, *Europhys. Lett.*, **40**(3), 311 (1997).

[22] A. Mysyrowicz, E. Benson, and E. Fortin, *Phys. Rev. Lett.*, **77**, 896 (1996).

[23] BEC website of W. Ketterle's group: *http ://c ua.mit.edu/ketterle_group/*

[24] N. Caswell, J.S. Weiner, and P.Y. Yu, *Solid State Commun.*, **40**, 843 (1981).

[25] M. Kavoulakis, G. Baym, and J.P. Wolfe, *Phys. Rev. B*, **53**, 7227 (1996).

[26] D.W. Snoke, A.J. Shiels, and M. Cardona, *Phys. Rev. B*, **45**, 11693 (1992).

[27] A.I. Bobrysheva, and S.A. Moskalenko, *Phys. Status Solidi (b)*, **119**, 141 (1983).

[28] D.W Snoke, J.P. Wolfe, and A. Mysyrowicz, *Phys. Rev. Lett.*, **64**, 2543 (1990).

[29] I. Loutsenko, and D. Roubtsov, *Phys. Rev. Lett.*, **78**, 3011 (1997).

[30] D. Roubtsov, and Y. Lépine, *Phys. Rev. B*, **61**, 5237 (2000).

[31] E. Hanamura, and H. Haug, *Phys. Rep. C*, **33**, 209 (1977).

[32] A. Imamoglu, R. J. Ram, S. Pau, and Y. Yamamoto, *Phys. Rev. A*, **53**, 4250 (1996).

[33] D. Hulin, A. Mysyrowicz, and C. Benoit a la Guillaume, *Phys. Rev. Lett.*, **45**, 1970 (1980).

[34] D. Snoke, J.P. Wolfe, and A. Mysyrowicz, *Phys. Rev. Lett.*, **59**, 827 (1987).

[35] E. Tselepis, E. Fortin, and A. Mysyrowicz, *Phys. Rev. Lett.*, **59**, 2107 (1987).

[36] E. Fortin, and W.M. Sears, *Can. J. Phys.*, **60**, 901 (1982).

[37] L.C. Olsen, and R.C. Bohara, *Appl. Phys. Lett.*, **34**, 47 (1979).

[38] J. Bardeen, *Phys. Rev.*, **71**, 717 (1947).

[39] C. Olsen, F.W. Addis, and W. Miller, *Solar Cells*, **7**, 247 (1982-1983).

[40] A.A. Berezin, and F.L. Weichman, *Phys. Stat. Sol. (a)*, **71**, 265 (1982).

[41] C. Klingshirn, T. Fleck, and M. Jörger, *Phys. Stat. Sol. (b)*, **234**, No.1, 23-24 (2002).

[42] A. Mysyrowicz, D. Hulin, and A. Antonetti, *Phys. Rev. Lett.*, **43**, 1123 (1979).

[43] A. Merizzi, M. Massé, and E. Fortin, *Solid State Communications*, **120-11**, 419 (2001).

[44] E. Fortin, and M. Massé, *Proceeding of International Conference on Excitonic Processes in Condensed Matter (Osaka, August 2000)*, World Scientific, 31-37 (2001).

[45] L. Hanke, D. Fröhlich, and H. Stolz, *Solid State Communications*, **112**, 455 (1999).

[46] S. Nikitine, J.L. Deiss, M. Certier, J.C. Merle, and A. Daunois, *J. Phys*, **27**, C2-107 (1966).

[47] D. Fröhlich, H. Stolz, G. Dasbach, R. Klieber, and D. Suter, Abstract, *NOEKS7 Conference, Karlsruhe*, (2003).

[48] M. Certier, *Ph.D. thesis*, L'Université de Strasbourg, 99 (1969).

[49] D. Snoke, *Science*, **298**, 1368 (2002).

[50] A. Jolk, M. Jörger, and C. Klingshirn, *Phys. Rev. B* , **65**, 245209 (2002).

[51] N. Naka, and N. Nagasawa, *Solid State Communications*, **126**, 523 (2003).